

DIGITALLY ENHANCED INTERFEROMETRY FOR PRECISION METROLOGY

CHATHURA PRIYANKARA BANDUTUNGA

A thesis submitted for the degree of
Doctor of Philosophy
of the Australian National University

June, 2020

© Copyright by Chathura Priyankara Bandutunga 2020
All Rights Reserved

Declaration

This thesis is an account of research undertaken between February 2015 and June 2020 at the Centre for Gravitational Physics, Department of Quantum Science, Research School of Physics, The Australian National University, Canberra, Australia.

Except where acknowledged in the customary manner, the material presented in this thesis is, to the best of my knowledge, original and has not been submitted in whole or part for a degree in any university.

Chathura Priyankara Bandutunga
June, 2020

Acknowledgements

Working towards this thesis has been a challenging, rewarding and enjoyable experience. It would not be possible without the great people I've had support me along the way.

Firstly, I'd like to acknowledge and thank my supervisor, Jong Chow. It has been an absolute pleasure to have worked with you and I thank you sincerely for the opportunities you have provided for me. I was introduced to you to take on a 'simple' project in acoustic sensing, and from that initial seed, we've managed to explore widely. Alongside your scientific mentorship, your insight and tutelage into other aspects of research and academic life has been an invaluable learning experience for me.

I extend my thanks to my second supervisor in every way but title, Malcolm Gray. Mal's broad and deep technical insight into everything from optics to digital signal processing has been a constant font of knowledge and both an excellent sounding board and an ever flowing stream for new ideas. The weeks that you were in the lab were by far the most productive, insightful and yet downright hilarious. Just magic.

To Jarrod, Roland and Terry. For anything practical, hands-on, or for a simple clarification and a word of encouragement (or shared cynicism), you were always available and approachable. As my mentors on the ground, in the lab, the 'DIY' mentality you all foster greatly encouraged me to just get the job done and find out of the box solutions to experimental problems (pun intended).

To the Graviteers, you make this place of work fun and enjoyable. In particular, David McClelland, thank you for your leadership of the group and the constant support and fostering of the Centre's wide range of research activities. I also extend my sincere thanks to John Close for being the spark that started this journey, and for providing guidance and direction both on a personal level and as Head of Department.

To my fellow PhD students. It's been quite a ride. To those who came before, Jarrod, Lyle, Sam, Shasi, Thanh, Georgia, Andrew, Tarquin and in particular Silvie. Thank you for making me feel welcome and a part of this large family. To my cohort, Cathy, Min Jet and David we made it! and we did it together. The many newcomers, you have all brought fresh energy to the group and made it a better place. It's really exciting to see so many bright, diverse people taking up the Graviteer mantle. Please forgive me for not naming you all! To Paul, James, Ya and Keshu your contributions and support both technically and as friends has been invaluable. To those I've had the pleasure of mentoring, Hugo, Lauren and Justin, I know you will all do great things.

To my friends outside the laboratory, thank you all for filling out and brightening up this adventure. Whether it's music with Twilight Jazz, boardgames with the Sri Lankan crew, D&D with high school friends or a catch up with the old physics crowd it was always fun and welcome. To be with so many close, supportive friends outside of university provided an invaluable perspective and change of scene, especially when work was hard.

To close; my family. You have carried me through everything and I would not be here without you all. Mum and Dad, words can not repay this debt and to my brother, together we are unstoppable. To my other half, Ya, my deepest thanks for standing by me through this journey.

Abstract

In this thesis we employ Digitally Enhanced Interferometric techniques to manage, measure or reject spurious interference. The technique, by using digitally controlled spread-spectrum modulation, manipulates the coherence of an optical source, enabling selective decoding of optical fields based on time-of-flight. Through this thesis, we demonstrate the use of this technique across three scenarios.

Firstly, in Part I, we consider the application to quasi-distributed interferometric sensing in the form of a multi-point interferometric acoustic sensing array. Using Digitally Enhanced Heterodyne interferometry, we demonstrate simultaneous readout from four discrete in-line surfaces using a single measurement optical field.

The demonstration characterises the displacement sensitivity of the measurement system, and proceeds to characterise the residual cross-coupling between the independent reflection surfaces. We further demonstrate some of the limitations of the digitally enhanced readout when considering equidistant targets, which has ramifications for multi-point sensing applications such as LIDAR.

The second body of work, presented in Part II, discusses the continued development of the Digitally Enhanced Fibre Frequency Reference. In this instance, we consider the coupling of coherent Rayleigh backscatter into the interferometric measurement. Using Digitally Enhanced Homodyne interferometry, we enable digital manipulation of the coherence length, thereby restricting the coupling of Rayleigh backscatter. The resultant phase noise is both modelled and measured, with good agreement between both.

We further implement a method, using a Rubidium stabilised optical frequency comb, to measure the long term drift of the fibre frequency reference. From this we are able to infer the thermal performance of the interferometer isolation chambers, the thermo-optic and thermo-elastic expansion of the interferometer. From these insights, we continue on to develop a nominal design for a future fibre frequency reference architecture.

The third and final project; Part III, considers the implementation of a Digitally Enhanced Homodyne interferometric readout to a Sagnac interferometer. The objective of this work was to demonstrate rejection of first order Rayleigh scattering, and was informed by the work on Rayleigh scattering in Part II.

As part of this project, we also demonstrate the first demonstration of a digital interferometric readout using an incoherent source, one which is significantly broader than the digital interferometric spread-spectrum modulation. We also present a first demonstration of sub $1 \text{ prad}/\sqrt{\text{Hz}}$ noise floor using a digital interferometric readout. Finally, we also surpass the theoretical Rayleigh backscatter induced phase noise floor, demonstrating rejection of first order Rayleigh scattering.

Contents

Declaration	iii
Acknowledgements	v
Abstract	vii
1 Thesis Prologue	3
1.1 Digitally Enhanced Interferometry: An Introduction	4
1.2 Thesis Overview	5
1.3 Publications	6
1.4 Patents	6
I Digitally Enhanced Interferometric Acoustic Sensing Array	7
2 Multiplexed Interferometric Acoustic Sensing	9
2.1 Multiplexed Interferometric Sensing	10
2.2 Multiplexing Techniques	12
2.3 Digitally Enhanced Acoustic Sensing	15
3 Digitally Enhanced Heterodyne Interferometry	17
3.1 Heterodyne Interferometry	17
3.2 IQ Demodulation and Phase Extraction	19
3.3 Pseudo-Random Modulation Sequences	21
3.3.1 Definitions	22
3.4 Digitally Enhanced Heterodyne Interferometry	24
4 Multipoint Acoustic Sensing Array	31
4.1 Conceptual Design	31
4.2 Experimental Implementation	32
4.3 PRN Code Aliasing Effects	35
4.4 The Three Signal Measurement	36
4.5 Transducer Response Measurements	37
4.6 Displacement Sensitivity	38
5 Crosstalk Characterisation & Limits	39
5.1 Three Channel Crosstalk	40
5.2 Source of Cross-Coupling	40
5.2.1 PRN Correlation Limits	40
5.2.2 Mechanical Coupling	42
5.2.3 Spatial Resolution Limits	44
5.2.4 Multi-Pass Reflections	47

6 Multipoint Acoustic Sensing Conclusions	49
6.1 Key Specifications	50
6.2 Future Work	50
II Digitally Enhanced Fibre Frequency Reference	53
7 Stabilising Optical Sources	55
7.1 Quantifying Optical Stability	56
7.1.1 Allan Variance	56
7.1.2 Spectral Densities	57
7.2 Measuring Frequency: References and Standards	58
8 Digitally Enhanced Homodyne Interferometry	63
8.1 Homodyne Interferometry	63
8.2 Quadrature Phase Shift Modulation	65
8.3 Double Demodulation	68
8.4 FPGA Implementation	70
9 Fibre Interferometer Frequency Reference	73
9.1 Conceptual Design	73
9.2 Experimental Implementation	75
9.3 QPSK Modulation Generation	78
9.4 Differential Stability Measurement	81
10 Gating of Rayleigh Backscatter Induced Phase Noise	85
10.1 Scattering in Optical Fibres	85
10.2 Backscatter Induced Phase Noise	86
10.3 Experimental Demonstration	91
11 Infrasonic Performance of a Fibre Frequency Reference	95
11.1 Optical Frequency Comb Wavelength Metrology	95
11.2 Digital Phasemeter Implementation	98
11.3 Comb Referenced Laser Frequency Readout	101
11.4 Hybrid Fibre-Comb Frequency Reference	103
11.5 Determining the Thermal Corner Frequency	106
11.6 Thermal Expansion of the Fibre Frequency Reference	108
12 Future Frequency References	111
12.1 Rayleigh Scattering Suppression Conclusions	111
12.2 Hybrid Fibre-Comb Conclusions	112
12.3 Towards A Future Reference Architecture	113
III Digitally Enhanced Fibre Optic Gyroscope	115
13 Gyroscopes for Inertial Navigation	117
13.1 Gyroscope Architectures & Characterisation	118
13.2 From Rotation to Optical Phase	120
13.3 Fibre Optic Gyroscopes	122

13.4	Technical Limits of Fibre Optic Gyroscopes	124
13.4.1	Rayleigh Backscattering	124
13.4.2	Shupe Effect	125
13.4.3	Optical Kerr Effect	125
13.4.4	Magnetic Field and Polarisation Effects	126
13.5	A Digitally Enhanced Fibre Optic Gyroscope	126
14	Digitally Enhanced Sagnac Interferometer	127
14.1	Rayleigh Scattering Limits	127
14.2	Conceptual Design	129
14.3	Experimental Implementation	133
14.4	Phase Calibration & Signal Extraction	135
15	Noise Characterisation Measurements	137
15.1	Relative Intensity Noise	137
15.2	Voltage Noise Coupling	140
15.2.1	Calculating Photodetector Dark Noise	141
15.2.2	Insight Balanced Photodetector	142
15.2.3	ADC Analog Front-end Noise	143
15.3	Direct Digital Synthesis Spurs	145
15.4	System Noise Budget	147
15.5	Beyond Rayleigh Scattering	149
16	Towards a Gyroscopic Measurement	153
16.1	Conclusions from Initial Prototype	153
16.2	Future Gyroscope Development	154
16.2.1	Scale Factor Calibration	154
16.2.2	Mitigation of Second Order Rayleigh Backscattering	155
16.2.3	Digitally Enhanced Polarisation Management	156
17	Thesis Epilogue	159
	Bibliography	161

List of Figures

1.1	Thesis Outline	5
2.1	Applications of acoustic sensors	9
2.2	Multiplexed Sensing Topologies	10
2.3	Temporal multiplexing concept	13
2.4	Spectral multiplexing concept	14
3.1	Two Beam Heterodyne Interferometry	18
3.2	IQ demodulation functional diagram	21
3.3	Simulated 3-bit PRN sequence auto-correlation	23
3.4	Functional diagram of a 3 bit linear feedback shift register	24
3.5	Simulated 3-bit PRN Sequence	25
3.6	Two beam Digitally Enhanced Mach Zehnder interferometer	26
3.7	Digitally enhanced heterodyne interferometry encoding	27
3.8	Digitally enhanced heterodyne interferometry decoding	28
4.1	The multiplexed acoustic sensing concept.	31
4.2	Multiplex acoustic sensing experimental diagram	33
4.3	Piezo mounted reflectors photograph	34
4.4	Optical table photograph	34
4.5	PRN aliasing harmonics	35
4.6	Initial recording demonstration	36
4.7	Piezo mirror transfer function measurement	37
4.8	Displacement sensitivity measurement	38
5.1	Cross-talk measurement interpretation	39
5.2	Three channel cross-talk measurement amplitude spectral density	41
5.3	Weighting of received PRN symbols	42
5.4	Mechanical coupling test schematic	43
5.5	Mechanical coupling measurement amplitude spectral density	43
5.6	PRN Spatial Resolution and Partial Correlations	44
5.7	Methods for increasing digital interferometric spatial resolution	46
5.8	Coupling of Multi-bounce elatons	48
5.9	Multi-pass cross-talk measurement amplitude spectral density	48
7.1	Frequency regimes of frequency references	58
8.1	Basic Homodyne Mach Zehnder Interferometer	64
8.2	Quadrature Phase Shift Key Constellation	65
8.3	QPSK generation example	66
8.4	Homodyne Digital Interferometry Mach Zehnder interferometer	67
8.5	Double demodulation phasor projections	68

8.6 QPSK Binning Algorithm	71
8.7 QPSK FPGA Demodulation Architecture	72
9.1 In-line frequency reference concept	75
9.2 In-line fibre frequency reference schematic	76
9.3 Isolation Chamber Design and Layout	77
9.4 200 MHz AOM carrier generation	79
9.5 High-speed AOM transfer function	80
9.6 Measured QPSK spectrum	80
9.7 In-line reference time domain measurement	81
9.8 In-line reference amplitude spectral density	82
9.9 In-line reference Allan deviation	83
10.1 Phasor description of Rayleigh scattering	87
10.2 Digital interferometric gating of Rayleigh backscatter	90
10.3 Measuring Rayleigh scattering phase noise	92
10.4 Estimated and measured Rayleigh scattering phase noise	93
11.1 Stabilising an optical frequency comb	96
11.2 Phase locked loop schematic	99
11.3 PLL transfer function test schematic	100
11.4 PLL measured transfer function	100
11.5 Frequency comb beat note detection setup	101
11.6 Laser frequency drift measurement	102
11.7 Hybrid fibre-comb reference experimental setup	104
11.8 Hybrid frequency reference time domain residual	105
11.9 Hybrid frequency reference time domain residual (Zoomed in)	105
11.10 Hybrid frequency reference frequency spectral density comparison	106
11.11 Fibre frequency reference infrasonic stability estimate	107
11.12 Fibre frequency reference thermal expansion	108
12.1 Future fibre frequency reference architecture	114
13.1 Inertial measurement	117
13.2 Sagnac effect	120
13.3 The canonical fibre optic gyroscope	123
14.1 Digitally enhanced fibre optic Sagnac interferometer concept	130
14.2 Coupling of Rayleigh scattering in a Sagnac interferometer	131
14.3 Preliminary digital enhanced Sagnac interferometer setup	134
14.4 White light digital interferometry signal extraction	136
15.1 Balanced Detection Experimental Setup	138
15.2 Balanced detection phase noise measurement	139
15.3 Balanced photodetector comparison	143
15.4 FPGA simulation schematic	144
15.5 ADC analog front end noise tests	145
15.6 Functional diagram of direct digital synthesis	146
15.7 Reduction of DDS generation harmonics	147
15.8 Interferometer phase sensitivity	148

15.9 Balanced AOM Schematic	149
15.10 Rayleigh scattering rejection	150
15.11 Projected gyroscope sensitivity	152
16.1 Real-time gyroscope scale factor calibration	155
16.2 Polarisation managed gyroscope architecture	157

List of Tables

5.1	Cross-talk values for combinations of injection and readout channels	40
5.2	Multi-pass cross-talk values for combinations of injection and readout channels	47
7.1	Frequency dependence of noise processes	56
10.1	RBS noise floor measurements	91
12.1	Future reference parameter estimates	113
13.1	Gyroscope sensitivity grades	119
15.1	Coil parameters for rotation sensitivity estimate	151

Thesis Prologue

All optical metrology can be reduced to the precise measurement of an environmental parameter on either the amplitude or phase of an interrogating optical field. Interferometric measurements encompass a specific range of techniques which are able to measure the optical phase to sub-wavelength precision. This can be used quantify a wide variety of measurands which affect the optical phase including displacement, rotation and changes in refractive index of the optical medium. Applications stemming from interferometry are therefore diverse and span a large breadth of optical metrology, including geophysical survey, astronomy, spectroscopy, optical coherence tomography and gravitational wave detection.

In parallel, the past decades have seen substantial development of the communications sector. The explosion in the capabilities of real-time computing and signal processing has been driven by the increasing availability of high performance, field deployable computing hardware. As society ever edges towards a completely connected and integrated network, the accompanying techniques for handling the decoding and decoupling of signals from multiple unique sources has been continually developed and refined.

Combining these two areas, Digital Interferometry uses pseudo random bit sequences to encode, and overlay, an additional layer of optical coherence. In many ways, we can draw parallels from spread-spectrum interferometric techniques, such as optical coherence tomography, however in our case the spread-spectrum being a digitally controlled parameter. When coupled with real-time parallelised decoding architectures this enables selective signal range-gating and multiplexing based on the optical time-of-flight, without compromising the sensitivity of the interferometric readout.

The underlying tenet of Digital Interferometry has always been to ‘pivot from optical complexity to digital signal processing’. In this thesis, we explore how the operational flexibility enabled by digital interferometry can be leveraged to develop methods for multiplexing, laser stabilisation and the rejection of spurious signals in the next generation of high precision interferometric sensors.

1.1 Digitally Enhanced Interferometry: An Introduction

Digitally enhanced interferometry (DI) was developed to transfer the added optical complexity typically found in multiplexed systems into the digital signal processing realm[1]. As a result, DI systems are both optically simple and robust, important traits for use in real world applications. The initial concept was developed on a heterodyne architecture allowing DI to retain the ability to perform high sensitivity phase and displacement measurements[1, 2, 3].

Since its initial development, early demonstrations of Digital interferometry by de Vine and Wuchenich have shown picometer displacement sensitivities and the ability to isolate up to three unique displacement signals at sub-audio frequencies respectively [3, 4]. Concept work on the ranging system for the laser interferometer space antenna (LISA) was also carried out by Sutton[5]. This work has been carried forward by Francis et al in more recent work demonstrating a proof-of-concept architecture for the GRACE II climate mission[6].

Alongside the space based gravitational wave and gradient detectors, digital interferometry has been moving from the concept phase towards more specific applications. Several of these applications stem from the challenge of tracking and manoeuvring of space debris. Towards this purpose, digitally enhanced heterodyne systems have been developed capable of tracking the fast moving, high Doppler regime targets presented by space debris[7]. In parallel, the development of an internally sensed optical phased array has combined both the high precision phase measurement and control with the multiplexing afforded by digital interferometry demonstrating high power handling capability for debris manoeuvring[8].

As a fork of the main heterodyne technique, Ralph et al has demonstrated spatial multiplexing using digital interferometry allowing for simultaneous readout of multiple digital ‘pixels’ of an optical wavefront from a single element photodetector[9]. However the largest single development to Digital Interferometry since its conception came with the development of the homodyne variants [5, 10]. These were initially developed by Sutton et al, and the concept has been applied in earlier generations of the fibre frequency reference by Ngo et al[11, 12].

The work we present here draws on all of the prior work on digital interferometry, both heterodyne and homodyne. It is hoped that through this body of work, new insights into the techniques, its potential strengths and limitations, and how it may be applied into a commercially viable sensor may be brought to light.

1.2 Thesis Overview

In this thesis, we consider three unique systems which use digital interferometry to augment or enable an interferometric readout. As such, the thesis is divided into three distinct parts which, given a working knowledge of digital interferometry, may be read in isolation with minimal cross-referencing. An outline of the three parts is shown in Figure 1.1.

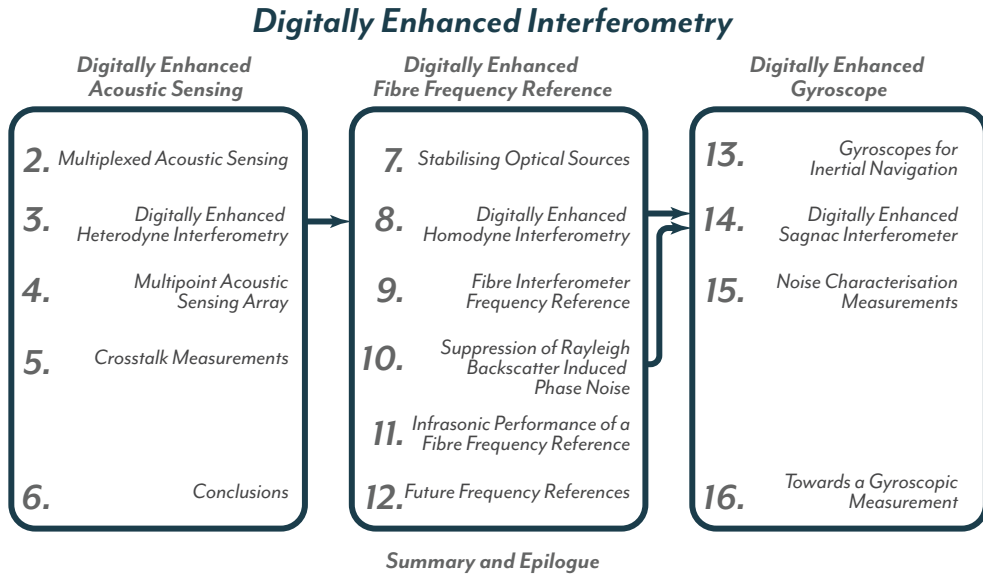


Figure 1.1: This thesis is structured in three parts. In each part we consider the use of digital interferometry in a specific application. While specific prior knowledge is not assumed, the arrows indicate where background reading will be insightful in interpreting the content of later chapters.

In Part I, we use digitally enhanced heterodyne interferometry to implement a multiplexed in-line interferometric readout, characterising displacement sensitivity and cross-talk coupling between successive measurement points. Part II switches to the use of digitally enhanced homodyne interferometry, as used by the fibre frequency reference. We extend on prior work by McRae and Ngo; characterising the coupling of Rayleigh scattering and fibre thermal expansion using a new in-line Michelson design. In Part III, we draw on the insight into Rayleigh scattering dynamics from the fibre frequency reference work and use it to address residual Rayleigh backscatter induced phase noise in Sagnac interferometers.

Finally, while digitally enhanced heterodyne interferometry is a well established and published technique with near a decade of development, its homodyne variant is a significantly less explored and developed technique. As such, it is hoped that Chapter 8 which outlines the implementation of a digitally enhanced homodyne interferometric readout, in conjunction with the work by Sutton [5], can serve as reference for future implementations of the technique.

1.3 Publications

As part of this candidature, several articles have been prepared for publication. The ones pertinent to this thesis are listed below.

- [13] Y. Zhang, C. P. Bandutunga, M. B. Gray, and J. H. Chow, “*Multi-target CW interferometric acoustic measurements on a single optical beam,*” Opt. Express **27**, 18477-18483 (2019)
- [14] C. P. Bandutunga, T. G. McRae, Y. Zhang, M. B. Gray, and J. H. Chow, “*Infrasonic performance of a passively stabilized, all-fiber, optical frequency reference,*” Opt. Express **28**, 9280-9287 (2020)

1.4 Patents

Systems and Methods for Sagnac Interferometry, Australian Provisional Patent Application No. 2020903073. Date Filed: 28 Aug 2020.

Part I

**Digitally Enhanced
Interferometric Acoustic Sensing
Array**

Multiplexed Interferometric Acoustic Sensing

Acoustic sensing is an umbrella term which covers a wide array of sensor architectures and frequency bands of interest. The applications of these sensors, as illustrated in Figure 2.1, extend from vibration monitoring on industrial sites, audio recording for communication and artistic purposes through to medical and biological applications of ultrasound detectors[15]. At their core, all acoustic sensors are functionally identical, converting a pressure wave into a displacement through an intermediary medium acting as a transducer, and measuring the induced displacement through a sensing system. To date, the majority of acoustic sensing use electro-magnetic systems, which include the use of piezo-electric, inductive or capacitive sensors.

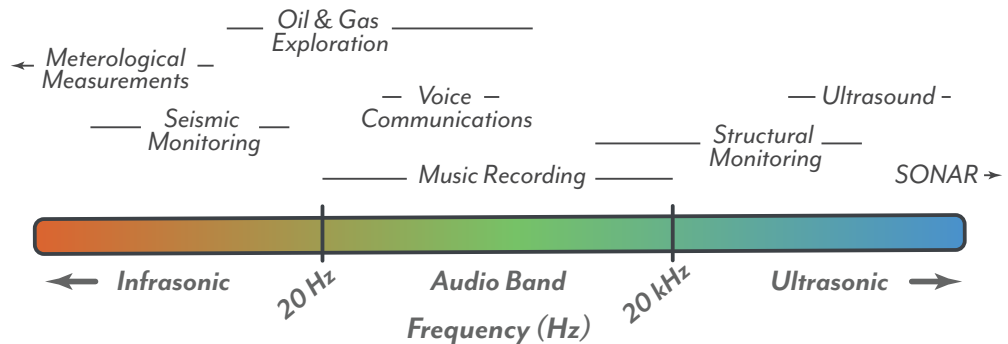


Figure 2.1: Acoustic sensors can be categorised based on the frequency band they operate. Based on three frequency bands, infrasonic (< 20 Hz), audio (20 Hz - 20 kHz) and ultrasonic (> 20 kHz) we show the approximate frequency regions of interest for different commercial, industrial and medical applications.

With the continual improvement of photonic sensors and growth of the optical telecommunications industry, the development of optical readouts for acoustic sensors has emerged as an alternative to electro-magnetic sensors. When coupled with the optical transport capabilities of optical fibre, the main advantages of these optical systems can be found in specific, niche applications where the sensitivity, remote operation or immunity to electro-magnetic interference outweighs the considerable cost differential between their electromagnetic counterparts[16].

In this chapter we discuss some of the techniques available to perform interferometric sensing, with a specific focus on acoustic sensing. We then proceed to consider how these techniques might be multiplexed, drawing on the expertise founded in optical and wireless communications standards.

2.1 Multiplexed Interferometric Sensing

Interferometric optical sensors use the interference of light to measure precise changes in the optical path length of an interrogating optical field. With the appropriate interrogation technique, it is possible with these sensors to recover sub-wavelength precision, enabling sub-nanometre scale sensitivities to be achieved. We can class interferometric sensors into three main areas, dependent on the type of sensing architecture employed and the source of the interfering fields. The three classes we consider are single point, distributed and quasi-distributed sensors, and their different topologies are shown in Figure 2.2.

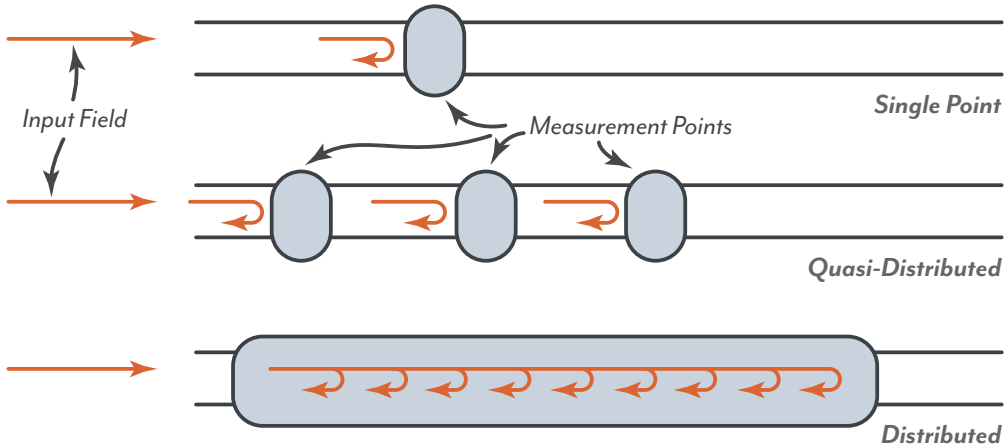


Figure 2.2: Displacement sensing can be done in several different ways. Single point sensors measure displacement at a single point, as their namesake suggests, and thus require independent systems for each measurement point. Quasi-distributed and distributed sensors allow for some or all of the physical system to be used to make multiple unique measurements. Quasi-distributed sensors use multiple single point sensors in conjunction with a multiplexed interrogation method to differentiate each sensor. Unlike the spatially separate point measurements of quasi-distributed systems, fully distributed sensors are able to measure displacement continuously along the sensing path using distributed reflection sources such as scattering.

Single Point Sensors

Single-point interferometers use well defined reflections from distinct surfaces to act as displacement markers. As such, they measure the displacement of only these displacement markers. Common methods for single point sensors include continuous wave laser ranging systems such as frequency modulated continuous wave LIDAR systems[17], fibre Bragg grating based sensors[16], or at the extreme, gravitational wave detectors[18]. In each case, it is only the displacement signal of the illuminated surface, Bragg grating or gravitational wave test masses, that is measured.

One significant class of point sensors are based on the Fibre Bragg Grating (FBG). FBG sensors rely on the grating strain response to induce a measurable shift in the Bragg wavelength, the reflectivity peak of the grating[19]. Depending on the readout, the change in the reflected wavelength can be measured as a frequency shift using a heterodyne readout, or by measuring the corresponding reflected intensity change of a single frequency source[16, 20]. Both of these techniques do not rely on an interferometric readout, and are limited in resolution by the bandwidth of the grating reflectivity profile. To surpass this limit, Fibre Bragg gratings can be combined in matched pairs to create intrinsic fibre Fabry-Perot cavities. Any dynamic change to the length of the cavity can be read out using an interferometric interrogation method, allowing for picometer precision to be achieved[21, 22, 23].

As FBGs can be fabricated directly in an optical fibre, architectures based on them are classified as intrinsic sensors. However, depending on the application it can be advantageous to interrogate using an external or extrinsic transducer. A widely developed sensor of this type is the extrinsic fabry perot[24, 25]. In these sensors, an optical cavity is formed between a delivery optical fibre or backplate, and a highly reflective acoustic diaphragm. The length of the optical cavity can be measured using standard cavity phase interrogation techniques, such as the Pound-Drever-Hall or Hänsch-Couillaud phase readouts.

Distributed Sensors

Distributed systems, as their namesake, rely on distributed signal sources such as Rayleigh or Brillouin scattering to measure signals along a sensing element. The measurement of the scattering profile, or time correlated speckle pattern then reveals information on external influences on the scattering medium at a specific distance. These sensors are typically designed using fibre optic systems, relying on the stress and temperature sensitivity of optical fibre while simultaneously allowing for optical delivery. Distributed sensing architectures have also been adapted to measure scattering from particulates in the atmosphere for aerosol and wind speed detection[26, 27, 28]. More recently, phase sensitive variants of these techniques have been developed to further improve the resolution and sensitivity of distributed readouts. This includes the use of coherent amplification and narrow linewidth sources and optical frequency combs[29, 30].

A drawback of fully distributed sensing architectures is the displacement sensitivity achievable with stochastic scattering sources. As such, for high precision applications, single point interferometry remains the gold standard. In the following section, we discuss how multiplexing techniques can be used to expand the functionality of single point sensors into an array, bridging the gap between single point and distributed sensors.

Quasi-Distributed Sensors

Quasi-distributed sensors fall into a category between single point and fully distributed readouts. As shown in Figure 2.2, single point sensors may be multiplexed to create a sensing array. While able to measure over a broad spatial area, each individual measurement in quasi-distributed systems is confined to the local area around each point sensor. Examples of this include hydrophone or geo-phone arrays for submarine detection and oil and gass exploration respectively[31, 32, 33]. The sensitivity of these systems are typically high due to the use of single point sensors, however the spatial resolution and scalability

is limited by the multiplexing technique used to interrogate the array. As such, the multiplexing technique used represents a critical component of these systems and the main methods used to achieve quasi distributed sensors of this form are discussed in the following section. Through the course of the work presented here, we use this definition of Quasi-distributed sensors.

2.2 Multiplexing Techniques

Multiplexing is a necessary requirement of modern communication systems. Multiplexing architectures exploit one or more properties of an optical system to allow for the same infrastructure to be used to transmit more than one channel of information. With the move towards an optical long-haul telecommunications infrastructure backbone, the development of multiplexing techniques to meet and exceed the demands on data traffic has been a high priority in both academic and commercial circles. Continued high pace development has seen improvements to all facets of the optical communication network, including optical sources, modulators, data encoding architectures and fibre optics, all of which can be manipulated to get the most out of an optical communication system.

As the development continues in the communication sector, the same principles can be applied to photonic sensors. In this way, existing point sensing interferometric techniques can be expanded to achieve a multiplexed readout. Existing multiplexing techniques can be separated into four broad categories.

Temporal Multiplexing

Time-domain phase interrogation methods rely on pulsed or frequency swept sources, with spatial resolution limited by the physical pulse width or sweep period. This enables gating of optical signals based on the time-of-flight, illustrated in Figure 2.3, allowing for both multiplexed readout and rejection of spurious interference. The canonical time multiplexed sensing system is the optical time-domain reflectometer (OTDR). These systems use Rayleigh scattering excited by an optical pulse injected from one end of an optical fibre.

By gating based on the time-of-flight of the optical pulse, the Rayleigh scattering from a localised area of the test fibre can be isolated and measured. This technique can be extended to use Brillouin scattering, or in the case of continuous wave LIDAR, frequency modulation[27]. The bandwidth of these systems however is limited by the repetition rate, and averaging time required to extract phase information, reducing the measurement duty cycle. Readily adapting these methods for continuous readout at acoustic frequencies is therefore primarily hardware limited[34]

Spectral Multiplexing

Multiplexed acoustic measurements have also been demonstrated using wavelength division multiplexing techniques. As shown in Figure 2.4, these systems use spectral separation of signals to enable multiplexed interferometric measurements, with continuous wave operation and include using wavelength separation or unique RF frequency shifts. By filtering the desired wavelength, or demodulating at the correct RF frequency, the

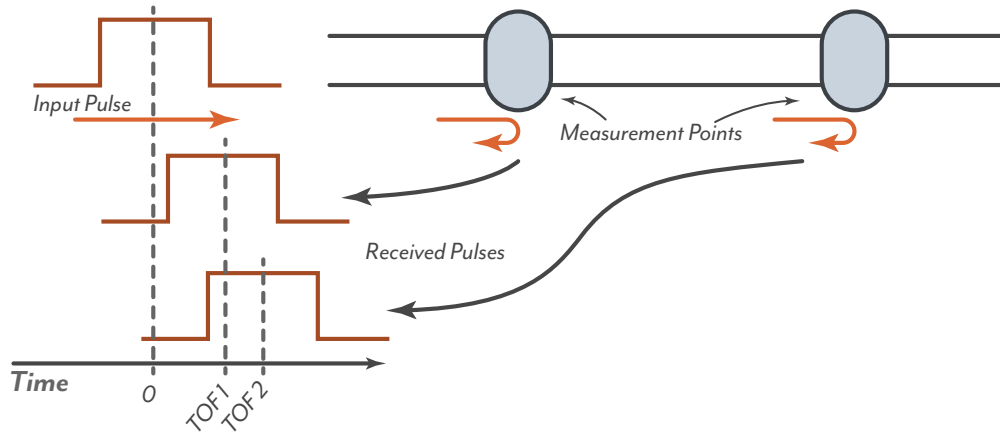


Figure 2.3: In temporal or time division multiplexed sensor architectures, a time-of-flight measurement is used to differentiate signals from spatially separated sensors. This may be done through pulses, as illustrated here, or using other time dependent modulation. As the signal identification is done through time-of-flight, multiple sensors at the same distance relative to the transmitter can not be distinguished.

signal of interest can be recovered. Methods for filtering out the wavelength of interest, using techniques such as add-drop optical filters draw heavily from the communications sector where wavelength division multiplexing is a mainstay for high throughput optical communications.

Such techniques have the required measurement bandwidth and sensitivity for acoustic sensing, and can achieve continuous wave, full duty cycle readout, as demonstrated by hydrophone and geophone arrays [31, 32, 35, 33]. However, there are two main technical challenges associated with wavelength division multiplexing. First, as signals are spectrally separate, this requires a unique optical filter for each readout channel. This in turn necessitates the use of individual detectors and optical sources or modulators. Scalability of these systems to include hundreds of sensors then becomes an increasingly difficult logistical challenge. Secondly, the transducers used for a wavelength division multiplexed system must also be wavelength selective, in order to impart a signal onto the correct wavelength channel. This adds a design restriction to the transducer itself, meaning specifically designed transducers are required.

Polarisation and Spatial Mode Multiplexing

Alongside signal manipulation in the time and frequency domain, multiplexing can be achieved by isolating and uniquely encoding orthogonal physical parameters of the optical beam. The first and more common instance of this is the encoding of orthogonal polarisation states. For optical communication networks, encoding the left and right handed polarisations separately allows for a two fold increase in data throughput[36].

Alongside polarisation multiplexing, the orthogonal optical spatial modes can be uniquely encoded[37]. This requires the use of higher order optical modes, restricting this to systems that use either multimode optical fibre or a free-space optical link. Furthermore, the independent manipulation of individual orthogonal modes necessitates the use of specialised phase masks or spatial light modulators (SLM). As the use of polarisa-

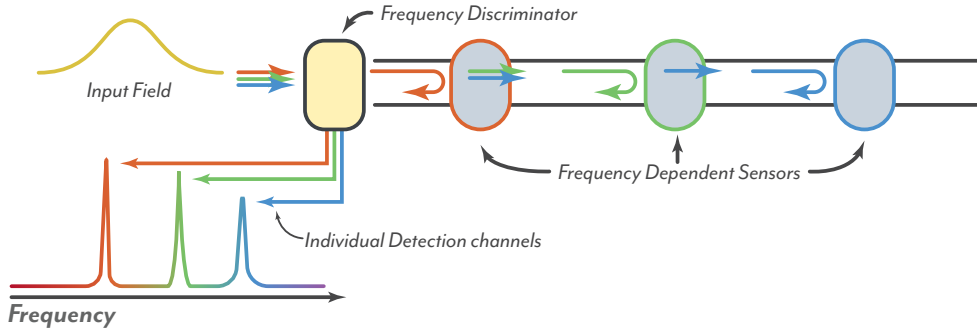


Figure 2.4: Spectral multiplexing distinguishes sensors based on optical frequency. These systems require a frequency discriminator to split the unique return frequencies from each sensor. Additionally the sensors themselves need to be frequency selective, which can be achieved through reflective gratings such as FBGs.

tion or spatial mode is independent of the amplitude, frequency or phase of the carrier field, these techniques can be used in conjunction with wavelength division multiplexing or code division multiplexing techniques. The main technical limit however remains the crosstalk due to depolarisation or spatial mode mixing[37].

Code Division Multiplexing

Code division multiplexing techniques use deterministic encoding of the optical field to either multiplex signals onto a single carrier or isolate individual signals using code orthogonality principles. Although there are many forms of code division multiplexing, we focus on the latter, including the use of spread spectrum techniques such as direct-sequence spread spectrum (DSSS) encoding. With these techniques, by using codes with favourable auto-correlation and cross-correlation properties, high isolation is achievable between adjacent measurement channels[38]. The use of such code division multiplexing is commonplace in telecommunications, and large components of the network infrastructure, namely the legacy code division multiple access (CDMA) wireless networks and the Global Positioning System (GPS) are reliant on the technique[39, 40].

Spread spectrum techniques are readily scalable, and can be coupled with existing wavelength division multiplexing (WDM) infrastructure to enable higher throughput and signal isolation through the same existing wavelength channels[40]. While optical code division multiple access (OCDMA) schemes are still being actively developed for telecommunications, the application of DSSS type modulation for metrology has also been pushed forward in a number of areas[41]. This includes using spread spectrum encoding to artificially, but deterministically broaden laser linewidths for quasi-white light interferometric applications, such as gyroscopes[42]. Alternatively, the correlation properties of pseudo random sequences have been employed in ranging applications and distributed sensors[43]. Digitally enhanced interferometry draws on concepts from both of these areas, allowing for multiplexed interferometric measurements to be made, with additional benefit of spurious interference rejection afforded by a spread-spectrum technique.

2.3 Digitally Enhanced Acoustic Sensing

Since its initial development, Digital Interferometric techniques have demonstrated both multiplexing capabilities and a high precision displacement sensitive readout. Notably, digitally enhanced heterodyne interferometry has demonstrated picometer scale sensitivities[3]. Furthermore, in certain regimes, cross-talk suppression between adjacent channels of 80 dB have been demonstrated at sub-audio band frequencies[4].

In scaling a sensing architecture to meet the bandwidth requirements of an acoustic sensor, concessions to averaging time and the code correlation properties have to be considered as the balance between readout bandwidth and crosstalk suppression must be kept. In this work, we use digitally enhanced heterodyne interferometry to demonstrate a multi-point acoustic sensing architecture in a free-space system. Through this process, we demonstrate audio band signal recovery from multiple sensors, with picometer scale sensitivity. Additionally we characterise the residual cross-talk between sensors and identify key limiting regimes which can inform the design of both free-space and fibre optic digitally enhanced sensing systems.

Digitally Enhanced Heterodyne Interferometry

Digitally Enhanced Heterodyne Interferometry superimposes multiplexing and ranging capabilities on top of conventional heterodyne interferometry by using pseudo-random binary sequences to uniquely encode the optical field. In this chapter, we introduce the basic principles of heterodyne interferometry followed by a description of the properties and generation of pseudo-random binary sequences. We finish with an analysis of the Digital Interferometric optical field and the required signal demodulation after the photodetector.

3.1 Heterodyne Interferometry

Heterodyne interferometry is a form multi-beam interference where the two interfering optical frequencies are offset, typically by a radio frequency shift. This has the effect of generating an optical beat at the intermediate frequency (IF) which carries the interferometric phase information. Here we consider a simple case study provided by a two beam Mach Zehnder interferometer shown in Figure 3.1. We can determine the intermediate frequency by explicitly calculating the optical field at the photodetector. We start from an input field split between two paths which we refer to as the signal and local oscillator (LO) paths respectively. The ratio of the split is governed by the transmission and reflection coefficients of the first beam-splitter, r_1, t_1 . We use the convention of a $\pi/2$ phase shift on transmission.

$$\begin{aligned} E_{in} &= \tilde{E}(t)e^{i\omega t} \\ E_S(t) &= r_1 \tilde{E}(t)e^{i\omega t} \\ E_{LO}(t) &= it_1 \tilde{E}(t)e^{i\omega t} \end{aligned}$$

Where $\tilde{E}(t)$ is the amplitude of the input field and ω , the optical frequency. Although symmetric, for clarity the heterodyne frequency shift is included as part of the LO path. This is introduced by a frequency shifter, for example, an acousto-optic modulator (AOM)

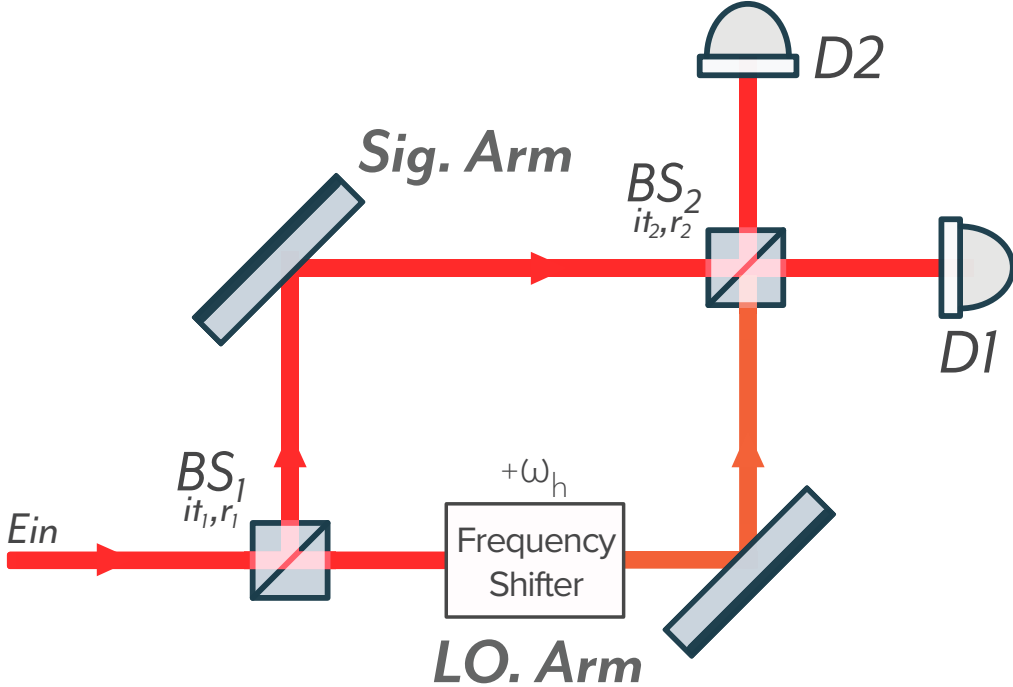


Figure 3.1: Two Beam Heterodyne Interferometry using a Mach Zehnder Interferometer. An input field is split by the first beam splitter (BS_1) which has reflectivity and transmission coefficients r_1 and t_1 respectively. The local oscillator (LO) arm is frequency shifted by an RF frequency ω_H . The two fields are recombined at the second beam splitter (BS_2) before measurement by photodetectors at the symmetric port (D1) or antisymmetric port (D2).

or an electro-optic modulator with seradyne modulation¹. The electric fields' contribution from each path immediately before the final beam-splitter can be then written as follows

$$E_S(t) = r_1 \tilde{E}(t) e^{i\omega t + i\phi_s(t)}$$

$$E_{LO}(t) = it_1 \tilde{E}(t) e^{i(\omega + \omega_H)t + i\phi_{LO}(t)}$$

Propagating through the final beam-splitter, the optical field at the symmetric port of the interferometer is then given by the superposition of the two input fields:

$$E_{D1}(t) = it_2 E_S(t) + r_2 E_{LO}(t)$$

$$E_{D1}(t) = ir_1 t_2 \tilde{E}(t) e^{i\omega t + i\phi_s(t)} + it_1 r_2 \tilde{E}(t) e^{i(\omega + \omega_H)t + i\phi_{LO}(t)}$$

Each path through the interferometer to the symmetric port consists of 1 beam-splitter reflection and one transmission, resulting in an identical common $\pi/2$ phase shift experienced by both signal and local oscillator paths. As this is a common phase shift, it has been omitted without loss of generality. If we assume a 50:50 splitting ratio for both

¹Seradyne modulation is where a linear phase ramp is generated at an RF frequency. This is equivalent to producing a fixed frequency offset at that modulation frequency

beam-splitters this reduces $r_1 = r_2 = t_1 = t_2 = \frac{1}{\sqrt{2}}$. Given the total field at the detector we can take the modulus square to calculate the incident optical power²:

$$P_{D1}(t) = \frac{|\tilde{E}(t)|^2(1 + \cos(\omega_H t + \Delta\phi(t)))}{2} \quad (3.1)$$

Where $\Delta\phi(t) = \phi_s(t) - \phi_{LO}(t)$ is the differential phase between the local oscillator and the signal arms. If we consider the Mach Zehnder in Figure 3.1, the phase difference is given by the differential arm length of the interferometer by the following expression:

$$\Delta\phi(t) = \frac{2\pi\Delta L}{\lambda}$$

Where ΔL is the path length difference between the signal and local oscillator paths of the interferometer. Similarly, the antisymmetric port optical power can be written as follows, and differs by a π phase shift due to the beam-splitter configuration:

$$P_{D2}(t) = \frac{|\tilde{E}(t)|^2(1 - \cos(\omega_H t + \Delta\phi(t)))}{2}$$

From the mathematical form of the photodetector output in Equation 3.1 we see that all the interferometric phase information is contained within the cross-term between the two fields. The key feature which affects the demodulation and subsequent readout of the interferometric phase is that the phase information is encoded at an intermediate frequency (IF). The IF frequency is equal to ω_H , the heterodyne optical frequency shift between the two interferometer arms.

The use of an IF frequency up-shifts the signal of interest out of the DC band which avoids low frequency noise features which is typically present in analog electronics. Extraction of the interferometric phase, $\Delta\phi(t)$ can be achieved through standard RF signal demodulation and extraction techniques such as IQ demodulation using a IQ lock-in amplifier[44], or continuous phase tracking using a phase locked loop (PLL) [8, 45]. With such techniques, heterodyne interferometry is able to achieve sub-wavelength resolution, with the noise floor of the demodulation architecture, or phasemeter typically well below other optical or electronic technical noise. Both IQ demodulation, and PLL phasemeters provide continuous phase tracking capability and are used throughout this thesis. For now, we will introduce and discuss the IQ demodulation phasemeter.

3.2 IQ Demodulation and Phase Extraction

IQ demodulation is a simple and robust method for continuous, sub-wavelength phase tracking. IQ demodulation uses phase locked sine and cosine radio frequency local oscillators to mix down an IF frequency. For simplicity of notation, we first normalise Equation 3.1 by the DC power, arriving at Equation 3.2:

$$P_{D1n}(t) = (1 + \cos(\omega_H t + \Delta\phi(t))) \quad (3.2)$$

²This expression is exact when $\tilde{E}(t)$ has units of $\text{W}^{1/2}$

The first stage of IQ demodulation is the mixing with the RF local oscillators. As the voltage signal generated by the photodetector is proportional to the incident optical power, we can use Equation 3.2 to write down this process as follows:

$$d_{cos}(t) = \cos(\omega_m t) P_{D1n}(t) \quad d_{sin}(t) = \sin(\omega_m t) P_{D1n}(t)$$

Where P_{D1} is defined in Equation 3.2 and ω_m is the (mixing) RF local oscillator frequency. The process of mixing with the RF local oscillators upshifts the DC component and downshifts the RF component at the mixing frequency. When the mixing frequency is matched to the IF frequency, in this case ω_H , the IF frequency is therefore shifted to DC. If we normalise to the photodetector power, we can expand out the mixing terms as follows:

$$\begin{aligned} d_{cos}(t) &= (\cos(\omega_H t) + \cos(\omega_H t) \cos(\omega_H t + \Delta\phi(t))) \\ d_{cos}(t) &= \underbrace{\cos(\omega_H t)}_{\text{DC Upshift}} + \underbrace{\frac{1}{2} \cos(2\omega_H t + \Delta\phi(t))}_{\text{IF Upshift}} + \underbrace{\frac{1}{2} \cos(\Delta\phi(t))}_{\text{IF Downshift}} \\ \\ d_{sin}(t) &= \sin(\omega_H t) + \sin(\omega_H t) \cos(\omega_H t + \Delta\phi(t)) \\ d_{sin}(t) &= \underbrace{\sin(\omega_H t)}_{\text{DC Upshift}} + \underbrace{\frac{1}{2} \sin(2\omega_H t + \Delta\phi(t))}_{\text{IF Upshift}} + \underbrace{\frac{1}{2} \sin(\Delta\phi(t))}_{\text{IF Downshift}} \end{aligned}$$

This is followed by a low pass filter (LPF) to remove high frequency upshifted components. The resultant output from the LPF are the inphase (I) and quadrature (Q) components of the IF tone.

$$\begin{aligned} I &= d_{cos}(t) = \cos(\Delta\phi(t)) \\ Q &= d_{sin}(t) = \sin(\Delta\phi(t)) \end{aligned}$$

The phase difference $\Delta\phi(t)$ can then be calculated by taking the arctangent of the ratio of quadrature and in-phase components:

$$\Delta\phi(t) = \tan^{-1} \left(\frac{Q}{I} \right)$$

Additionally, the amplitude of the input signal can also be determined through the following calculation:

$$\text{Amplitude} = \sqrt{I^2 + Q^2}$$

A functional diagram of the IQ demodulation architecture is shown in Figure 3.2. If we consider the spectral effect of this process, it is equivalent applying a lock-in amplifier at the IF frequency with a bandpass filter FWHM equivalent to the LPF 3dB point.

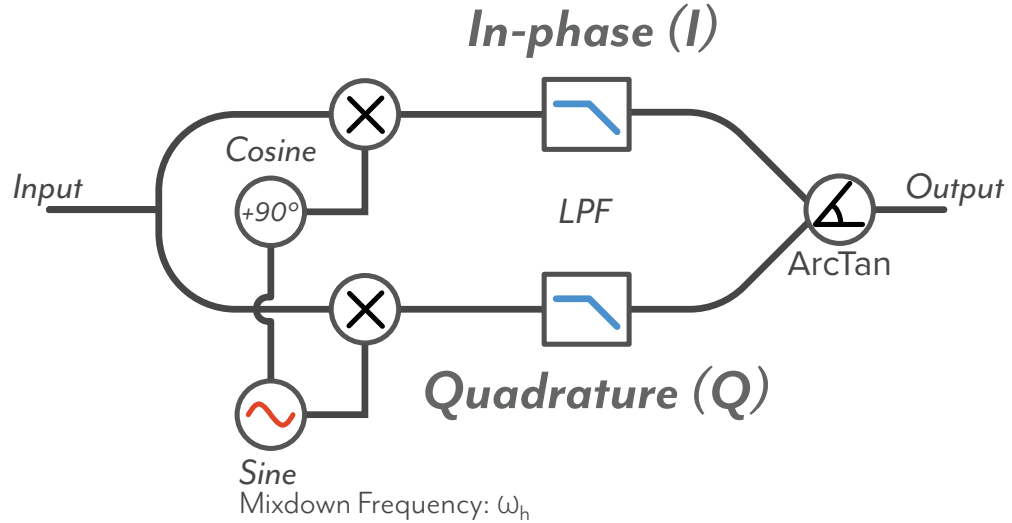


Figure 3.2: The functional diagram for an IQ demodulation logic circuit. We mix the input frequency down to DC using phase locked sine and cosine functions. Low pass filtering (LPF) removes any higher harmonics generated by the mixing process ensuring only the DC component remains. Mixing with both functions forms a complete orthogonal basis therefore, through the I and Q projections of the input frequency we can extract both amplitude and phase. As we are primarily interested in a phase readout, we compute the arctangent of Q/I in order to recover the angle.

3.3 Pseudo-Random Modulation Sequences

Pseudo random modulation sequences are a broadly used digital signals technique which have become common place in the age of high receiver count wireless communications. Using these sequences, applications such as the Global Positioning System or the CDMA telecommunication networks are able to uniquely identify, separate and demodulate signals for multiple users, while incorporating a high level of immunity to spurious reflections and interference. This is all achieved through the correlation properties of the pseudo-random sequences employed by these applications[46].

Analogously to GPS, the cornerstone of digital interferometry are the modulation sequences or codes used to produce the necessary auto-correlation and cross-correlation between the relevant signals. In the case of digital interferometry, the pseudo random sequence is used for ranging and gating optical fields based on a time-of-flight using a single master code. As only a single code is used, a pseudo-random sequence with a strong auto-correlation is to maximise the gating and signal isolation provided by the time-of-flight measurement.

Given these operating requirements, digital interferometry in this thesis, and more broadly [1, 4, 3, 8, 47], typically uses the maximal length pseudo-random sequence (m-sequence). In other subsets of digital interferometry, such as Digitally Enhanced Wavefront Sensing, other generating codes have been used including Hadamard and Gold Codes [9]. Furthermore, multiple m-sequences can be combined to generate four-level modulation schemes that are used for digitally enhanced homodyne interferometry as discussed later in this thesis.

3.3.1 Definitions

Before we proceed it is prudent to list several definitions which are used throughout this thesis when referring to pseudo random sequences and digital interferometry.

PRN	Pseudo Random Noise, which in the context of Digital Interferometry and this thesis refers exclusively to m-sequences.
Code	Also referred to as <i>Sequence</i> . This corresponds to a specific pseudo random sequence used for either modulating or decoding
Code Bit Depth	The code bit depth is defined by highest order term in the characteristic polynomial representing the sequence. It determines the number of elements in the code, as given by the <i>Code Length</i>
Chip	Also referred to as <i>symbol</i> . This is a single element of a PRN code.
Code Length	The total number of chips before the code repeats. It is dependent on the code bit depth, N , through the relation $L_{\text{code}} = 2^N - 1$.
Chip Frequency	Also referred to as the <i>modulation frequency</i> . The frequency at which a new chip/symbol is generated, modulated or decoded
Code Repetition Rate	Also referred to as <i>code frequency</i> . The frequency at which the code repeats when generated at a specific chip frequency. It is the inverse of the <i>code period</i> . It is given by the relation $f_{\text{code}} = f_{\text{chip}}/L_{\text{code}}$
Chip Length	The physical distance covered by a single chip. This is dependent on the speed of the modulated field, in this case, light and the chip frequency. The chip length for an optical beam in vacuum is given by $L_{\text{chip}} = c/f_{\text{chip}}$

Correlation properties of M-sequences

The key advantage of m-sequences, and the reason for their use in Digital Interferometry are their strong auto-correlation properties. For an n-bit sequence, the length of the sequence before repeating is given by the code length, $L_{\text{code}} = 2^n - 1$. Within a code length, the sequence will contain 2^{n-1} ones and $2^{n-1} - 1$ zeros. The auto-correlation of the sequence is given by computing the element-wise multiplication with a delayed copy of the sequence and integrating over the code length[5, 46]. We can write this in the discrete time picture as follows

$$A(\tau) = \sum_{t=1}^{L_{\text{code}}} c(t)c(t - \tau)$$

Where τ is the relative delay between the received code and the demodulation code. Evaluating this as a function of delay we find the autocorrelation takes on two values [48]

$$A(\tau) = \begin{cases} 2^n - 1 & \text{for } \tau = 0, L, 2L \dots \\ -1 & \text{for other } \tau \end{cases}$$

From this we see that the peak correlation is equivalent to the code length, and is determined by the bit depth of the code. Plotted as a function of the delay τ , Figure 3.3 shows that there is one peak correlation per code length, and it is ± 1 chip in width.

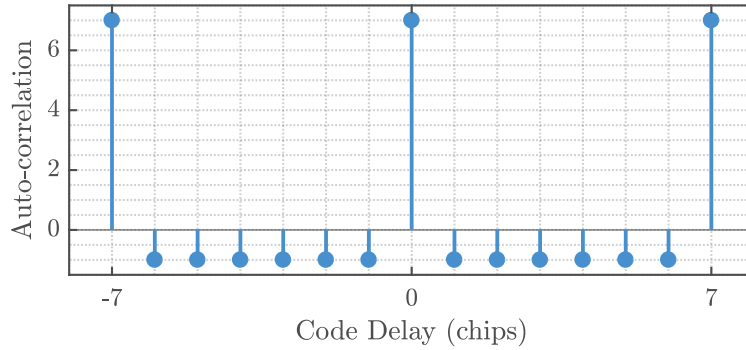


Figure 3.3: The computed auto-correlation of a 3-bit (7 chip) m-sequence as a function of the relative delay in chips. The peak correlation only occurs if the two codes are in phase modulo code length (7 chips). At all other delays the auto-correlation is -1. The magnitude of the peak correlation is equal to the code length of 7 chips.

In practice, when a received signal is encoded with an m-sequence, the peak in the auto-correlation can be used to unambiguously identify the delay τ , and therefore the absolute range to the target. Conversely, decoding with a demodulation code set to a specific delay can then be used to reject signals at all other delays, by virtue of the low value for $A(\tau)$ at other delays.

Generating M-sequences using Linear Feedback Shift Registers

The generation of m-sequences is done through the use of linear feedback shift registers (LFSR). These are linear recursive operations which transform an existing or original ‘state’ vector to a new state which becomes the input for the subsequent iteration[49]. The core operation is an XOR operation between two or more elements of an input vector, as shown in Figure 3.4. The position of the feedback ‘taps’ determines which elements are to undergo the XOR operation. For the tap positions given in Figure 3.4, the corresponding m-sequence is shown in Figure 3.5. In a digital implementation, the XOR operation is computed through a modulo-2 addition of the two input values[50].

We can describe the LFSR generator through a characteristic polynomial. This irreducible function carries information regarding the position of the LFSR taps and the length of

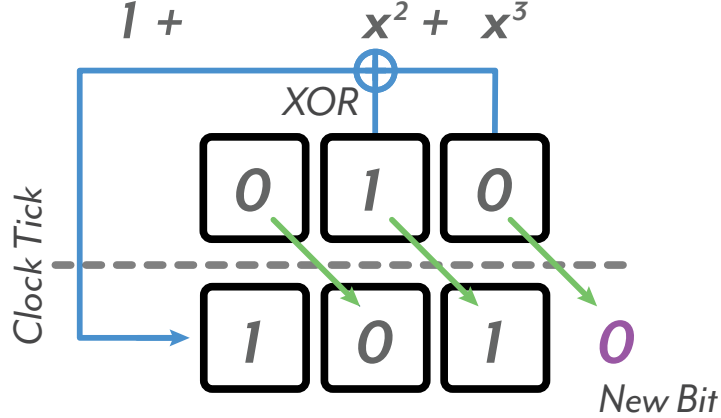


Figure 3.4: Functional diagram of a 3 bit linear feedback shift register built using the characteristic polynomial $f(x) = x^3 + x^2 + 1$. Every clock tick the exclusive OR (XOR) of the 2nd and 3rd bits is computed. On the following clock cycle, all bits are circularly shifted with the XOR output becoming the new least significant bit. The most significant bit is expelled as the new code symbol (chip).

the m-sequence and thus can be used to completely describe the LFSR generator and the subsequent m-sequence[51]. We can write the characteristic polynomial in the form:

$$f(x) = x^n + a_{(n-1)}x^{(n-1)} + a_{(n-2)}x^{(n-2)} + \dots + 1$$

Where a_i is either zero or one for each order. The highest order component x^n is determined by the bit depth of the generated m-sequence. From this we can immediately calculate the code length, $L_{\text{code}} = 2^n - 1$ and auto-correlation maximum. The remaining non-zero orders determine the position of the LFSR taps. In our example shown in Figure 3.5, the full characteristic polynomial can be written as follows:

$$f(x) = x^3 + x^2 + 1$$

From this we can immediately see that the highest order is $n = 3$, meaning the sequence is a 3 bit sequence. The length of the sequence is therefore $L_{\text{code}} = 2^3 - 1 = 7$, which corresponds to the number of code symbols before the sequence repeats. Lastly, we know that the position of the XOR is between the 2nd and 3rd elements of the input state.

In Digital Interferometric applications, higher bit depth sequences are typically used. The characteristic polynomials and LFSR circuits for these sequences are readily available through published resources [52].

3.4 Digitally Enhanced Heterodyne Interferometry

Digitally Enhanced Heterodyne Interferometry (DEHeI) combines the sub-wavelength resolution of heterodyne interferometry with the correlation properties of the M-sequences discussed in the previous two sections. The combined technique consists of the modulation stage in which the modulation signal is generated and imprinted onto the optical beam. The second stage is the signal extraction which handles decoding of the pseudo-random noise (PRN) code and demodulation of the recovered optical beat. Both of these processes

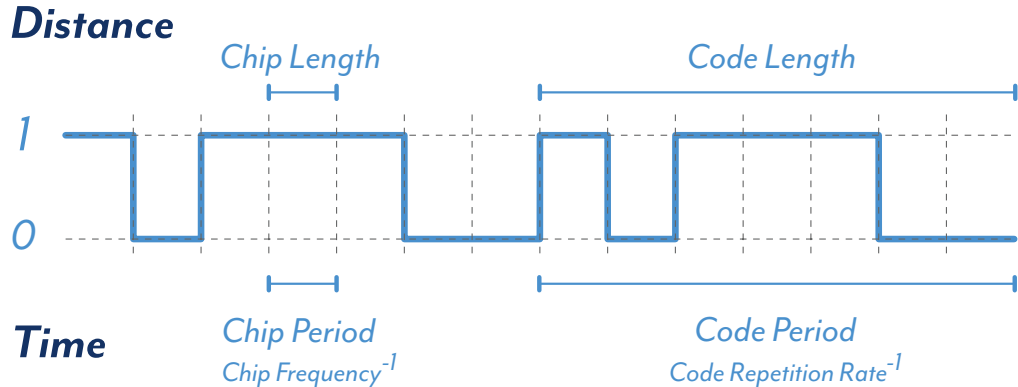


Figure 3.5: A simulated 3 bit binary Pseudo Random Noise (PRN) sequence generated using the LFSR in Figure 3.4. The sequence consists of 7 elements (chips) before repeating. In a system, the code is modulated at a fixed rate, determining the chip frequency and by extension the code repetition rate. As we modulate onto an optical field, we use the speed of light in the medium of propagation to determine the physical distance corresponding to the chip length and physical code length.

require the use of real-time digital signal processing resources, for which we exclusively use field-programmable gate arrays (FPGAs). The following sections go through the details of modulating and demodulating pseudo-random binary phase modulation in an optical system.

Modulating the Optical Beam

Before moving to the optical system, the PRN code must be generated. The generation of the PRN code is carried out using the LFSR method discussed in Section 3.3, after which it is then modulated onto the metrology beam through a phase shifter. The phase shifter converts the binary PRN code and maps it from zero to the modulation depth specified and is added into the optical system at the start of the signal arm of the interferometer as shown in Figure 3.6.

The main considerations when choosing a phase shifter for encoding a Digital Interferometry (DI) code is required bandwidth, which is typically on the order of 100 MHz, and the accuracy and stability of the two level phase jump. For these reasons, an electro-optic modulator (EOM) is favoured, as shown in Figure 3.6.

The introduction of the EOM also modifies the optical field in the signal arm of the interferometer by applying an additional phase modulation to the signal arm optical field. If we consider the point immediately following the EOM, the optical field in the signal arm is as follows:

$$E_S(t) = r_1 \tilde{E}(t) e^{i\omega t + i\phi_s(t)} e^{i\beta c(t-\tau_1)} \quad (3.3)$$

Where β is the modulation depth of the PRN code. The modulation speed of the code is given by the chip frequency; the number of chips per second. The optimal modulation

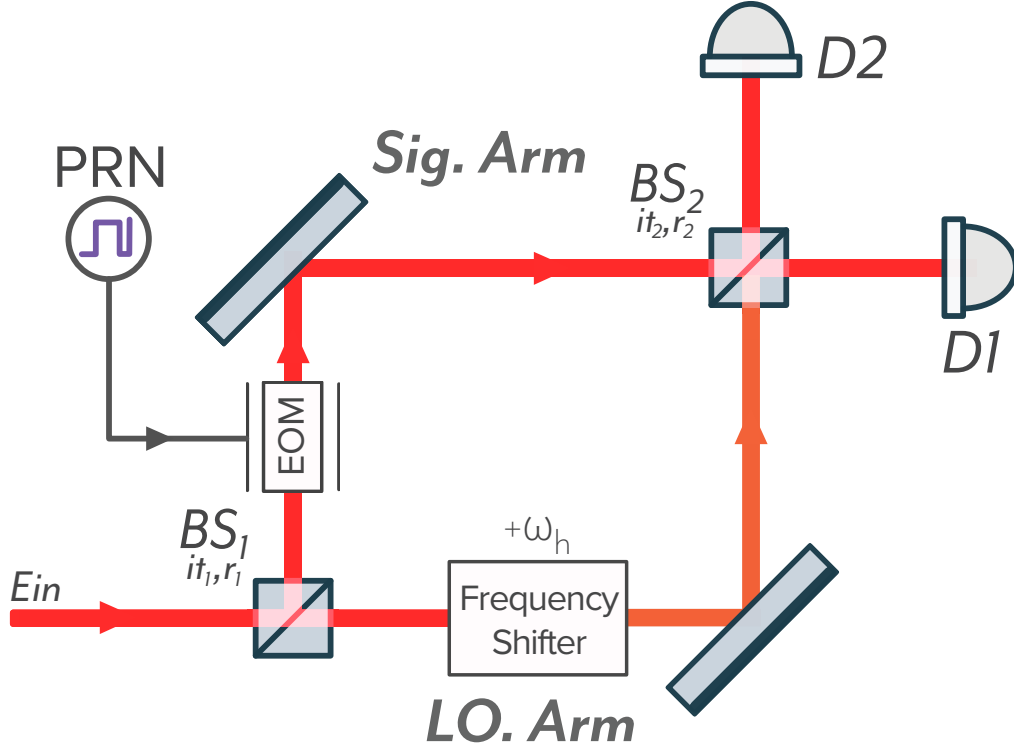


Figure 3.6: In order to introduce a digital interferometric readout, we include a phase shifter in the form of an electro-optic modulator (EOM) into the signal arm and apply a PRN code as a direct phase shift, optimally between 0 and π modulation depth. The remainder of the optical setup is identical to Figure 3.1.

depth of DEHeI applications is a π phase shift. Diverging away from the π modulation depth results in incomplete or partial decoding during the demodulation process, yielding sub-optimal signal isolation and additional noise coupling[8]. Substituting in the optimal modulation depth of π , we can simplify the field output, bringing the code out from the exponent. We can further simplify the expression by writing the code in a bipolar form (± 1), given by the following expression: $p(t - \tau) = 2c(t - \tau) - 1$. Substituting this into the optical field in Equation 3.3 yields:

$$\begin{aligned} E_S(t) &= r_1 \tilde{E}(t) e^{i\omega t + i\phi_s(t)} e^{i\pi c(t - \tau_1)} \\ E_S(t) &= r_1 \tilde{E}(t) p(t - \tau_1) e^{i\omega t + i\phi_s(t)} \end{aligned}$$

In order to determine the optical power on the photo-detector, we can follow a similar procedure to Section 3.1. With the revised signal optical field containing PRN modulation, we interfere it with the same local oscillator field from Section 3.1. This yields the following total electric field at the symmetric port of the interferometer:

$$E_{D1} = ir_1 t_2 \tilde{E}(t) p(t - \tau_1) e^{i\omega t + i\phi_s(t)} + it_1 r_2 \tilde{E}(t) e^{i(\omega + \omega_H)t + i\phi_{LO}(t)}$$

We compute the detected optical power by taking the modulus square of the field at $D1$. We again assume 50:50 splits at both beam-splitters:

$$P_{D1} = \frac{|\tilde{E}(t)|^2(1 + p(t - \tau_1) \cos(\omega_H t + \Delta\phi(t)))}{2} \quad (3.4)$$

Whereas in the conventional heterodyne interferometry case we see an optical beat at the heterodyne frequency, ω_H , the PRN modulation results in a spread spectrum response, as shown in Figure 3.7. As the signal is entirely contained within the RF component, we AC couple the output in Equation 3.4 resulting in the following expression for the PRN encoded signal.

$$s(t) = p(t - \tau_1) \cos(\omega_H t + \Delta\phi(t))$$

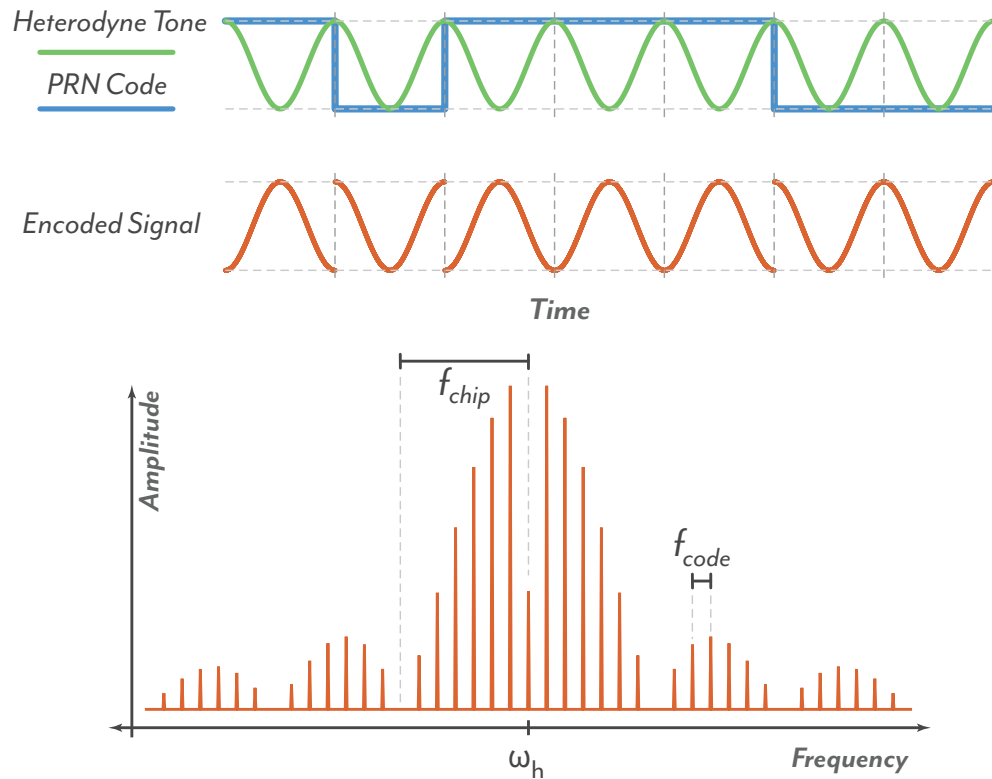


Figure 3.7: We simulate a 3 bit PRN code modulated onto a phase locked heterodyne beat note. The fourier transform of the encoded signal demonstrates the structure of the spread-spectrum response. The sidebands have a sinc^2 response, with nulls occurring at multiples of the modulation (chip) frequency. The spacing between successive sidebands is equal to the code frequency, which can be expressed in terms of the chip frequency and code length by: $f_{code} = f_{chip}/L_{code}$

Digital Decoding and Optical Beat Recovery

The spread-spectrum output from the photodetector requires decoding in order to recover the IF signal from a conventional heterodyne interferometer. The decoding process is done on the same FPGA system used to generate the original codes to ensure that the entire digital signal chain is operating on a common clock. Discarding the DC components of the photodetector output, the RF spectrum, $s(t)$ is correlated against a locally generated demodulation PRN code $p(t - \tau_d)$. The demodulation code is identical to the code originally modulated on the optical field, however it is tuned to an arbitrary delay, τ_d . This yields the following expression for the demodulated output:

$$d_1(t) = \sum_{n=1}^{L_{\text{code}}} s(t)p(t - \tau_d)$$

$$d_1(t) = \sum_{n=1}^{L_{\text{code}}} p(t - \tau_1)p(t - \tau_d) \cos(\omega_H t + \Delta\phi(t))$$

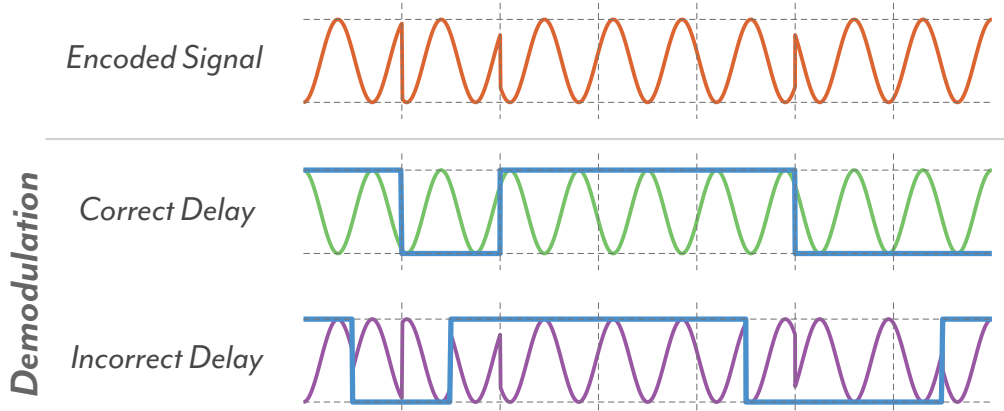


Figure 3.8: A received digitally encoded heterodyne beat note is decoded by applying a demodulation PRN code. When the demodulation code is in phase with the received code, it is correctly decoded, restoring the heterodyne beat note. If the demodulation delay is out of phase with the received code, this process has the effect of re-encoding the heterodyne beat note, which remains a spread-spectrum. In the former case, integration over the code length leads to amplification with gain corresponding to the code length, while in the latter, it averages to -1. When multiple codes are present in the encoded signal, only the heterodyne beat note, and accompanying phase information of the decoded delay is restored.

An intuitive way to visualise this process is illustrated in Figure 3.8. When the decoding PRN code is aligned with the received code, the decoding removes the π phase shifts, restoring the optical beat. If the decoding sequence is out of phase with the received code, the decoding sequence effectively re-encodes the received signal $s(t)$ with an additional PRN sequence. The decoding is completed by integrating over the code period. Integrating over the code period averages over all elements of the code. Due to the correlation properties discussed in Section 3.3, the integration process increases the amplitude of the correctly decoded signal up to $2^n - 1$ while incorrectly decoded signals average to -1. Ap-

plying the correlation conditions to the decoded output results in recovery of the optical beat, as per conventional heterodyne interferometry:

$$d_1(t) = \begin{cases} L_{\text{code}} \cos(\omega_H t + \Delta\phi(t)) & \text{for correctly decoded signals } \tau_d = \tau_1 \\ -\cos(\omega_H t + \Delta\phi(t)) & \text{for incorrectly decoded signals } \tau_d \neq \tau_1 \end{cases}$$

From the decoding process we see that signals which are incorrectly decoded are suppressed by a factor of L_{code} . Spectrally, the decoding process restores the spread-spectrum PRN encoded signal back to a single frequency tone at the heterodyne frequency of the interferometer.

Following the decoding process, the output from $d_1(t)$ is passed onto a phasemeter, such as the IQ demodulator discussed previously. In practice, the integration of the code length, L_{code} is combined with the low pass filter used for the IQ demodulation to most effectively utilise DSP resources and reduce potential aliasing. In the event of multiple signal fields with unique time delays, the decoding process can be parallelised by using a unique decoding delay for each parallel path, producing parallel demodulated outputs $[d_2(t), d_3(t) \dots d_i(t)]$. In this way multiple signals can be separately decoded and individual phase signals extracted.

Multipoint Acoustic Sensing Array

Interferometric acoustic sensing allows for the readout and measurement of sub-wavelength level displacement signals. When combined with the multiplexing and signal gating capabilities of digital interferometry, we can develop sensing architectures which enable multiple simultaneous readouts while retaining full interferometric sensitivity for each unique sensor. In this chapter, we highlight the design and initial characterisation of a multiplexed interferometric acoustic sensing system based on a digital interferometric readout.

4.1 Conceptual Design

The concept behind this acoustic sensing design is to have a single frequency free-space optical beam interrogate multiple partially reflective surfaces, as shown in Figure 4.1. At each surface, an interferometric measurement is made to determine the time varying displacement with the gating of individual reflections from the interrogation arm achieved through the use of digital interferometry. We can, based on these conditions, define a number of performance specifications for the system.

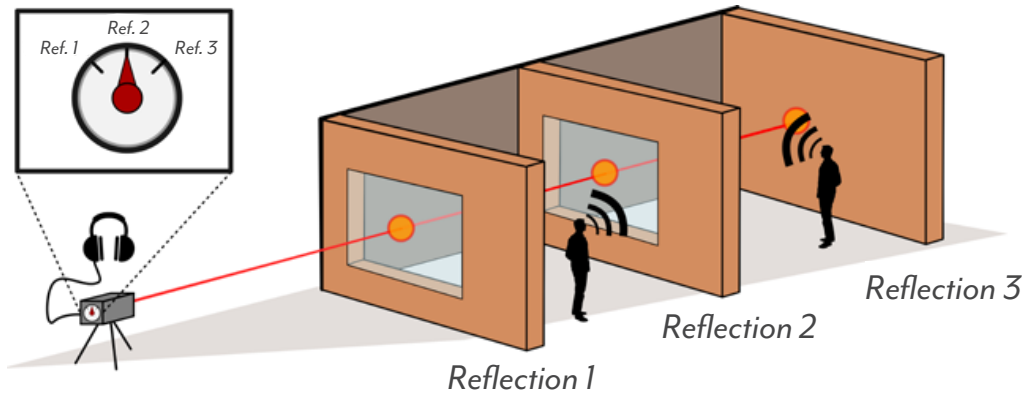


Figure 4.1: The multiplexed acoustic sensing concept. While fibre optic systems are commonplace, for this demonstration we choose a free-space ranging and acoustic sensing system. The signal arm of the interferometer is set to interrogate three partially reflective surfaces (Ref. 1 - Ref. 3), each with unique acousto-vibrational signals. Through the experiment we aim to characterise the sensitivity and cross-talk suppression achievable in such a free-space system.

Readout Bandwidth

The readout bandwidth is dependent on the code averaging required for digital interferometry and therefore can be increased by increasing the chip frequency or reducing the code length.

Ranging Resolution

The ranging and gating resolution is dependent on the chip length, and thus a smaller ranging window can be made by reducing the chip length. This can only be achieved by increasing the chip frequency. In order for the system to be developed on a standard size optical table ($1.2\text{m} \times 2.4\text{m}$), we require better than ≈ 2 metre resolution.

Ambiguity Range

The ambiguity range of the system is dependent on the code length and the chip length and can be represented by the physical distance occupied by the code. Beyond this, the code will wrap, no longer decoding at a unique delay

Displacement Sensitivity

The displacement sensitivity is dependent on the interferometric readout and therefore is primarily effected by technical noise from the laser, photodetector, digitisation electronics and quantisation noise of the demodulation process and fundamental shot noise.

Crosstalk Suppression

The suppression of a rejected or gated signal relative to the same signal when correctly decoded. This determines how effective the decoding process is at rejecting unwanted signals from the readout.

During the course of the experimental implementation we either specify or characterise the performance of each of these metrics. We use a modified Mach Zehnder as the fundamental optical architecture, with the signal arm used to interrogate three reflection surfaces, as depicted in Figure 4.1. The details of the experimental implementation are discussed in the following section.

4.2 Experimental Implementation

In the experimental demonstration we were able to isolate and measure the phase and subsequently displacement of four in-line reflective surfaces up to a Nyquist frequency of 10 kHz. The system, shown in Figure 4.2, used an Orbita Lightwave 1550 nm fibre coupled laser, split between an interrogation arm and a local oscillator. The local oscillator (LO) was frequency shifted by 40 MHz using an IntraAction FCM-401E5A acousto-optic modulator (AOM), producing a heterodyne beat which was demodulated at the output. The heterodyne beat is spectrally broadened using a PRN code phase modulated onto the interrogation arm implemented by a Photline MPZLN-10 electro-optic modulator (EOM).

In post-processing, the PRN code was be demodulated with a digital copy of the code. By applying a pre-determined delay to the demodulation code, we enable the recovery of the heterodyne beat for the optical time-of-flight corresponding to the four unique delays present in the system. The spatial resolution of the gating is dependent

on the symbol rate of the modulated code. The chip frequency of the PRN code in this demonstration was 125 MHz, corresponding to a 2.4 m spatial resolution in air. Once tagged with the PRN code, the interrogation arm was collimated into a free-space beam which interrogated the target reflectors.

The generation of the local oscillator drive signal and PRN code was handled by a high speed field-programmable gate array (FPGA) manufactured by National Instruments (NI 7966R) coupled with high speed digital-to-analog converters (DACs), with an analog bandwidth of 200 MHz (500 MS/s) (NI 5782 Transceiver)[53, 54]. Following the digitisation of the photodetector output at 250 MS/s, the FPGA was used to apply the delayed decoding PRN code to recover the heterodyne beat at each of the four delays. Subsequently, the recovered IF tone was demodulated using an IQ demodulation. Data was streamed to a networked PC at 10.2 kHz per demodulation channel. Data recording was handled by the computer with phase extraction done in post-processing in MATLAB.

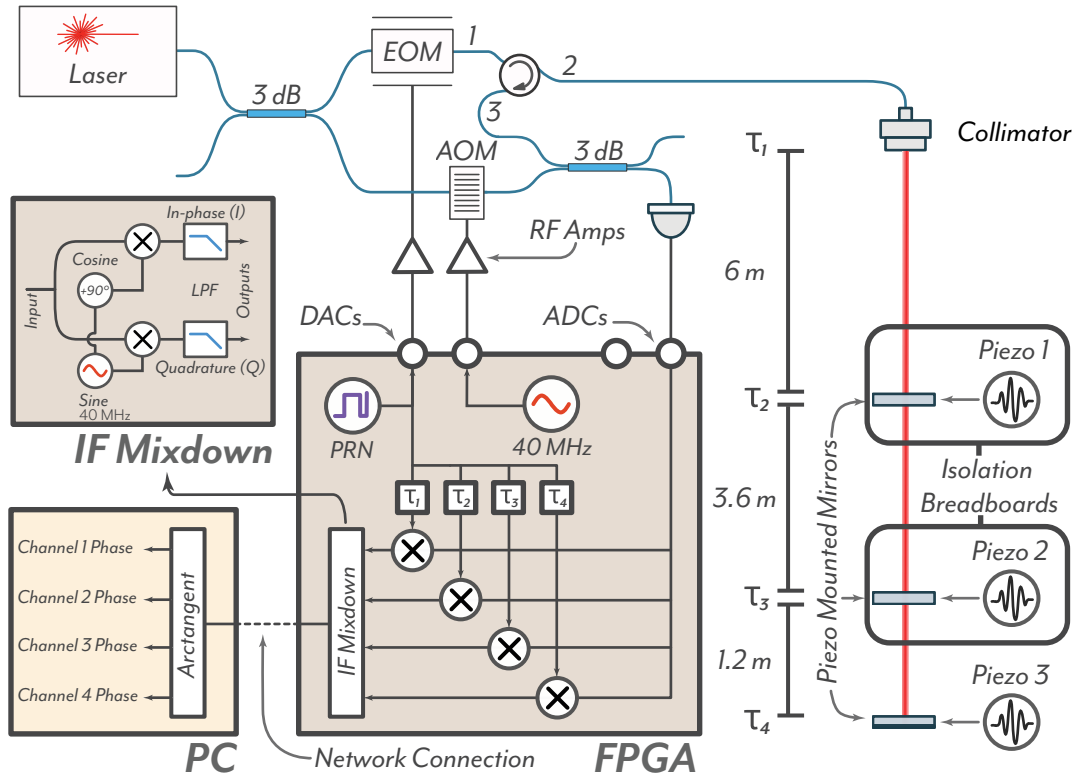


Figure 4.2: The experimental layout can be split into the input optics, free-space optics and digital components. The input optics, including both EOM for PRN phase modulation and AOM for LO frequency shifting are fiber coupled. The collimator sends the PRN encoded interrogation beam through three free-space piezo actuated reflectors, with a fourth reflection provided by retro-reflection from the collimator itself. The return signal is separated using a circulator and recombined with the LO before detection. After digitization, the heterodyne signals for each reflection are recovered by mixing with appropriately delayed PRN codes. The recovered heterodyne beat notes are passed to separate IF mixdown processes. This is done in parallel for all four reflections, all in realtime on a FPGA. The outputs are passed to a networked host computer and recorded to disk and in post-processing the phase is recovered through the arctangent operation.

The optical setup for this experiment was constructed on a mechanically damped optical bench using coated glass plates with approximately 40% reflectivity to act as intermediate reflection surfaces, shown in Figure 4.2. The final, rear reflector was a piezo mounted high reflectivity mirror. All reflectors were mounted on low voltage piezo-electric transducers, allowing for the injection of up to three unique acoustic signals into the system. A photograph of the two partial reflectors and the rear retro-reflector are shown in Figure 4.3.



Figure 4.3: Photograph of the two types of piezo mounted reflectors used in the experiment. Piezo 1 and piezo 2 are actuating on partially reflected glass slides and piezo 3 is actuating on a standard 1 inch mirror

The spacing between the reflectors was optimised to ensure that multiple round-trips of an optical path length did not match path lengths of subsequent reflectors in the beam path. In order to get sufficient path length within the confines of the optical table, the beam was folded from the collimator as shown in Figure 4.4. As shown in the Figure, the two inline reflectors were mechanically isolated from each other, and the other two reflectors by mounting them onto to individual Sorbathane isolated breadboards to reduce mechanical cross-coupling.

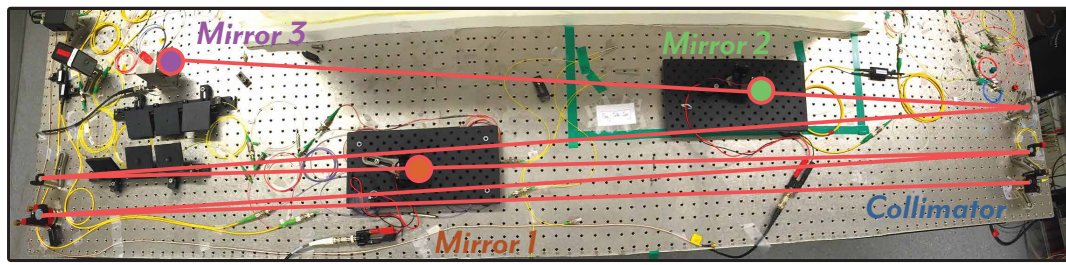


Figure 4.4: A photograph of the optical table showing the highlighted optical beam path. The beam has to be folded along the optical table in order to achieve the necessary distances

Each reflector in the interrogation arm was driven by a unique audio frequency signal through the piezo-electric transducer. The resultant displacement of the reflectors was measured through the induced optical phase shift. On the FPGA, multiple demodulation PRN codes were generated simultaneously, each at differing delays, allowing for the con-

current demodulation of the four reflection surfaces. Although a total of four simultaneous demodulation channels were demonstrated in this work, this number was not a limit of the signal processing and further demodulation channels may be added as required.

4.3 PRN Code Aliasing Effects

In the majority of digital interferometry applications, the chip frequency and the heterodyne frequency are matched to ensure optimal, synchronous averaging during the demodulation process. However, in this system, in order to achieve the necessary bandwidth and spatial resolution we use a PRN code chip frequency of 125 MHz, which is 3.125 times faster than the heterodyne frequency of 40 MHz.

During the early testing of the system, we were subject to aliasing effects which manifested themselves as large single frequency peaks in the output phase spectrum. An example spectral density demonstrating the peaks is shown in Figure 4.5.

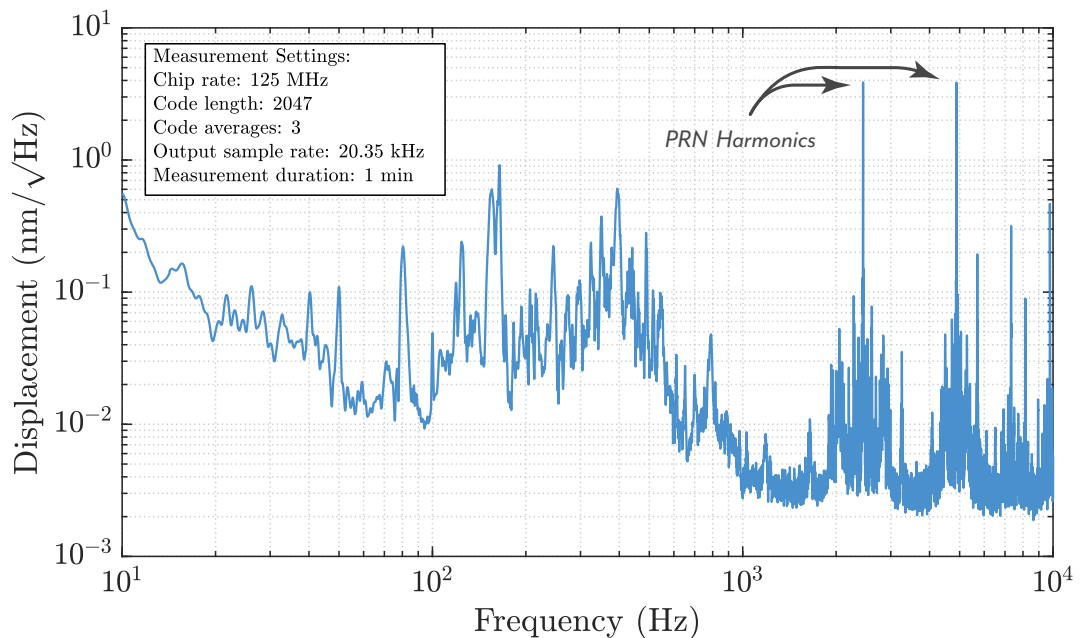


Figure 4.5: Amplitude spectral density showing the harmonics due to PRN modulation. The effect is a by-product of the decoupled PRN chip frequency and the heterodyne frequency of the system. The tones are tunable by adjusting either of the aforementioned parameters.

We determined that these were caused by the large frequency difference between the two main operating frequencies of the system. Firstly, the peaks were removed when the digital system was switched off, and the system was running with a conventional heterodyne interferometer readout. Secondly, with digital interferometry active, the peaks were tunable by shifting the heterodyne frequency.

From this, it was possible to conclude that the aliasing effect was due to the residual DC component from the photodetector being upshifted to the heterodyne frequency ω_H . This was then aliased back into the measurement band resulting in peaks in the kHz range.

We can write the relation between the heterodyne frequency, chip frequency, code length and aliased harmonic frequency as follows

$$f_{\text{Harmonic}} = f_H - Nf_{\text{code}}$$

Where f_H is the heterodyne frequency, f_{code} is the code repetition rate and N is an integer multiplier. As all the frequencies are known, we can solve for N . Given this expression, and a tunable f_H , we can calculate the smallest shift to the heterodyne frequency such that the harmonics alias to DC. This removes the harmonics from the acoustic frequency band, however this method may not be appropriate if the sub-hertz band is of interest. In this case, the appropriate method is to optimise the system based on the additional constraint that the heterodyne and chip frequencies are matched.

4.4 The Three Signal Measurement

With the removal of the aliased harmonics, we are able to use the entire readout bandwidth. The results shown here utilise a Nyquist bandwidth of 10.2 kHz, however higher sampling frequencies, up to 2 MHz have been demonstrated, though not reliably. The main limitations in implementing faster data acquisitions are due to hardware constraints, including network traffic, hard drive write speeds and file format overheads. These are readily solvable technical challenges which were not fully optimised for this proof-of-concept demonstration.

The first proof-of-concept test was to record three separate audio signals from pieces of music, converted to displacement signals through the piezo transducers. The pieces of music used were the Bach Cello Suite 1 for the first piezo mirror, Dancing in the Moonlight for the second mirror and Shake Your Tailfeather for the rear mirror. The resultant audio has been presented as supplementary material attached to Figure 4.6, highlighting the isolation of each channel.

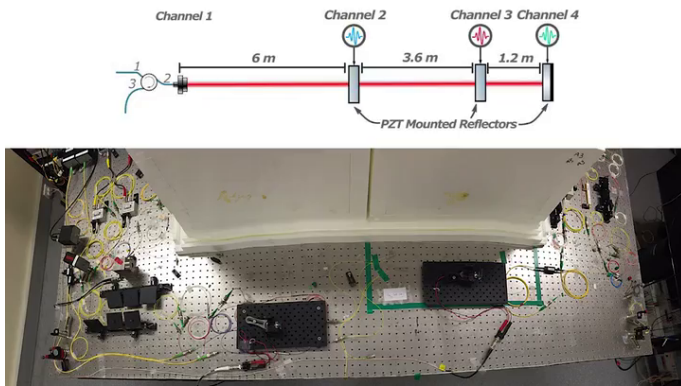


Figure 4.6: In the video (Supplementary Material: Visualisation 1) we demonstrate the signal fidelity and isolation of the readout through the recording of three unique musical pieces onto the three separate channels. We directly compare the DI signal extraction from Channel 2, 3 and 4 with a traditional heterodyne measurement of the system.

Alongside the readout from the three channels, an analogous measurement was done with the DI system deactivated. This is akin to a conventional heterodyne interferometric

readout and does not include any signal gating. From this comparison in the multimedia presentation of Figure 4.6, we hear both channel isolation and suppression of spurious interference effects such as fading when compared to the conventional heterodyne setup. A more quantitative analysis of the crosstalk coupling between different channels is discussed in the following chapter.

4.5 Transducer Response Measurements

As with all acoustic sensors, the frequency response of the system is critical for ensuring accurate reproduction of acoustic signals. In this system, the piezo actuated reflectors all had unique transfer functions with fundamental resonances below 1 kHz. The transfer function of the readout itself however was flat over the 10 kHz Nyquist bandwidth. Figure 4.7 shows the transfer functions of reflector 1-3 shown in trace (a)-(c) respectively. The flat transfer function of the readout has been omitted in Figure 4.7 for clarity.

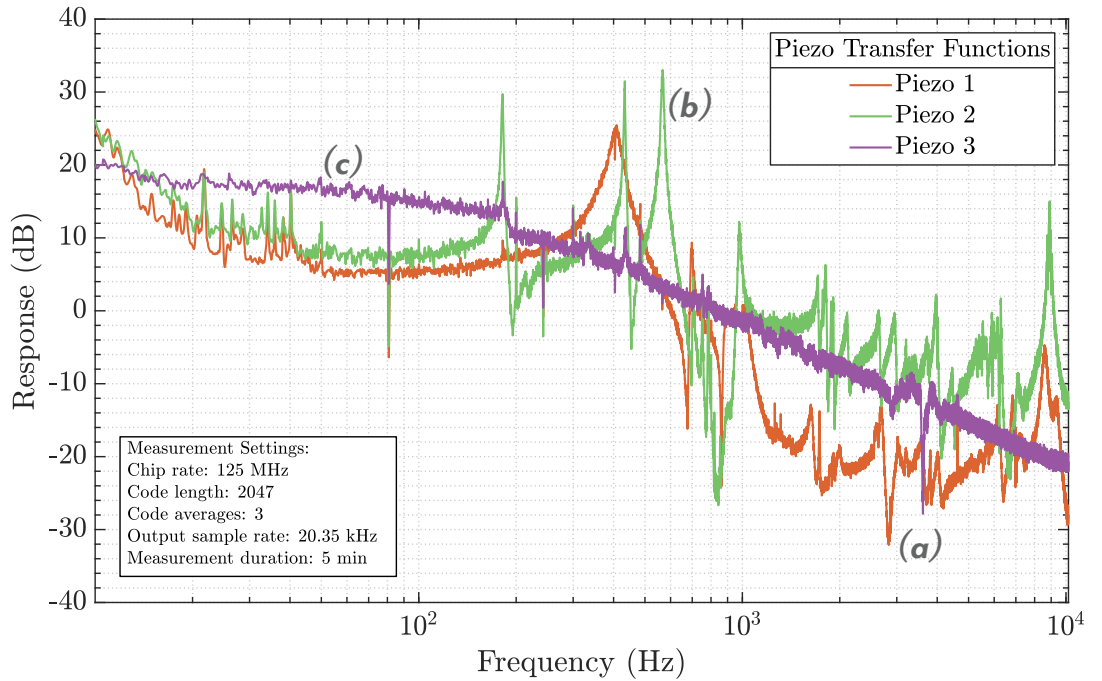


Figure 4.7: Measured transfer functions of the three PZT actuated mirrors (a)-(c).

The transfer functions were measured by injecting white noise generated using an Agilent signal generator into the system through the respective transducer. The readout transfer function was measured by phase modulating the local oscillator AOM to provide a direct differential phase shift to the interferometer. The piezo-reflector transfer functions were measured by injecting a white noise displacement signal directly through the mounted piezos. As the readout response was flat, we can infer that the frequency response is limited by the acoustic transducer used to couple the acoustic signal into a physical displacement.

4.6 Displacement Sensitivity

The displacement sensitivity of the readout will determine the response requirements for a transducer in an actual system. For an acoustic sensing system such as this, the transducers are fixed, therefore the displacement sensitivity determines which reflective surfaces are audible. In essence, a better displacement sensitivity would allow for signal extraction from lower response, poorly impedance matched acoustic transducers. The displacement sensitivity of the device was measured by calculating the amplitude spectral density of the background noise floor, shown in Figure 4.8 from a 1 minute time domain recording. The data was recorded under normal laboratory conditions, without any injected signals. We can see acoustic band pickup from 4 Hz to 1.5 kHz on the free-space channels, corresponding with ambient noise in the laboratory. This is reduced for channel 4 which had a larger inertial mass and therefore lower coupling. This pickup is altogether absent for channel 1 which corresponds with a measurement of the lead fiber noise in the system up to the collimator.

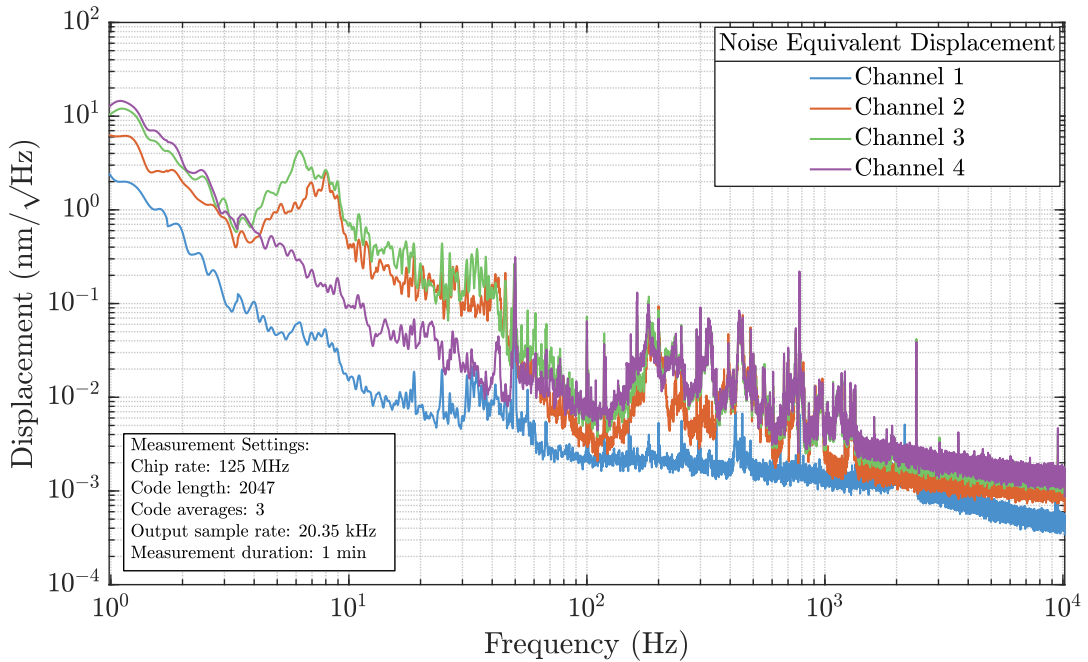


Figure 4.8: Amplitude spectral density measurement of the noise floor for each individual channel. Channel 1 shows the lead fibre noise measured up to the free-space collimator. Channel 2, 3 and 4 correspond with successive free-space reflectors, with Channel 4 having higher inertial mass, and therefore lower coupling of environmental noise. We see the ambient audio band pickup on all channels between 10 Hz and 1 kHz. The low frequency roll up below 10 Hz was measured to be caused by frequency noise of the laser. The high frequency noise floor reaches a displacement sensitivity on the order of $10 \text{ pm}/\sqrt{\text{Hz}}$.

Below 10 Hz we see a low frequency roll up in the noise equivalent displacement. This is attributed to laser frequency noise, which was independently measured using a fiber frequency reference [55]. Above 10 Hz we demonstrate the same performance as other DI systems reaching a noise floor on the order of $80 \mu\text{rad}/\sqrt{\text{Hz}}$ in phase, corresponding to a displacement sensitivity of $10 \text{ pm}/\sqrt{\text{Hz}}$ [3].

Crosstalk Characterisation & Limits

Cross-talk or channel isolation refers to the signal leakage into the channel of interest from another, unwanted source. All multiplexed systems, including digital interferometry, offer a finite amount of cross-talk suppression. We can measure the amount of cross-talk in a system by injecting a signal into one channel, and measuring the response in another channel. In this work, we use single frequency tones, taking the difference in the frequency domain as depicted in Figure 5.1 as our metric of merit.

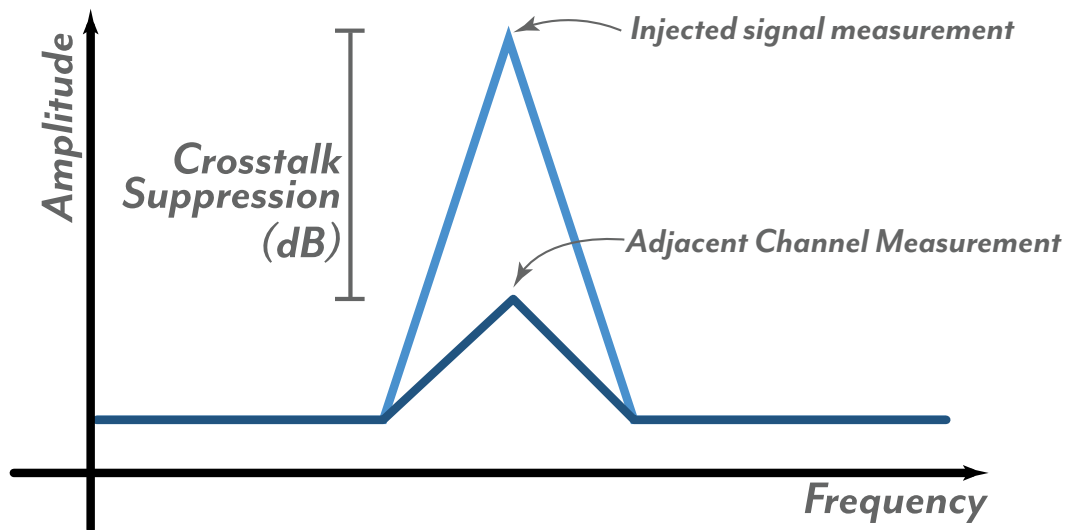


Figure 5.1: The cross-talk suppression for a readout channel is characterised as the difference in the frequency domain amplitude between the injected signal and the measured response in an adjacent channel of interest.

In digital interferometry, the suppression of external signals is dependent on the length of the PRN sequence used and the heterodyne and PRN chip frequencies [1]. In this chapter we go through the process of quantifying the cross-talk between readout channels for the multiplexed acoustic sensing system and discuss the causes of the residual coupling.

5.1 Three Channel Crosstalk

The cross-talk for the acoustic sensing setup was characterised by injecting single frequency sinusoidal tones through the three separate piezo inputs. We compare the amplitude spectral density of each channel, and quantify the suppression of all other channels relative to signal of interest. The amplitude spectral densities for all channels are listed in Table 5.1 and shown in Figure 5.2. In Figure 5.2, we zoom in around the frequency of the injected tone used to interrogate each reflector. Measuring the average suppression for each channel, we see 31 ± 4 dB of suppression of piezo 1, 34 ± 2 dB on piezo 2 and 32 ± 1 dB on piezo 3.

Measurement \ Injection	Piezo 1	Piezo 2	Piezo 3
Collimator	-35.15	-36.59	-33.07
Piezo 1	-	-33.06	-30.60
Piezo 2	-31.29	-	-31.71
Piezo 3	-27.25	-33.27	-
Mean	-31.23	-34.30	-31.71
σ	3.94	1.98	1.26

Table 5.1: Cross-talk values for all combinations of injection and readout channels measured from Figure 5.2. We take the mean suppression across all adjacent readout channels with uncertainty defined by the standard deviation

5.2 Source of Cross-Coupling

Having measured and quantified the cross-talk present in the system, we can go through and identify the contributing sources. In this section we discuss both the limitations and finite suppression afforded by PRN modulation and also effects from mechanically cross-coupling between the piezo driven mirrors.

5.2.1 PRN Correlation Limits

In determining the theoretical maximum possible suppression, we have to initially consider the properties of the PRN sequence used in the system. For a given bit depth, the PRN sequence has an auto-correlation peak given by the code length, $L_{\text{code}} = 2^N - 1$. This is assuming optimal averaging over the entire code, as discussed in Section 3.3. However, in the context of digital interferometry, the value of each chip of the code is weighted by the time varying amplitude of the heterodyne beat. Recalling from Section 3.4, the encoded signal entering the demodulation chain is given by the normalised function $s(t)$:

$$s(t) = p(t - \tau_i) \cos(\omega_H t + \Delta\phi(t))$$

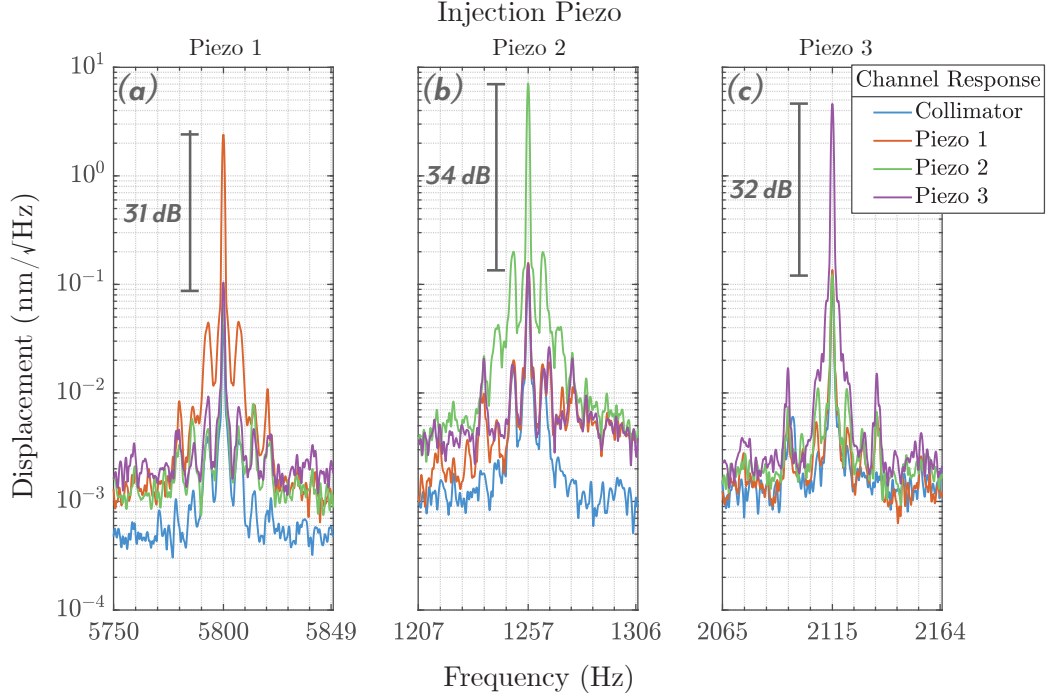


Figure 5.2: The amplitude spectral density of three injected sinusoidal tones into the system. The three subplots, (a) shows the coupling from piezo 1, (b) from piezo 2 and (c) from piezo 3 into the other channels. By comparing the signal amplitude between the injection channel and background channels, the crosstalk was quantified. The measured crosstalk is comparable with the expected cross-talk suppression from digital interferometry

Where τ_i is the encoded delay, ω_H the heterodyne frequency, and $\Delta\phi(t)$ the time varying phase signal. Going through the demodulation process, we multiply by the demodulation code and integrate over the entire code period t_{code} :

$$s(t) = \int_0^{t_{\text{code}}} p(t - \tau_D) p(t - \tau_i) \underbrace{\cos(\omega_H t + \Delta\phi(t))}_{\text{weighting function}}$$

In the case where the heterodyne frequency is equal to, or an integer multiple of the chip frequency, this results in an equal weighting across all the chips. Therefore, this condition gives a maximum theoretical suppression of L_{code} [4]. However, when the heterodyne and chip frequencies are not coherently matched, which is the case for this system, it results in a variable weighting of each of the chip, as illustrated in Figure 5.3.

The variable weighting due to an uncorrelated heterodyne frequency leads to a modified auto-correlation maximum [1]. The modified autocorrelation, converted to dB, can be approximated through Equation 5.1 for equal magnitude reflections:

$$\text{Suppression} = -20 \log_{10} \left(\frac{\pi}{2} \sqrt{\frac{A_i L_{\text{code}}}{A_j}} \right) \quad (5.1)$$

In Equation 5.1, L_{code} corresponds with the length of the PRN sequence used, and A_i for the amplitude of the signal of interest and A_j the amplitude of the unwanted field. For

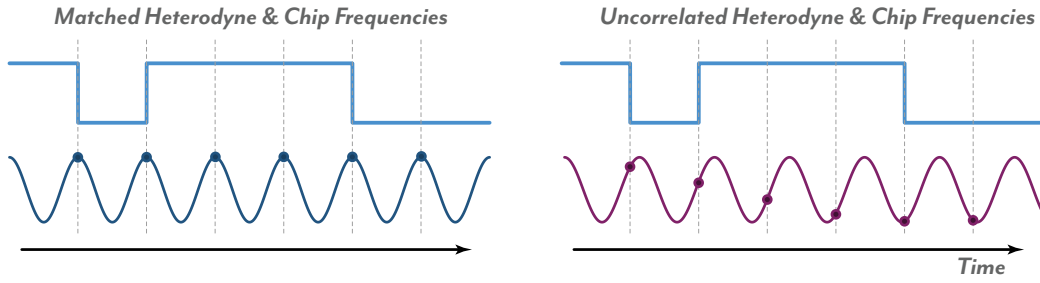


Figure 5.3: When the PRN chip frequency and heterodyne frequency are coherently locked, there is an integer number of cycles per chip. This ensures a constant average across all chips, and optimal correlation can be achieved. When the two frequencies are uncorrelated, the average across an individual chip is variable, leading to a modified auto-correlation maximum when integrated over an entire code length

the measurement presented in the previous section, a 2047 element code was used, and the magnitude of each reflection was adjusted to be approximately equal. If we assume equal reflected power from each of the four surfaces, the expression reduces to the following:

$$\text{Suppression} = -20 \log_{10} \left(\frac{\pi \sqrt{L_{\text{code}}}}{2} \right) \quad (5.2)$$

Substituting in the value for L_{code} we derive a maximum theoretical suppression for the previous measurement of 37 ± 1 dB given a 10% uncertainty in the amplitude of both the signal of interest and unwanted signal.

5.2.2 Mechanical Coupling

Aside from the residual optical coupling through the digital interferometry readout, the other dominant source of coupling arises from directly mechanical coupling between vibrating mirrors. To reduce the impact of this effect, we mounted two partially reflective piezo mirrors on individual isolated breadboards. The remaining coupling was characterised by driving one of the piezo mirrors with an intermediate beam block to prevent it interacting with the interferometer, as shown in Figure 5.4.

While blocking the optical field from interacting with the driven mirror, we measure the response of the system at the drive frequency. As there is no optical interaction, the residual coupling can be attributed solely to mechanically coupling between the driven mirror and other reflectors in the system. Repeating the measurement, we optically measure the magnitude of the driven mirror displacement, measuring the residual coupling as the ratio between the measured response on the drive channel and all other channels. The amplitude spectral density, calibrated to displacement is shown in Figure 5.5.

From Figure 5.5 we see -32 dB of direct mechanical coupling from piezo 3 into piezo 1 and 2 in this optical configuration. We also see mechanical coupling in the collimator measurement, however at a significantly reduced level compared with Figure 5.2. From these two observations we can infer that the mechanical coupling into Piezo 1 and Piezo 2 is of the same magnitude as the residual cross-talk from DEHeI.

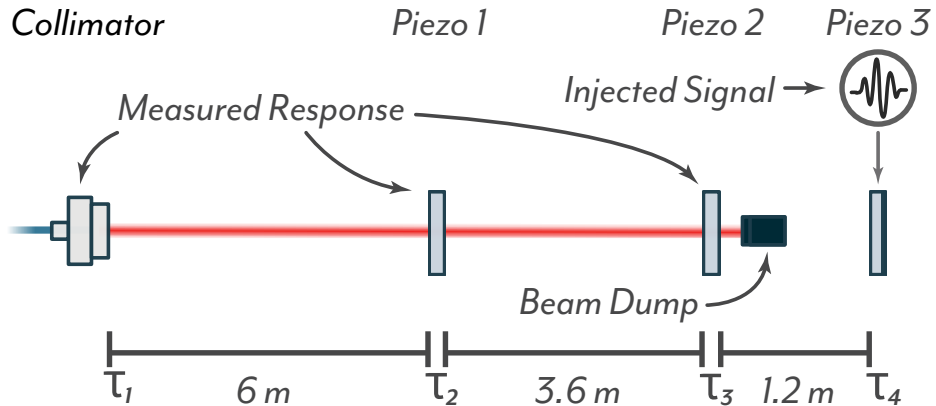


Figure 5.4: A modified signal arm to test mechanical coupling. A beam dump was used to block the final piezo mirror, which was actuating at 800 Hz. The response was measured in the remaining optically active channels. The residual coupling is therefore solely due to mechanical coupling through the optical table. In this setup, piezo 1 & 2 were mechanically isolated relative to piezo 3.

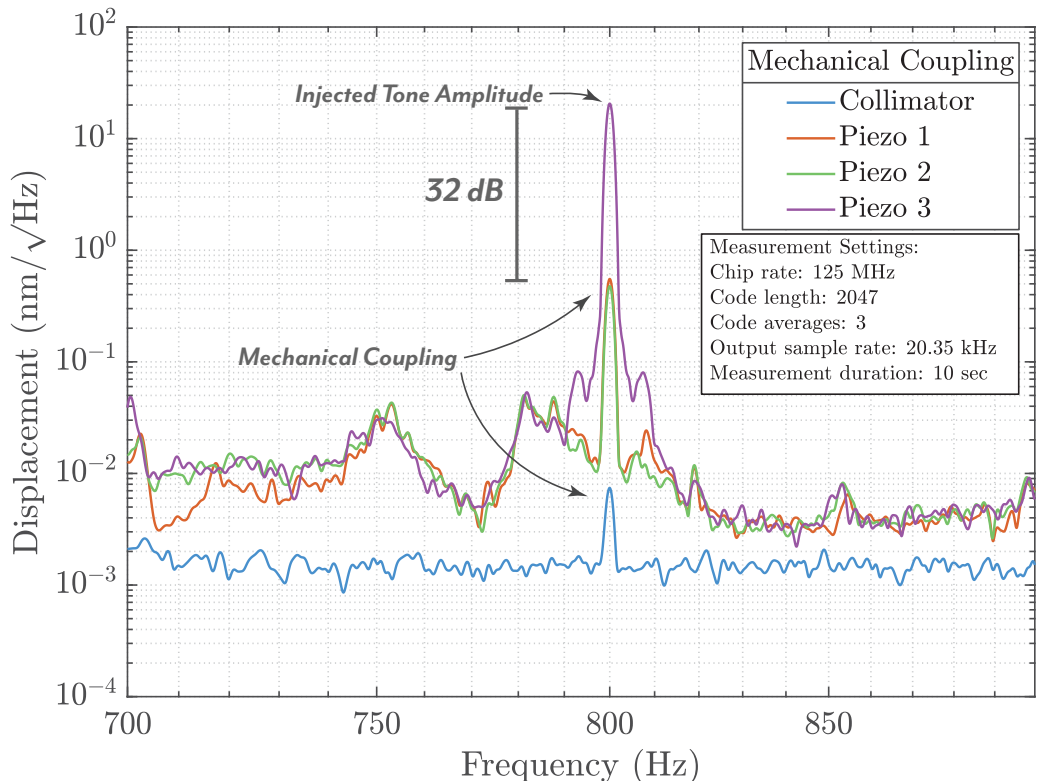


Figure 5.5: The mechanical coupling from piezo 3 into the other reflections. We measure 32 dB of cross-talk suppression, even without an optical path to the actuating piezo. The likely cause of mechanical coupling into the mechanically isolated surfaces is through the steering mirrors used to fold the optical beam.

As these two surfaces were mounted on mechanically isolated breadboards, the mechanical coupling is likely due to the steering mirrors used to fold the beam across the optical table. This in agreement with the measured cross-talk from piezo 3 into those two channels.

5.2.3 Spatial Resolution Limits

A second cause of cross-talk is due to the finite spatial resolution afforded by digital interferometry, and the delay resolution of the demodulation codes. The spatial resolution of a digital interferometry system is determined by the chip frequency of the PRN modulation, and thereby the physical distance that a chip occupies in space. The expression for the chip length for the acoustic sensing setup is given by:

$$L_{\text{chip}} = \frac{c}{2nf_{\text{chip}}}$$

Where c is the speed of light, n the refractive index of the medium and f_{chip} the chip frequency. The factor of 2 arises from the fact the measurement is a reflection measurement, and thus, the distance the optical field travels is twice the physical distance of the interferometer. Therefore, if the relative delay between the two are matched to within a chip, there is at minimum, a partial correlation between the received and demodulation codes, as illustrated in Figure 5.6.

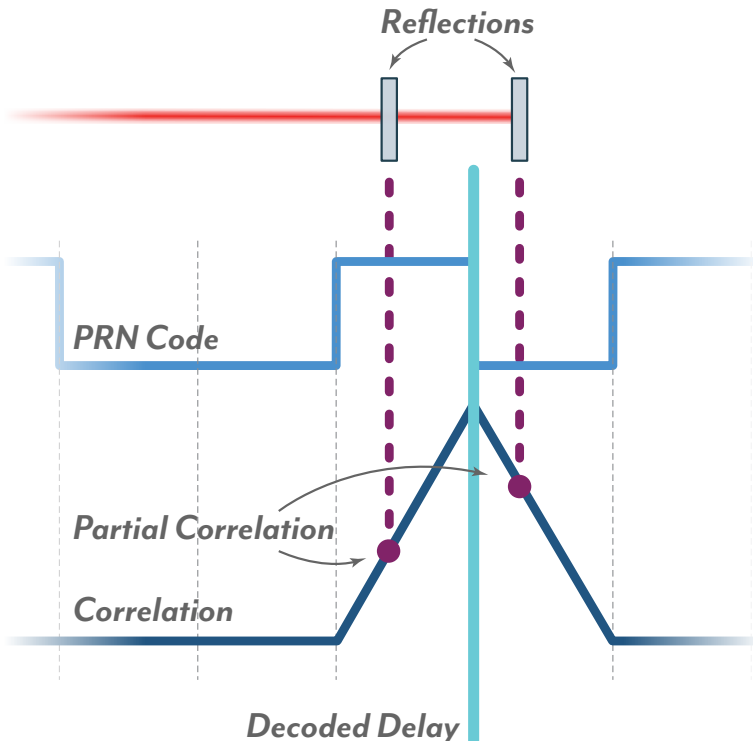


Figure 5.6: Due to the finite chip length of the PRN modulation, the two reflections both receive partial correlations when decoded at the nearest delay. Decoding at the two delays either side will reduce the direct coupling, however, due to the phase of the code symbols relative to the reflector positions, the peak correlation still can not be achieved.

This has two ramifications for the acoustic sensing system. Firstly, if there are multiple reflections or signal sources within a chip length of the desired signal, there is significantly reduced signal rejection provided by using the code. Secondly, if the position of the desired signal within the chip is not centred, the correlation, and therefore subsequent demodulated output will have a lower signal-to-noise.

The resolution problem has several potential solutions, and we discuss three avenues to address the issue here. Firstly, we can use a brute force method and increase the resolution by increasing the chip frequency. This in turn decreases the chip length, as illustrated in Figure 5.7(a) allowing for higher spatial resolution to be achieved. The maximum attainable chip frequency is primarily limited by hardware speed constraints imposed by the sampling speed of the digitisation electronics. This is the case for the current acoustic sensing demonstration. With specialised digitisation electronics, the chip length can be feasibly reduced to on the order of 10cm [56].

The second solution is a variation on the first, still requiring the sampling speed of the digitisation to be increased. However instead of increasing the chip frequency, we can use oversampling of the code to increase the number of samples per chip. This enables tuning of the demodulation code delay by sub-chip resolution, allowing us to tune to the maximum correlation peak, shown in Figure 5.7(b). The difference (a) and (b) is that (b) maintains the same chip length, and therefore the spatial resolution remains the same. Method (b) however is preferred as the higher sampling speed allows for a better defined code shape, with lower Gibbs phenomena, and cleaner spectral output[57]. Work has also been done investigating the use of Delay Locked Loops (DLL) to use the sub-chip resolution to continuously track and lock to the correlation peak[7].

The third method, (c) draws on concepts from other ranging techniques such as frequency modulation continuous wave LIDAR (FMCW LIDAR)[58]. These techniques use a frequency sweep which is common to both the local oscillator and signal fields. The time delay between the two fields results in a frequency shift between the two fields, the magnitude of which carries sub-chip ranging information, shown in Figure 5.7(c). The frequency of this peak can be tracked using a phase locked loop (PLL), which will allow for sub-chip resolution. By band-pass filtering around the peak, we can also reject signals outside this frequency band, thereby improving the overall spatial resolution of the system. In essence, this method uses PRN ranging for the coarse distance measurement, resolving up to the chip length, followed by a higher resolution FM readout for sub-chip resolution[59]. When combined in this way, we can overcome the range diversity limitation of the FMCW technique, and improve the range resolution of the digital interferometry technique with each technique covering the shortcomings of the other.

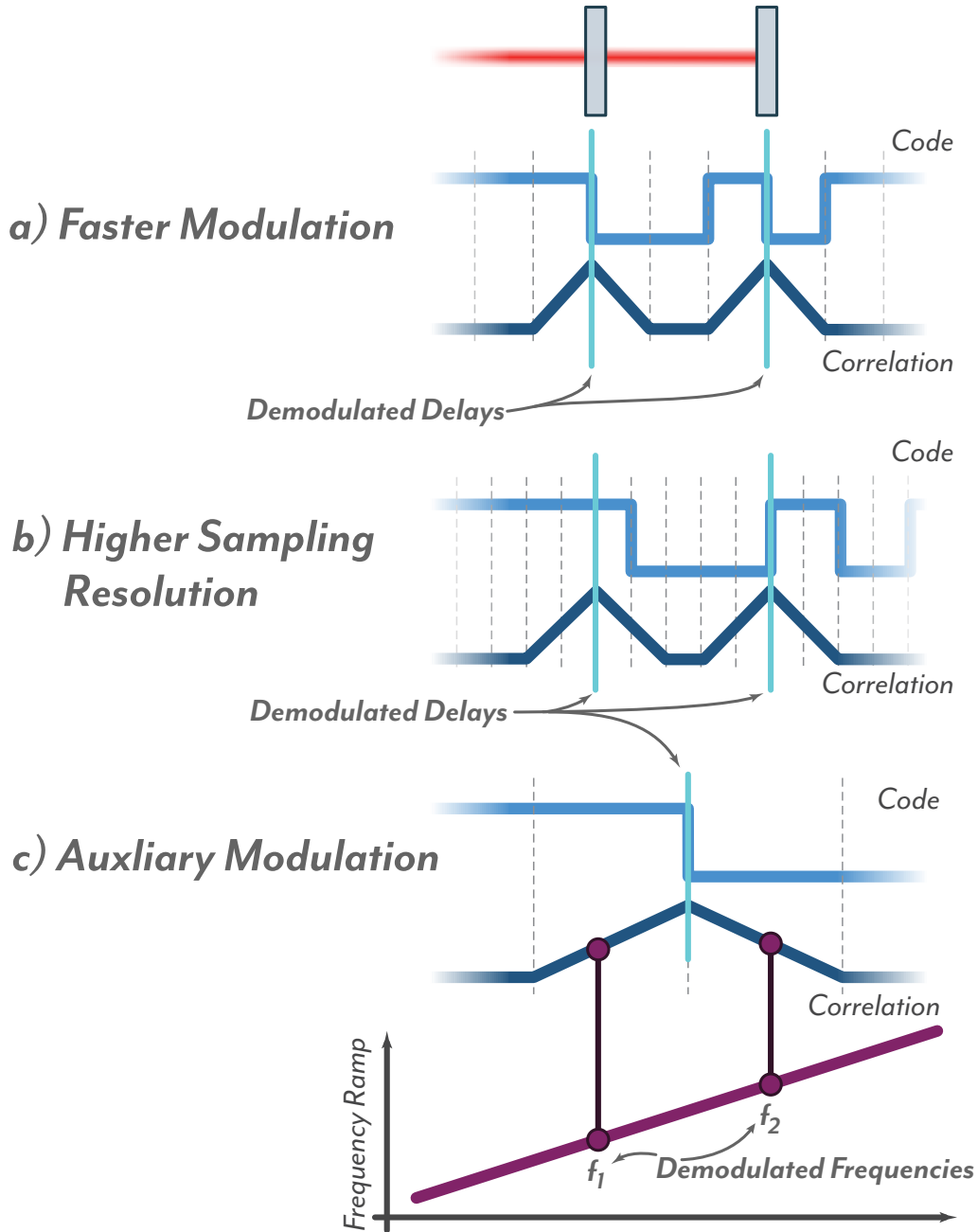


Figure 5.7: Three methods for increasing the spatial resolution of a digital interferometric readout. a) Increasing the chip frequency reduces the chip length and therefore improves spatial resolution. b) Increasing the sampling rate allows for sub-chip demodulation phases to be used, moving the correlation peak to optimise signal to noise for each reflection. c) Adding an additional modulation technique, such as a frequency sweep for sub-chip ranging relaxes the requirements on both techniques and improves resolution.

5.2.4 Multi-Pass Reflections

In addition to the spatial resolution limit of digital interferometry, we must also consider the presence of multiple equivalent optical paths. As digital interferometry applies a time-of-flight gating, the readout for different optical paths with the same time-of-flight or optical path length is degenerate and can not be uniquely identified. As a result, all these fields will contribute and interfere within the demodulated output.

This effect is a larger concern when we have multiple reflective surfaces between which etalons can form. In the example illustrated in Figure 5.8, the three in-line reflections are placed equidistant from each other. In the case where a three bounce etalon forms between the first two surfaces, the path length can be identical to the single pass round trip to the final surface. Therefore, demodulating for the final surface round trip time will also fully couple in the triple pass round trip of the front surface.

We experimentally show this by altering the signal arm to have an equidistant spacing, as shown in Figure 5.8, repeating the cross-talk measurement from before. The spacing between the reflections was set to 3 chips, or 3.6 m. Measuring the cross-talk between each of the channel combinations, we see that there is a large degradation in the cross-talk suppression between the first two mirrors and the last. This accounts for the triple pass and compound round trips between both the first two surfaces and the second two surfaces, as indicated in Figure 5.8.

Injection Measurement		Piezo 1	Piezo 2	Piezo 3
Collimator	-44.62	-52.51	-36.58	
Piezo 1	-	-49.27	-43.84	
Piezo 2	-6.90	-	-36.29	
Piezo 3	-5.68	-13.73	-	

Table 5.2: Cross-talk values for all combinations of injection and readout channels measured from Figure 5.9. Significantly higher cross-talk is present from Piezo 1 and 2 into Piezo 2 and 3 respectively due to multi-pass effects. The higher suppression in other channels are due to the non-equal power ratios between signals in this optical configuration.

In this chapter we have considered the major contributing sources of cross-talk in a digital interferometric system and characterised them through in the context of the multiplexed acoustic sensing architecture. Additional techniques for the improvement of cross-talk, beyond the PRN suppression limit, have been explored on this architecture by Ya Zhang and are detailed in her thesis on the topic[47].

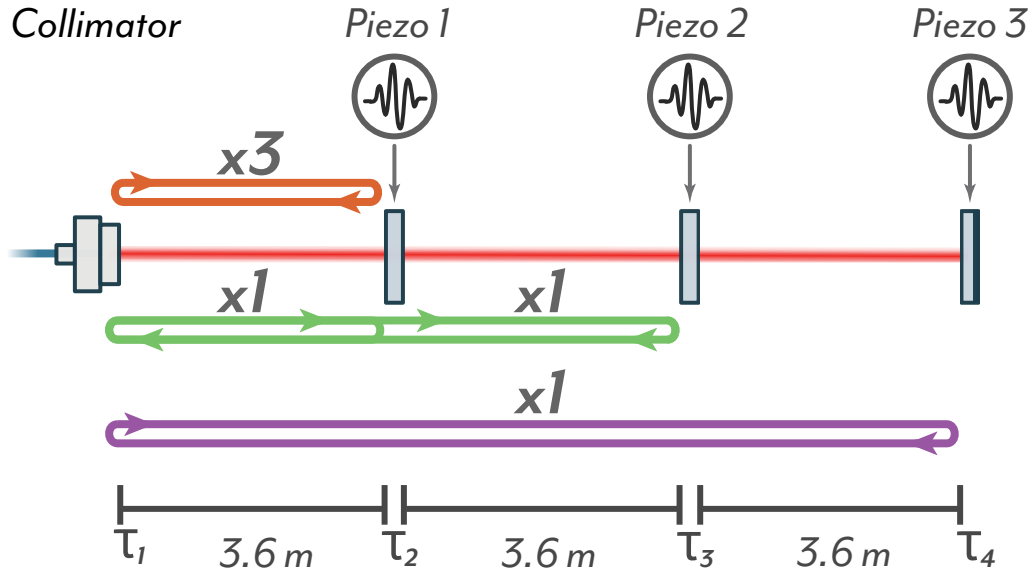


Figure 5.8: The signal arm of the interferometer was modified to be equidistant with a spacing of 3.6m between each surface. This results in several equidistant path combinations. The highlighted example is the equivalence between the triple pass of the first two reflections, single pass of surface 1 - 2 and 1 - 3, all having an equivalent time-of-flight to the round trip to the final surface.

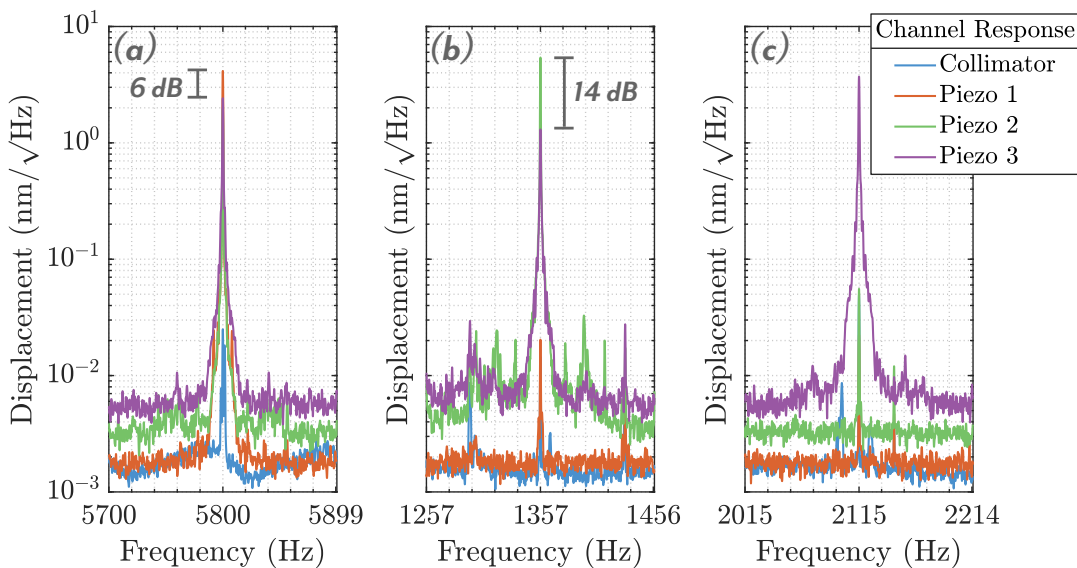


Figure 5.9: The amplitude spectral density of three injected sinusoidal tones into the system with equidistant surface spacing. The three subplots, (a) shows the coupling from piezo 1, (b) from piezo 2 and (c) from piezo 3 into the other channels. There is significantly higher coupling in a) and b) due to the presence of etalons with an optical path length equivalent to the distance to piezo 3.

Multipoint Acoustic Sensing Conclusions

In this work we have demonstrated a multiplexed interferometric readout of four measurement channels, characterising the isolation of three audio band signals using digitally enhanced heterodyne interferometry. In this experiment we also highlight a number of technical challenges that need to be considered when applying digital interferometric techniques to vibration or acoustic sensing.

The main experiment, as described in Chapter 4, demonstrates the initial audio band dynamic displacement measurements from three in-line reflections. In order to achieve a benchtop scale experiment, the spatial resolution of the digital interferometric gating was confined to the order of the table length, which was achieved through the high speed, 125 MHz chip frequency. Due to the tunability limitations of acousto-optic frequency shifters, the difference between the high speed chip frequency and the factor of three slower heterodyne frequency, the aliasing of spurious harmonics from the pseudo random modulation was present in the measurement band. Although the cause of the harmonics was identified as a function of the digital interferometric readout, the spectral position of the harmonics can only be shifted, and not readily removed or suppressed.

The chapter also details the measurement of the transfer functions of the system. The white noise measurement using an acousto-optic modulator for signal injection demonstrated a flat readout transfer function over the measurement bandwidth. Following this, the piezo mirror transfer functions were characterised by further white noise injection measurements. From these measurements we determined that the system response within the measurement band is dominated by the transducer response.

The displacement sensitivity was characterised with 1 minute measurements of all measurement channels without any injected signals. Taking the amplitude spectral density of the time series measurement, we see a noise floor dominated at low frequencies by laser frequency noise from the free-running laser. The audio band is dominated by ambient laboratory acoustic noise reaching a displacement sensitivity of $1 \text{ pm}/\sqrt{\text{Hz}}$ at 1 kHz.

We then proceed to characterise the cross-talk suppression afforded by the digital interferometric readout. In Chapter 5 we measure the cross-talk using a three signal measurement. Aside from the mechanical coupling present on piezo 3, the measured cross-talk is several dB greater than the predicted limit, based on initial estimates by

Shaddock [1]. The limitations of this method lie in the approximation of the weighting of the PRN modulation due to uncorrelated chip and heterodyne frequencies. Recent work by Sibley et al aims to provide a more rigorous analysis of this specific cross-talk coupling case, and these results will be revisited in conjunction with insights from that new work.

Chapter 5 further characterises the spatial resolution limit and poses several methods to improve the spatial resolutions through changes to the hardware configuration. The final experiment examines the effect of cross coupling due to multiple equivalent optical path lengths into the measurement. This provides a critical design consideration for future digitally multiplexed sensors.

6.1 Key Specifications

Here we list the main technical specifications of the multi-point acoustic sensing array to act as a reference point for future designs. For the key specifications, we refer back to those defined in the design chapter, Chapter 4.

Readout Bandwidth	The readout bandwidth had a Nyquist frequency of 10.2 kHz
Spatial Resolution	Limited by the chip frequency of 125 MHz, the spatial resolution was 1.2 m and was experimentally verified.
Ambiguity Range	The ambiguity range for an 11 bit code at 125 MHz chip frequency is 4.9 km
Displacement Sensitivity	Measured displacement noise floor of $1 \text{ pm}/\sqrt{\text{Hz}}$ at 1 kHz reducing to $10 \text{ pm}/\sqrt{\text{Hz}}$ at 10 Hz as measured from the collimator.
Cross-talk Suppression	We achieve an average cross-talk suppression of $32 \pm 2 \text{ dB}$ across the three channels

6.2 Future Work

The development of a robust multiplexing architecture functioning in the audio band opens up applications on a number of different fronts. Firstly, this architecture provides an optically simple and scalable method for testing the properties of pseudo random modulation. In the future, this work will directly link with other efforts by Sibley et al in order to construct a complete description the Digital interferometric readout and its capabilities [60]. In this area, the main of interest is in characterising the causes behind cross-talk coupling, and whether additional measures may be able to mitigate it.

One regime where this becomes critical is where a spurious interference from elsewhere in a system are dominant. Although suppressed through the demodulation process, instances where weaker fields are still obscured due the demodulation noise floor may arise. One example where this is prevalent is free-space laser communications where at a transceiver a received signal is likely to be significantly smaller than the transceiver's

own output. To this end, follow-on work has been done led by Ya Zhang to mitigate phase noise coupling from high strength reflections by introducing a phase ramp. This phase ramp upshifts the demodulated code noise from the strong field to discrete harmonics located at multiples of the ramp frequency. These harmonics can be tuned out of the measurement band of interest, further suppressing the unwanted field from the measurement. Initial demonstrations as detailed in her thesis shows an additional 15 dB suppression of spurious interference on top of the digital interferometric readout [47].

An integral part of the digital interferometric readout, its noise performance and cross-talk suppression is the preservation of the PRN code modulation shape. As modulation speeds are increased, and become bandwidth limited by the electronics or electro-optic components, the higher order harmonic content of the code is filtered, degrading the code shape. There have been several instances outside of digital interferometry where high speed PRN modulation has hit this technical limit[42]. While for this demonstration, the spatial resolution was limited to 1.2 m by the maximum achievable chip frequency of the digital signal processing. Increasing the speed of the digital signal processing is primarily an engineering challenge, which is readily solvable using current telecommunications hardware. As we move towards this regime, more consideration would have to be given to code shape and possible modulation errors arising from missing or filtered spectral content. Since the conclusion of this experiment, an analysis of these effects in the context of a digital interferometric readout is being investigated by Sibley et al [60].

More broadly, the application of this work can be extended to a variety of different areas. One such example is a passive quasi-distributed fibre hydrophone array aimed towards oceanographic survey and naval surveillance. To date, these types of fibre optic arrays have two methods for interrogation - active and passive. Active arrays are the current prevailing method, where each individual transducer is actively lasing, driven by a remote pump field while passive sensors use a remotely injected sensing field to interrogate the transducer directly [21, 31]. However, for both these methods, the multiplexing architecture utilised is a wavelength division multiplexing (WDM) topology. The techniques shown here using digital interferometry can readily be adapted to a passively interrogated array, removing the need for separate wavelengths, wavelength filters, or detectors. In this way, the scalability of the hydrophone arrays can be improved significantly.

Another key area where Digital interferometric multiplexing can be applied is for airborne pollution monitoring. Particulates in the atmosphere due to industrial pollution provide a distributed scattering field when interrogated with an optical beam. Digital interferometry provides a new method to gate these signals, providing depth information on a particulate cloud as well as absolute ranging information. While possible to develop these systems with either a pulsed or swept frequency approach[26, 61], the use of a single frequency source, or optical frequency comb opens up the possibility to combine digital interferometry with a spectroscopic readout, enabling identification of the particulate chemical composition and concentration.

In this work, we demonstrate how interferometric systems may be simplified using digitally enhanced heterodyne interferometry. As we have discussed in this chapter, the next major innovations lie in combining digital interferometry with other readout quadratures to develop new optically simple and robust sensors.

Part II

Digitally Enhanced Fibre Frequency Reference

Stabilising Optical Sources

The stabilisation of oscillators is an established and mature field, both in the radio-frequency (RF) and optical domains. The stability of an optical source is determined by its phase noise: the phase fluctuations of an oscillator with time. When differentiated, this in turn leads to frequency fluctuations in the source. The natural stability of an optical source depends on many factors: the type of light source and its mode of generation, the thermal stability of the environment, and vibrational coupling to name a few.

In order to stabilise an oscillator, a frequency reference or standard is required. A frequency reference is a measurement tool which characterises the phase and frequency fluctuations of another oscillator relative to itself. References therefore must have a response dependent on the oscillator frequency, examples in the optical domain include the resonance of an optical cavity, absorption spectra of a molecule, fringes of an interferometer or interference with another optical source [62]. As references have a frequency dependent response, they also have a natural stability, driven by similar environmental factors to the optical source under test. Provided the reference stability exceeds the source under test, the relative phase can be used as a control signal; a means to correct these fluctuations. In this way, the stability of a frequency reference may be transferred to other oscillators.

The development of optical stabilisation techniques and frequency references is critical for the improvement of optical metrology systems, in particular those using an interferometric or phase sensitive readout. As high precision optical metrology continues to develop, through applications such as gravitational wave detection, the ability to stabilise optical sources continues to improve. As the application of optical metrology expands outside the confines of the laboratory to harsher environments, the development of robust, field deployable, and space qualified frequency references becomes of interest.

In this work, we continue the development of the fibre optic frequency reference, initially demonstrated at the National Measurement Institute. We consider the viability of an 'In-Line' reference design, discussing the technical limits imposed by Rayleigh scattering. We further move to calibrate the reference using an independent frequency measurement using an optical frequency comb which in turn provides an estimate of the thermal limits of the architecture.

7.1 Quantifying Optical Stability

There are a number of different methods for quantifying the stability of an optical source. The most readily used method is linewidth determination, where the frequency noise of an oscillator is integrated over a finite measurement time. While this metric provides a single value for stability, insight into the optimal integration time, spectral shape and frequency distribution of the contributing noise sources can all be determined using more comprehensive methods. Of these methods, the ones we discuss here are the Allan variance and deviation and the frequency spectral density.

In order to quantify the stability of an optical source, we must firstly consider the dynamics of the noise processes which limit its stability. For optical sources, and oscillators in general, these noise processes can be categorised in terms of their frequency dependence. As a result, each noise source will manifest itself in measurements uniquely and, with the appropriate methods, can be identified and quantified [63, 64]. A table of the different driving noise sources and their respective coupling in an Allan deviation and frequency spectral density are shown in Table 7.1.

Noise Process	Allan deviation slope	FSD slope
White Phase	τ^{-1}	f^2
Flicker Phase	τ^{-1}	f
White Frequency	$\tau^{-1/2}$	1
Flicker Frequency	τ^0	f^{-1}
Random-walk Frequency	$\tau^{1/2}$	f^{-2}

Table 7.1: Frequency dependence of noise processes when measuring through an Allan deviation and frequency spectral density (FSD)

In the following sections, we briefly discuss both Allan variance and spectral density approaches to characterise the stability of an optical source.

7.1.1 Allan Variance

As the linewidth of an optical source determined by its integration time, the Allan variance extends on this concept and provides a measure of stability as a function of the integration time. Named after its inventor David Allan, the Allan Variance, and its square root, the Allan deviation were developed to provide a measurement tool to characterise the frequency stability of oscillators due to different noise processes [63, 65]. As such, using an Allan variance, the dynamics of these noise processes, and their relative contributions to the total stability of an oscillator can be determined.

The Allan variance and deviation therefore become an important characterisation tool for oscillator and clock stability. Its usage however extends further as a tool for characterising the optimal integration times for metrological systems. This has seen the Allan deviation become a widely used metric in fields such as inertial navigation and spectroscopy, where the optimal integration times for gyroscopes and spectrometers determine both the long term stability and measurement acquisition speeds of these systems.

The Allan variance, and deviation are calculated through a time series measurement, averaged over a variable time, τ . By varying the integration time τ , we can determine the variance of a signal as a function of this integration time. Mathematically, we can compute the Allan variance for a time signal, $y(t)$, as follows:

$$\sigma_y^2(\tau) = \int_0^\infty \frac{1}{2} [\bar{y}(t + \tau) - \bar{y}(t)]^2 dt$$

Where $\bar{y}(t + \tau)$ represents the time average over an integration time, τ . When computing the stability of clocks, oscillators and optical sources, the input to the Allan variance calculation is nominally fractional frequency. This can be computed as the ratio of the frequency noise to the carrier frequency. Lastly, while we define the Allan variance, in practice we compute and compare the Allan deviation for determining oscillator stability. In a similar vein to variance and standard deviation, the Allan deviation is computed as follows:

$$\sigma_y(\tau) = \sqrt{\sigma_y^2(\tau)}$$

In the work we present in this thesis, the Allan deviation is computed from fraction frequency noise data using the industry standard program Stable32 developed by W.J. Riley [66], and is replotted in MATLAB for visual consistency.

7.1.2 Spectral Densities

Whereas the Allan variance is a time domain measure of stability, the spectral density acts as a frequency domain counterpart, depicting the phase noise of a source as a function of its Fourier frequency. Further, the spectral density calibrates to the measurement sample time, referred to as the resolution bandwidth in the frequency domain. For example, if we consider the power spectral density (PSD), $S(f)$, it provides a measure of the *noise power per unit frequency* as a function of frequency. For metrology we use the amplitude spectral density (ASD)¹, $\tilde{S}(f)$, which follows the same square root dependence with the PSD.

Since it accounts for the resolution bandwidth of a discrete frequency domain measurement, the spectral density is often used to analyse the frequency contributions of different noise sources. The main applications where spectral densities are employed include the communications sector, where the frequency domain analysis of spread-spectrum signals is critical and the metrology sector, where the noise performance of sensors is characterised in the frequency domain. When specifically relating to the stability of optical sources, the main metric we use is the frequency spectral density, $\tilde{S}_\nu(f)$ [64].

Throughout this thesis, there are instances of calibrated spectral densities, where the function has been calibrated to reflect an appropriate measurand for the given application or system. As we are dealing with measurements of optical phase, we measure the phase spectral density of our interferometer, $\tilde{S}_\phi(f)$. In the work specifically pertaining to the fibre frequency reference, we use the interferometer response to calibrate to a frequency spectral density, $\tilde{S}_\nu(f)$, as discussed in Chapter 9.

¹The amplitude spectral density may also be referred to as the root power spectral density (RPSD)

In the most general case, we relate the spectral density to the total variance of a measurement by integrating over all frequencies[63]:

$$\text{Total Variance} = \int_0^{\infty} S(f) df$$

However, the actual computation and methods of spectral density estimation is a broad field, and is not discussed within the scope of this thesis. In order to compute the spectral density of discrete time series data, we employ the Welch method for spectral density estimation. This relies on overlapping windowing of a time series to compute and average subsets of a time-series data set. The windowing method we use in this thesis is the Blackman-Harris window for its high side-lobe suppression characteristics [67].

7.2 Measuring Frequency: References and Standards

The measurement of optical source stability requires a reference point: a frequency reference with which to compare against. Using a reference, the relative frequency with a test optical source can be measured. Once measured, stabilisation is possible with real-time feedback or through post-processing feed-forward architectures. A subset of frequency references are frequency standards, which differ as they have a fixed, known frequency. This allows them to act as a reference point for absolute frequency, as opposed to being solely a relative measure.

We can break down the types of optical frequency reference into three broad categories: optical absorption transitions, optical frequency combs referenced to atomic clocks and interferometers. Each category of frequency reference provides optimal stability in a unique frequency band, as shown in Figure 7.1, and when used together may be used to address both short time-scale frequency fluctuations and long term frequency drift.

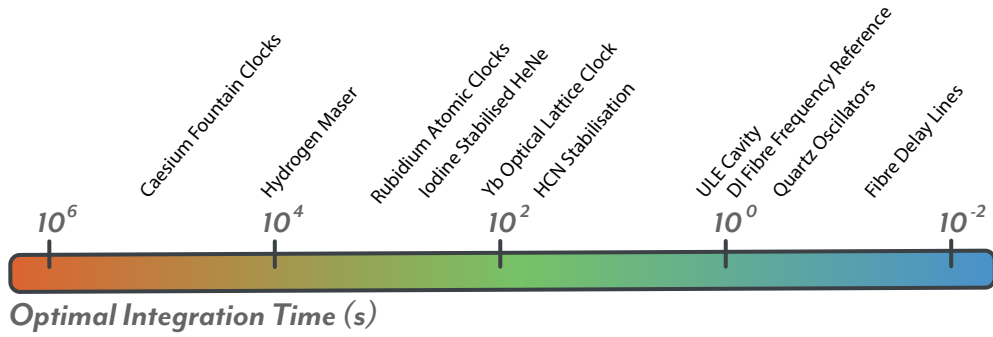


Figure 7.1: The optimal frequency regime of different frequency reference architectures. While atomic standards are able to provide long term stability on the order of hours to days, this is often limited by the duty cycle of the measurement at high frequencies. Meanwhile, short term stability is typically achieved through optical references such as ULE cavities which suffer from mechanical and thermal drifts at longer integration times. In order to achieve broadband frequency stability, a hybrid approach consisting of combination of references spanning a broad range of Fourier frequencies is required.

Spectroscopic References

Laser stabilisation and laser absorption spectroscopy are closely linked fields of research with both areas being of benefit to the other. In the case of spectroscopy, the use of narrow linewidth optical sources offers better spectral resolution, resolving spectral features with higher fidelity. On the flip-side, atomic and molecular transitions also represent stable, well known reference points for optical frequency, and can therefore act as frequency standards.

The requirements for these transitions include that they are spectral narrow and immune to shifts from external stimulus from electric or magnetic fields. Some examples of transitions include the Iodine transitions probed by HeNe lasers at 632 nm[68, 69]. Caesium hyperfine transitions are also readily optically accessible [70]. At telecommunication wavelengths, HCN and Acetylene are typically used as 1540 - 1560 nm standards [71, 72, 73, 74], with fractional stabilities achieved typically on the order of 10^{-12} [75].

As the spectral width of a transition is paramount for its effectiveness as a frequency reference, methods of minimising the transition linewidth need also be considered. Such methods include the use of spectroscopic techniques such as Saturated Absorption Spectroscopy and Noise Immune Cavity Enhanced Optical Heterodyne Molecular Spectroscopy (NICE OHMS) [76]. Other methods use cryogenics or laser cooling to reduce thermal motion, and thereby reduce doppler effects [70]. While the challenge of doppler broadening may be addressed, the precision afforded by these standards remains limited by the linewidth of the transition.

Atomic Standards & Optical Frequency Combs

A critical development in the area of both spectroscopy and laser stabilisation was the demonstration of a self-referenced optical frequency comb [77, 78]. The initial demonstration showed the phase control of two key parameters, the comb repetition rate and carrier envelope offset frequency, back to an RF frequency standard. This directly enabled the stability of RF sources to be transferred to the optical domain.

The main RF frequency standards used to stabilise optical frequency combs are either Rubidium or Caesium atomic clocks. Being atomic clocks, both of these act as standards, and allow the frequency comb in turn to provide a measure of absolute frequency. The main advantage of these clocks is the stability, which is achieved on time-scales on the order of > 1000 seconds. For example, a Rubidium atomic clock achieves a nominal fractional frequency stability on the order of $\sim 10^{-13}$ at 1000 seconds [79]. This is further improved by transitioning to a Caesium fountain clock, where stabilities of $\sim 10^{-16}$ have been achieved on the order of $\sim 10^6$ s integration times [80].

More recent developments have seen the probing of optical transitions in favour of the traditional RF transitions, leading to the development of ‘optical clocks’. This includes the development of strontium lattice and ytterbium lattice clocks. With these clocks, unprecedented stability has been achieved, with fractional stabilities on the order of 10^{-18} being possible [81]. The transitions probed in optical clocks are spectrally very narrow, and thus frequency pre-stabilisation is required for the lasers used to probe these transitions. As a result, the cost of achieving high fractional stability lies in the associated complexity of the experimental apparatus. Additionally there is an associated preparation time, reducing

the duty cycle of the measurement and limiting the readout bandwidth. For these reasons, optical clocks to date are used as large pieces of infrastructure, to disseminate frequency stability for other experiments.

Interferometers & Resonators

The last category we consider, interferometers, primarily refer to the use of optical resonators but can be extended to include two beam interferometers, such as the unbalanced Michelson or Mach Zehnder topology. Critically, unlike molecular transitions or a self-referenced optical frequency comb, interferometers only provide a measure of relative frequency, and thus cannot be used to determine the absolute frequency of a source.

The response of an interferometer to relative frequency fluctuations is dependent on the optical gain, also known as the optical discriminant can be determined by the arm-length difference. For a Michelson or Mach Zehnder topology, this is determined purely by the difference between the length of the two interferometer arms. In the case of the optical resonator or cavity, the discriminant is directly proportional to the finesse. One of the first implementations of an optical resonator as a frequency reference for an optical source was demonstrated by Hall et al [82] with further implementations by Hänsch et al [83] and Drever et al in the following years [84].

This stability is primarily limited by an interferometer's mechanical and thermal properties, and thus operate most effectively over short time-scales (>1 Hz) where the effects of temperature related drift are reduced [85]. Therefore, in practice interferometers are commonly referenced at low Fourier frequencies to a long time-scale stable source, such as a molecular transition or comb in order to achieve broadband stability.

The most common implementation in of an interferometer reference is the use of a high finesse optical cavity. An optical source is tuned to a cavity resonance, and its frequency with respect to that resonance is measured. There are a number of methodologies for carrying out this measurement, but in essence it can be reduced to measuring the interference between an optical field probing the cavity (on resonance) and one that is promptly reflected (off resonance).

Another contribution by Drever et al, the PDH locking technique achieves this by using phase modulation to produce promptly reflected sideband fields [84, 86]. The interference between the carrier and sidebands then carries the necessary phase information for determining the phase offset between the optical field and cavity resonance. This is conventionally used as an error signal for feedback to the laser frequency, or alternatively for feed-forward; correction through post-processing. Two examples of analogous techniques are the Hänsch-Couillaud method [83] which utilises polarisation, and spatial mode locking [87]. These can be readily translated from optical cavities to other interferometer architectures [55, 88].

For optimal performance, these interferometers are typically environmentally isolated through active temperature control, vacuum operation and mechanical isolation [89]. However, for state-of-the-art performance, the use of Ultra-Low-Expansion (ULE) glass cavities are required [90, 89]. This further reduces the effects of thermal expansion by

operating the cavity in a temperature regime where the material linear thermal expansion coefficient is near zero. With such cavity designs, fractional frequency stabilities on the order of $\sim 10^{-15}$ over 0.1 - 1 second integration times ($\sim 0.1 \text{ Hz}/\sqrt{\text{Hz}}$ at 1 Hz) are readily achievable and commercially available²[91]. Alongside linear expansion, thermo-refractive noise in both the coatings, and the bulk cavity mirrors themselves represent another fundamental limit [92]. Addressing this through cavity design and material choice, approaches using alternative materials such as sapphire [93] and cryogenic silicon cavities have demonstrated, with the best performing setups reaching fractional frequency stabilities of 10^{-16} ($0.04 \text{ Hz}/\sqrt{\text{Hz}}$ at 1 Hz). However, due to the amount of engineering and hardware required to achieve these results, such systems reside in bespoke laboratory setups [90].

Besides optical cavities, the use of fibre-optic interferometers and delay lines is attractive due to the vastly simpler hardware implementation. While we present work on a digitally enhanced fibre frequency reference in this thesis, there have been several other implementations using fibre optic delay lines which reach near the same performance as ULE optical cavities [94, 95]. The key shortcoming of optical fibre based references however is the maximum achievable integration time before the onset of thermally induced drift. Unless isolated with similar levels of care as an optical cavity, existing demonstrations achieve optimal stability well above 1 Hz.

The advantages of a fibre optic frequency reference are its cheap, alignment free, robust construction, making it ideally suited for satellite based metrology and laser communication applications. Initially developed for the Gravity Recovery And Climate Experiment (GRACE), the Digitally Enhanced Fibre Frequency Reference uses digitally enhanced homodyne interferometry to characterise and mitigate the limiting technical noise sources, especially at sub-hertz Fourier frequencies [11, 12, 55, 96]. In this part of the thesis, we extend on this prior work, characterising the coupling of Rayleigh backscattering, and then continue to use an optical frequency comb to characterise the thermal expansion of the frequency reference.

²Depending on the publication, the fractional stability or frequency spectral density are quoted.

Digitally Enhanced Homodyne Interferometry

Digitally Enhanced Homodyne Interferometry (DEHoI) is a natural extension of Digitally Enhanced Heterodyne interferometry as discussed in prior sections of this thesis. By extending to the homodyne case, we remove the requirement for a frequency shifted local oscillator to scan the phase of the signal field. This technique was initially demonstrated by Sutton et al [5], which contains further detailed discussion including effects of modulation errors and subsequent noise coupling. The DEHoI technique has also subsequently been used for initial fibre frequency reference experiments by Ngo et al [11, 12, 96].

The extension to a homodyne readout is achieved through a four level pseudo-random code architecture, which samples the signal phase at four discrete points in IQ space. By removing hardware and shifting to a code based scanning method, the homodyne optical layout is further streamlined compared with an equivalent heterodyne architecture, enabling optically simpler, compact and cheaper systems.

As with digitally enhanced heterodyne interferometry (DEHeI), the homodyne variant also allows for gating of signals based on code time-of-flight. This enables the same suite of improvements afforded by DEHeI including the multiplexed readout from several in-line sensors [4], rejection of spurious electric fields due to scattering [96] and coarse ranging information to be extracted [3]. In this chapter, we discuss the basic principles of digitally enhanced homodyne interferometry including code generation, optical field analysis and demodulation scheme as they pertain to the Fibre Frequency Reference.

8.1 Homodyne Interferometry

Homodyne interferometry can be considered a subset of the heterodyne case with the local oscillator (LO) frequency shift, ω_H being set to zero. Considering a two beam Mach Zehnder interferometer, as shown in Figure 8.1, the resulting power on the photodetector is then dependent solely on the magnitude of the interfering fields and the differential phase between them. Starting from an input field:

$$E_{in} = \tilde{E}(t)e^{i\omega t}$$

where $\tilde{E}(t)$ is the amplitude of the input field and ω , the optical frequency. Propagating through the interferometer similarly to the heterodyne case, we arrive at the following optical field at the photodetector:

$$\begin{aligned} E_{D1}(t) &= E_S(t) + E_R(t) \\ E_{D1}(t) &= ir_2 t_1 \tilde{E}(t) e^{i\omega t + i\phi_S} + ir_1 t_2 \tilde{E}(t) e^{i\omega t + i\phi_R} \end{aligned}$$

Here $E_S(t)$ is the signal electric field and $E_R(t)$, the reference electric field. The beamsplitters have transmission and reflection coefficients of t and r respectively. Over their respective paths, the two fields accumulate a phase ϕ_S for the signal path and ϕ_R for the LO path.

If we assume a 50:50 splitting ratio for both beam-splitters this reduces $r_1 = r_2 = t_1 = t_2 = \frac{1}{\sqrt{2}}$. Given the total field at the detector we can take the modulus square to calculate the incident optical power:

$$P_{D1}(t) = \frac{|\tilde{E}(t)|^2 (1 + \cos(\Delta\phi(t)))}{2} \quad (8.1)$$

Where $\Delta\phi(t)$ is the differential phase between the local oscillator and the signal arms. If we consider the Mach Zehnder interferometer in Figure 8.1, the phase difference is again given by the differential arm length of the interferometer by the following expression:

$$\Delta\phi(t) = \frac{2\pi\Delta L}{\lambda}$$

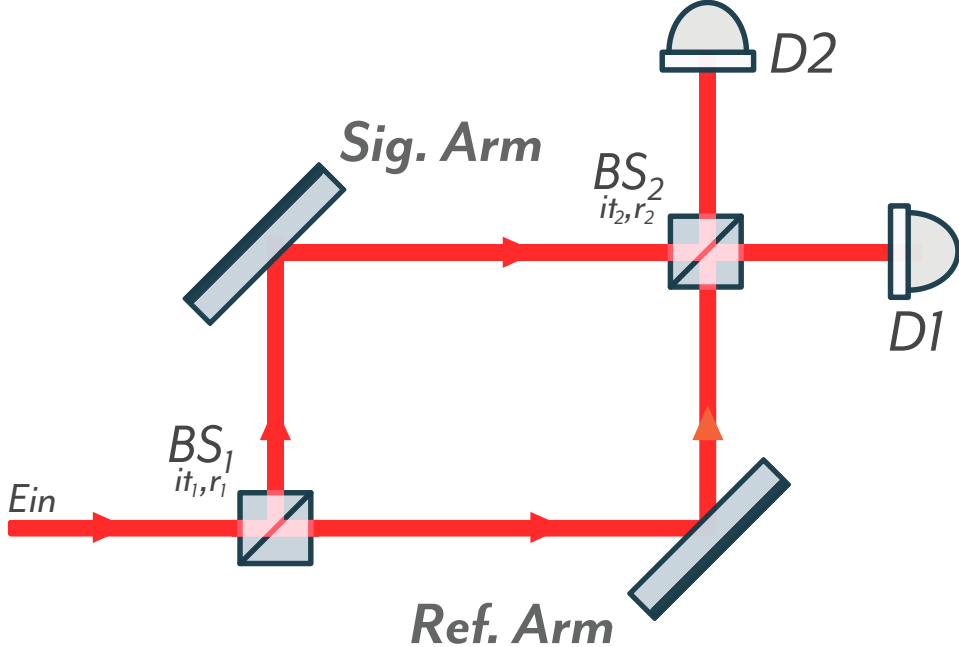


Figure 8.1: A basic 2 beam Mach Zehnder interferometer. The instantaneous optical power at the detectors D1 and D2 are dependent on the phase difference between the two arms. Unlike the heterodyne variant shown previously, the Homodyne interferometer has no frequency shift between the two arms, therefore the interference occurs around DC.

8.2 Quadrature Phase Shift Modulation

Due to the absence of a local oscillator, we require an alternative phase shifting method to extract phase difference. This can be achieved using optical methods such as an 90 degree hybrid, which consists of an interferometer with discrete phase shifts to allow for measurements to be made in each quadrature[97, 98, 99]. In digitally enhanced homodyne interferometry, we take the same concept of discrete phase shifts, and achieve this by using a single four-level, Quadrature Phase Shift Key (QPSK) modulation scheme instead. The QPSK modulation constellation, as shown in Figure 8.2, has each of the four levels separated by a $\pi/2$ phase difference. This discretely maps the signal into each quadrature, which when sampled and combined allows for a complete reconstruction of the modulation constellation, and extraction of the optical phase difference.

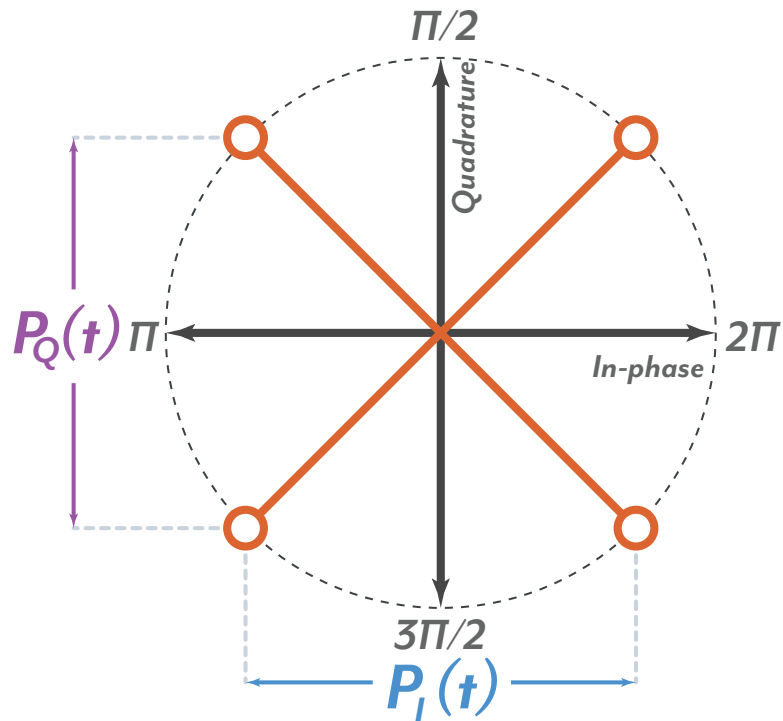


Figure 8.2: The phase constellation for the QPSK modulation implemented in this work. Two m-sequence PRN codes, $P_I(t)$ and $P_Q(t)$ are used to toggle between interrogating the I-I and Q-Q quadratures respectively through a series of logic operations. By deterministically projecting into the four quadratures, we are able to reconstruct the DC phase during the demodulation process without the need for a continuous phase scanning mechanism

As with digitally enhanced heterodyne interferometry, we use the unique auto-correlation properties of m-sequences for the generation of QPSK modulation codes. In doing this, the modulation scheme is able to include the ranging and signal isolation afforded by digital interferometry alongside the 4-level discrete phase scan required for signal extraction. The pseudo-random four-level modulation is achieved by using two binary PRN codes for mapping between $\pm I$ and $\pm Q$ quadratures respectively. The mapping

into the phase constellation in Figure 8.2 can be represented by the following set of logic operations:

$$\begin{aligned} P_I(t) \& P_Q(t) &= \pi/4 \\ \overline{P_I(t)} \& P_Q(t) &= 3\pi/4 \\ \overline{P_I(t)} \& \overline{P_Q(t)} &= -3\pi/4 \\ P_I(t) \& \overline{P_Q(t)} &= -\pi/4 \end{aligned}$$

Where $P_I(t)$ and $P_Q(t)$ are the respective I and Q binary PRN codes in boolean form, and $\overline{P_I(t)}$ represents a NOT operation on code $P_I(t)$. As they are generated using m-sequence PRN codes, QPSK codes used for DEHoI retain the same properties as discussed in Chapter 3, and the main parameters that we refer to consistently are the code length, which remains $L_{\text{code}} = 2^N - 1$, and the chip frequency. Spectrally, the QPSK code is analogous to a π modulation depth binary code, with the I and Q individual codes contributing to half the modulation depth. An example 3 bit QPSK code is shown in Figure 8.3.

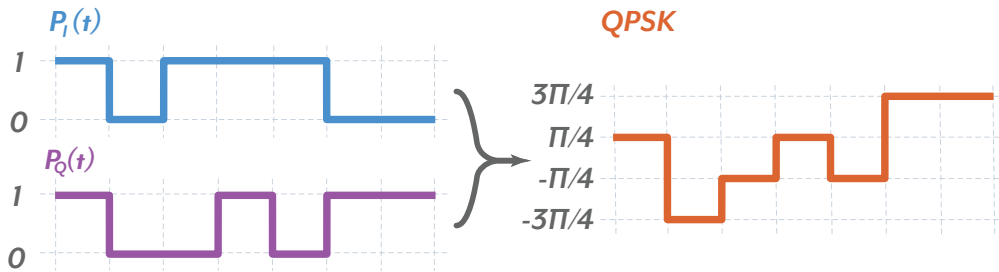


Figure 8.3: An example of how two phase shifted binary PRN codes, equivalent to those used in Digitally enhanced Heterodyne interferometry are able to be combined to generate a single QPSK code. The QPSK code retains the same bit depth and code length as the generating PRN sequences, which in this example, is 7 chips long, as per a 3 bit code

In an optical setup, the QPSK modulation can be applied in two main ways. Firstly, as with heterodyne systems, an electro-optic modulator (EOM) can be used. This allows for fast modulation frequencies on the order of 100 MHz or greater, however, as the electro-optic voltage is susceptible to variation with thermal and vibration effects, this can lead to modulation angle errors as the modulation depth becomes a time varying function[5]. As demonstrated by Sutton, these limitations can be overcome by monitoring the phase shift and applying control feedback to the modulator bias ports.

The second method, and the one used by the fibre frequency reference, is to use acousto-optic modulators (AOMs). These modulators are typically used to introduce frequency shifts, as was the case in the acoustic sensing array demonstrated in Part I. However, by controlling the phase of the AOM drive frequency, an exact phase shift can be applied in addition to the frequency shift[100]. In this way, we can significantly reduce, or eliminate many of the calibration issues found with electro-optic modulators[5].

If we consider the Mach Zehnder interferometer from Figure 8.1, we can make it DEHoI compatible by adding in a common path phase shifting modulator, shown in Figure 8.4.

Immediately following the modulator, we can describe the QPSK modulated electric field with the following expression. Note that the constellation may undergo a global rotation without loss of generality.

$$E(t) = \tilde{E}(t)(C_I(t) + iC_Q(t))e^{i\omega t + \phi(t)} \quad (8.2)$$

Where $C_I(t)$ and $C_Q(t)$ are mappings of the I and Q codes to ± 1 . Upon propagating

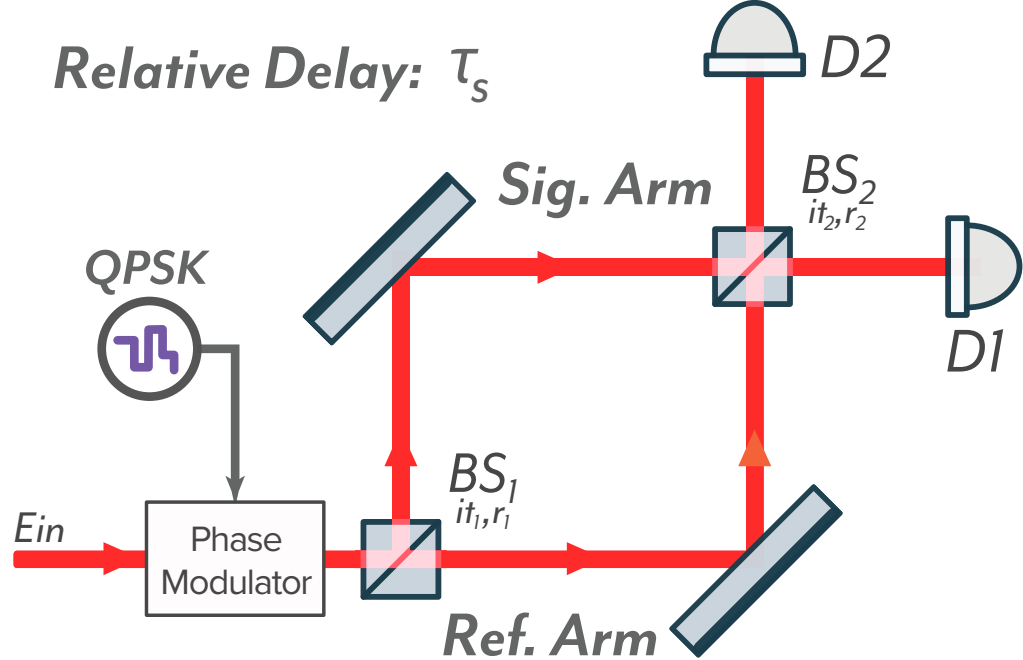


Figure 8.4: The inclusion of a phase modulator which is common to both the signal and reference arms enables the use of Digitally enhanced Homodyne interferometry. In this case, any path length difference between the two arms constitutes a proportional time difference between the QPSK code propagating through each arm, τ_S . When combined at the photodetector, this differential delay can be demodulated through the double demodulation architecture.

through the arms of the interferometer and returning through the centre beam splitter, the electric fields of the signal and reference arm can be written as follows at the photodetector:

$$\begin{aligned} E_S(t) &= \tilde{E}(t - \tau_S)(C_I(t - \tau_S) + iC_Q(t - \tau_S))e^{i\omega t + i\phi(t - \tau_S)} \\ E_R(t) &= \tilde{E}(t - \tau_R)(C_I(t - \tau_R) + iC_Q(t - \tau_R))e^{i\omega t + i\phi(t - \tau_R)} \end{aligned}$$

Here, the signal field and the local oscillator are delayed relative to each other by a fixed time-of-flight delay, τ_S . The corresponding code delay between the two fields results in effectively two unique QPSK codes being present at the detector, one for the signal field, and one for the local oscillator. The optical power on the photodetector is then given by the modulus square of the superposition of the two fields. If we consider only the modulated components of the optical power, discarding the static DC power, the photodetector output can be written in terms of only code modulated fields. Additionally, as orthogonal PRN sequences are sufficiently uncorrelated, higher order codes have also been discarded for this calculation. The retains four first order code terms which we use for the demodulation

process. Each of these terms represent a combination of I and Q binary code modulated onto the signal or local oscillator field, as shown below:

$$\begin{aligned}
 P_{D1} = & \tilde{E}(t)\tilde{E}(t - \tau_S)C_I(t)C_I(t - \tau_S) \cos(\Delta\phi(t)) & (I_R \& I_S) \\
 & + \tilde{E}(t)\tilde{E}(t - \tau_S)C_I(t)C_Q(t - \tau_S) \sin(\Delta\phi(t)) & (I_R \& Q_S) \\
 & - \tilde{E}(t)\tilde{E}(t - \tau_S)C_Q(t)C_I(t - \tau_S) \sin(\Delta\phi(t)) & (Q_R \& I_S) \\
 & + \tilde{E}(t)\tilde{E}(t - \tau_S)C_Q(t)C_Q(t - \tau_S) \cos(\Delta\phi(t)) & (Q_R \& Q_S)
 \end{aligned} \quad (8.3)$$

As can be seen from the above expression, the photodetector output is doubly modulated. The extraction of the phase difference between the two arms therefore requires a two stage, or double demodulation process, which is described in the following section.

8.3 Double Demodulation

As both the local oscillator and signal fields are encoded in this readout scheme, a double demodulation architecture is required to extract the phase difference between the two fields[5]. The breakdown of the constituent components described in Equation 8.3, as shown in Figure 8.5 highlights how they can be used to project back to recover the phase difference between the two fields.

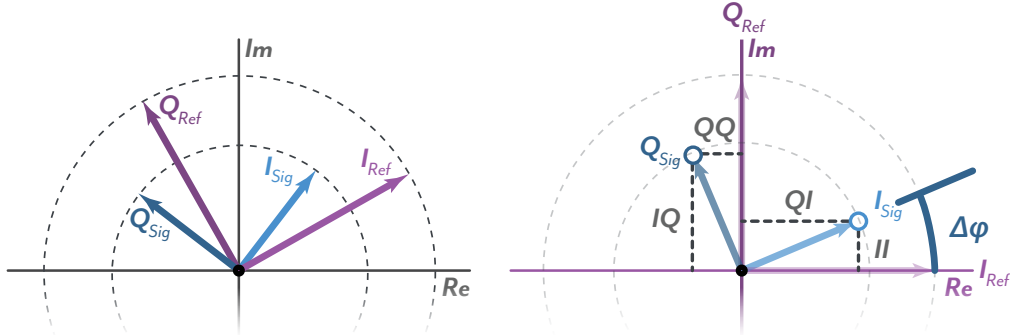


Figure 8.5: Double demodulation reconstructs the phase difference between the optical fields at the reference (ref) and signal (sig) time-of-flight delays. If we consider the phasor representation of the electric field at these two delays, we can represent them in terms of an orthogonal IQ basis (left). Rotating to the frame of the reference field, we can characterise the phase projections of each of the double demodulation terms presented in Equation 8.3 (right). Using these projections, we can then reconstruct the phase difference $\Delta\phi$ between the two fields.

Following digitisation, we apply the same decoding procedures as the heterodyne case, by correlating against two copies of the original QPSK code. The demodulation codes are time shifted such that they are decoding at two unique delays, τ_i and τ_j . Since we can break down the QPSK code into two binary codes in the I and Q quadratures, when

combined with the two demodulation delays, this leaves 4 permutations of the decoding operation as listed below:

$$\begin{aligned} II &\Rightarrow C_I(t - \tau_i)C_I(t - \tau_j) \\ IQ &\Rightarrow C_I(t - \tau_i)C_Q(t - \tau_j) \\ QI &\Rightarrow C_Q(t - \tau_i)C_I(t - \tau_j) \\ QQ &\Rightarrow C_Q(t - \tau_i)C_Q(t - \tau_j) \end{aligned}$$

From these code combinations we infer the physical meaning of the demodulation process. Demodulation with II and QQ codes represent the I and Q codes interfering with time shifted versions of the same. In other words, they do not have a relative phase shift between them, and thus represent the 'in-phase' component of the signal. The remaining two terms, IQ and QI represent the interference of one code against another. These cross-terms interfere against each other with a $\pi/2$ relative phase shift, thus representing the 'Quadrature' component of the signal.

Applying the demodulation codes to the digitised photodetector output, results in the following four auto-correlation functions representing each of possible projections:

$$\begin{aligned} II(t) &= \sum_{t=0}^{L_{\text{code}}} C_I(t - \tau_i)C_I(t - \tau_j) \times P_{D1}(t) \\ IQ(t) &= \sum_{t=0}^{L_{\text{code}}} C_I(t - \tau_i)C_Q(t - \tau_j) \times P_{D1}(t) \\ QI(t) &= \sum_{t=0}^{L_{\text{code}}} C_Q(t - \tau_i)C_I(t - \tau_j) \times P_{D1}(t) \\ QQ(t) &= \sum_{t=0}^{L_{\text{code}}} C_Q(t - \tau_i)C_Q(t - \tau_j) \times P_{D1}(t) \end{aligned}$$

Where L_{code} is the code length of QPSK code and $P_{D1}(t)$ is the digitised photodetector output. Computing the auto-correlation by integrating over the code length, we arrive at the following expressions for each of the IQ projections:

$$\begin{aligned} II(t) &= \mathcal{A}_{ij}\beta \cos(\Delta\phi(t)) \\ IQ(t) &= \mathcal{A}_{ij}\beta \sin(\Delta\phi(t)) \\ QI(t) &= -\mathcal{A}_{ij}\beta \sin(\Delta\phi(t)) \\ QQ(t) &= \mathcal{A}_{ij}\beta \cos(\Delta\phi(t)) \end{aligned}$$

Where \mathcal{A}_{ij} represents the auto-correlation magnitude for codes of delay τ_i and τ_j . The coefficient β is given by $\tilde{E}(t - \tau_S)$; the optical power carried by each term. Returning to the example of the Mach Zehnder interferometer from the previous section, we established a relative delay between the two fields of τ due to the length difference between the local oscillator and signal arms. As with DEHeI, in order to recover the maximum auto-correlation, the demodulation delays must be matched to the optical time-of-flight for each of these fields. We therefore tune the demodulation delays, τ_i and τ_j to match the LO

and signal code delays: $\tau_i \rightarrow 0$ and $\tau_j \rightarrow \tau_S$. As with DEHeI, the maximum correlation is given by the code length, L_{code}

$$\mathcal{A}_{0,\tau_S} = L_{\text{code}}$$

The final step in the double demodulation process is the recovery of the full phase projection. For this, we refer back to the physical description of the demodulation process. As shown in Figure 8.5, the ‘in-phase’ or I component of the phasor is given by the II and QQ projections while the ‘quadrature’ or Q component is given by the remaining cross-terms. Computing the vector sum of these components, we can arrive at the following phase projection:

$$s(t) = [II(t) + QQ(t)] \hat{I} + [IQ(t) - QI(t)] \hat{Q} \quad (8.4)$$

We can then compute the phase difference by taking the arctangent of the Quadrature and In-phase components:

$$\Delta\phi(t) = \arctan\left(\frac{IQ(t) - QI(t)}{II(t) + QQ(t)}\right) \quad (8.5)$$

So far we have considered the case where the reference and signal fields are correctly decoded. In the situation where there are multiple fields present or the demodulation delays are out of phase with any of the received codes, the auto-correlation amplitude reduced to -1. This minimises the coupling of spurious fields into the desired measurement, with suppression as per the heterodyne case, equivalent to the QPSK code length.

8.4 FPGA Implementation

Another major difference between the homodyne and heterodyne variants of digital interferometry is the implementation of the demodulation process on a field programmable gate array (FPGA). In the heterodyne case, the demodulation of the code and the optical phase are decoupled, the former being handled by the auto-correlation and the latter by IQ demodulation. For the homodyne case, the combined nature of the code demodulation and phase readout requires the implementation of a technique named ‘binning’. This method uses the pre-determined QPSK logic to correlate a received sample with a particular measurement quadrature, as shown in Figure 8.6. We subsequently ‘bin’ or associate the sample with a particular phase quadrature.

As shown in Figure 8.6, when the demodulation code is matched to the received code, this process separates the samples correctly. When the demodulation code is out of phase with the received code, the same process is equivalent to re-encoding with another QPSK code. This is functionally identical to the heterodyne case, causing incorrectly decoded signals to be spread out as broadband noise.

The binning operation is able to demodulate one code at a time. In order to perform the double demodulation, two of these binning operations are cascaded. The full architecture is shown in Figure 8.7. The output of the first binning stage produces four terms, one for each quadrature. Subtracting the I and $-I$ terms returns the total ‘in-phase’ component for the first demodulation stage. The total ‘quadrature’ component can be similarly

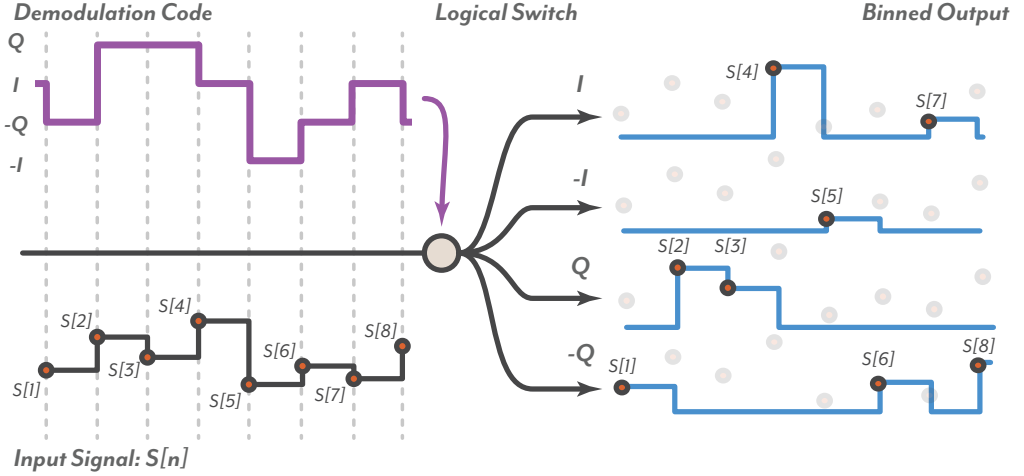


Figure 8.6: The binning architecture uses an input demodulation QPSK code to sort incoming samples into IQ projections. Following the binning process, the samples in each channel are integrated over a code length, resulting in an averaged value for each of the four projections. When the delay of the demodulation code coincides with an optical delay, the projections imparted by the modulation code are correctly identified and sorted appropriately, with the integration resulting in an average value for each quadrature. When the delay does not match a received code, the binning process does not correlate with the phase projections imparted by the received code. The resultant output after the integration averages towards zero.

calculated. The I/Q data streams become inputs into two parallel binning operations for the second demodulation stage. Both of the parallel second stages produce I and Q outputs, representing the four combinations of II, IQ, QI and QQ as discussed previously.

The penultimate stage of the demodulation process is averaging which is handled by a decimation filter of either 1st or 2nd order. The algorithm is reliant of very few digital signal processing resources as the operations are all boolean or two bit switching operations. This portion of the demodulation uses significantly fewer resources than the equivalent heterodyne demodulation, largely due to the lack of multiplication operations.

In the experiments presented in this thesis, following the output of averaged I/Q data, the phase reconstruction, shown in Figure 8.7, is carried out in post-processing. If real-time phase reconstruction is necessary, a CORDIC algorithm can be used perform the arctangent operation on FPGA[101]. In this instance a heterodyne system with a phase locked loop (PLL) readout would also facilitate real-time phase output, and consume a comparable amount of FPGA resources.

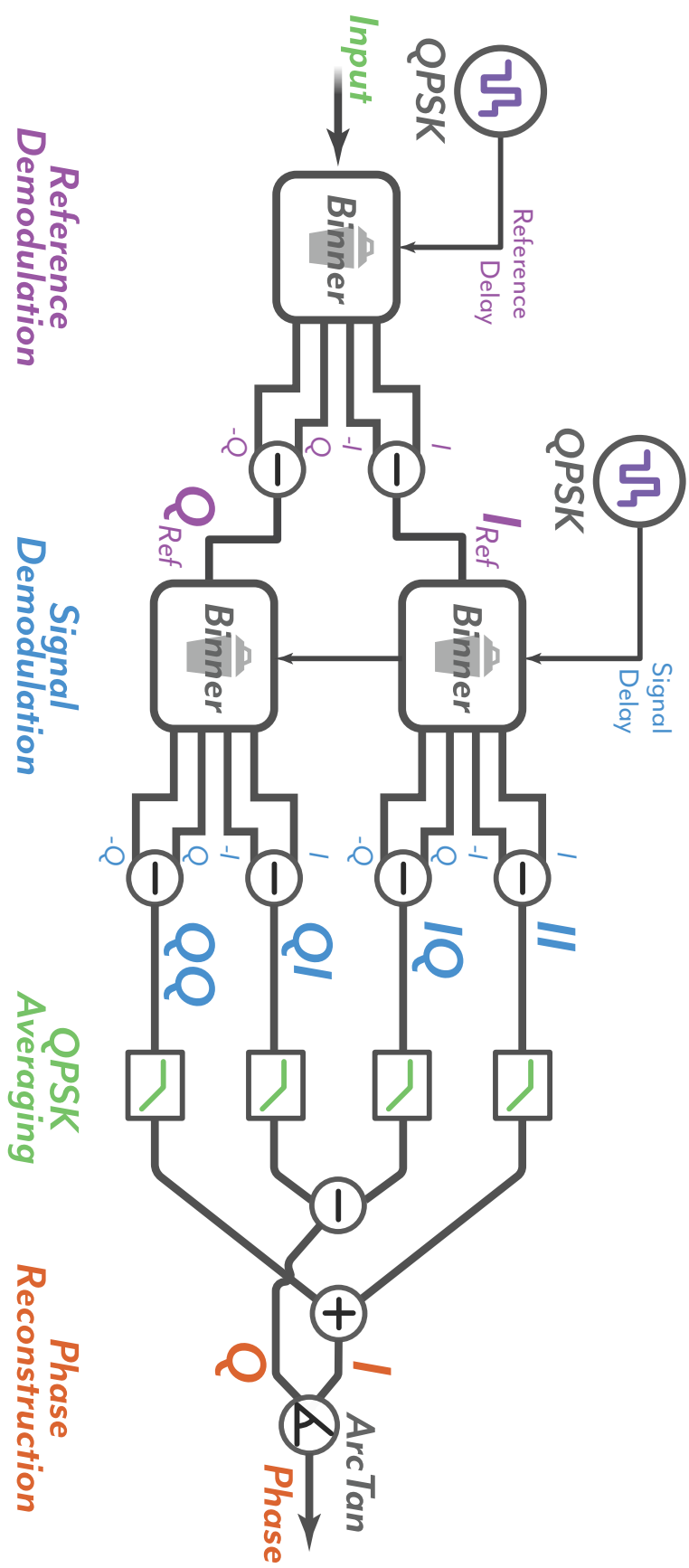


Figure 8.7: The full double demodulation FPGA architecture. Following digitisation, the input is binned according to the reference delayed QPSK code, as per the example shown in Figure 8.6. The first demodulation is equivalent to rotating the phasor to the frame of the reference field, as shown in Figure 8.5. The second demodulation computes the projections of the signal field with respect to the IQ projections of the reference field. The resultant four projections (I_I, Q_Q, I_Q, Q_I) are then used to reconstruct the final IQ projection of the phase difference between the two fields, as per Equation 8.4. The phase is then computed using an arctangent as per Equation 8.5.

Fibre Interferometer Frequency Reference

In this chapter we outline the design and implementation of the fibre interferometer frequency reference. We start with a discussion of the meaning of the phase readout and how it enables the tracking of laser frequency noise. Following this, we go through a detailed description of the experimental setup, including the challenges associated with the generation of QPSK modulation. We conclude by considering how the stability of the system may be characterised and introduce the differential phase measurement method.

9.1 Conceptual Design

The phase noise of an optical source is most readily measured by making a time-delayed comparison of the source with itself. As the instantaneous phase noise is unique to the time delay, there is a resultant phase difference between the two compared optical fields. The magnitude of the phase difference is also proportional to the phase stability of the optical source, which can be tracked using an interferometric readout. Measuring over time, we then build up a picture of the phase noise dynamics of the optical source.

In order to generate a differential time delay, an unbalanced interferometer can be used. This includes arm-length different Michelson or Mach Zehnder configurations as well as optical cavities. If we consider an optical source with a phase noise, $\phi_n(t)$, interrogating an interferometer with path length difference ΔL , the optical field at the detector is given by the following expression:

$$E_{D1}(t) = ir_2 t_1 \tilde{E}(t) e^{i\omega t + i\phi_n(t)} + ir_1 t_2 \tilde{E}(t - \tau) e^{-\alpha \Delta L} e^{i\omega t + i\phi_n(t - \tau)}$$

Where $\tilde{E}(t)$ is the amplitude of the input field and ω , the optical frequency. There is an extra exponential decay with coefficient α representing the optical fibre attenuation. As these interferometers are unbalanced on the order of kilometres, fibre attenuation is no longer negligible. The delay τ represents the transit time difference between the two arms of the interferometer and can be written in terms of the path length difference ΔL :

$$\tau = \frac{n \Delta L}{c}$$

where n is the refractive index of the optical fibre. Following this we can write down the AC optical power at the detector, again assuming a 50:50 splitting ratio at each of the beam splitters.

$$P_{D1}(t) = \frac{\tilde{E}(t)\tilde{E}(t-\tau)e^{-\alpha\Delta L}}{2}(1 + \cos(\Delta\phi(t))) \quad (9.1)$$

where $\Delta\phi(t)$ is the differential phase between the two interferometer arms; $\phi_n(t) - \phi_n(t-\tau)$. For a given phase difference $\Delta\phi(t)$, the instantaneous frequency difference can then be computed by factoring in the arm length difference of the interferometer:

$$\Delta f(t) = \frac{c}{2\pi n \Delta L} \Delta\phi(t - \tau) \quad (9.2)$$

where ΔL is the arm length difference of the interferometer and n the refractive index of the optical fibre. This calibration from phase to frequency shows that the responsitivity of the interferometer is directly proportional to the arm length difference. That is to say, as the arm length difference of the interferometer increases the phase response of the interferometer becomes more sensitive to frequency shifts in the source.

In designing a fibre optic interferometer, there are a number of challenges which are unique to fibre optic systems. This is namely the effects of spurious interference from Rayleigh scattering, optical path length changes from thermal expansion and birefringence drifts which induces polarisation phase noise in the readout. In designing a fibre optic frequency reference we must therefore consider and address these effects.

The cornerstone of the frequency reference is the phase interrogation method. For this, we use digitally enhanced homodyne interferometry (DEHoI) to interrogate the phase relative to the fibre interferometer. By doing this, we are able to reduce the effects of spurious interference, allowing for significantly longer fibre lengths to be utilised without significantly impacting the noise performance due to the increased Rayleigh scattering. We highlight details and limitations of Rayleigh scattering reduction using DEHoI in Chapter 10.

Secondly, the DEHoI readout enables the minimisation of mechanical complexity. Instead of using fibre couplers, a single fibre optic spool can be used with partial reflections at each end, as shown in Figure 9.1. Normally this would cause an etalon to form between the two reflection surfaces, but due to the spread-spectrum modulation, these effects are not coherent and suppressed due to the shortened optical coherence length.

In this configuration, the interferometer is acting equivalent to a Michelson interferometer. As such, it is susceptible to first order Rayleigh scattering, which provides a simple, and effective platform to test the spurious interference rejection capabilities of digitally enhanced interferometry.

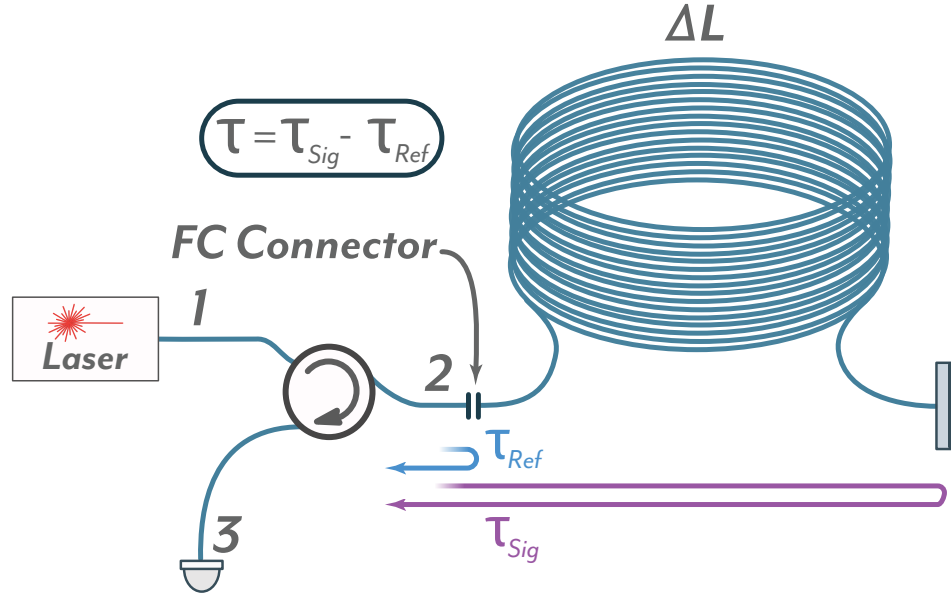


Figure 9.1: A conceptual diagram of the in-line frequency concept. It is functionally identical to an arm-length unbalanced Michelson interferometer without the use of a fibre coupler. The front reflection is provided by an FC fibre connector. A silvered fibre reflector is used for the rear reflection. The path length difference between the two arms is therefore two times the length of the coil. This provides two unique delays, τ_{Ref} and τ_{Sig} which we measure the phase shift between using the QPSK double demodulation method.

9.2 Experimental Implementation

The fibre frequency reference can be broadly considered as two main subsystems. Starting with the optical system, as shown in the experimental diagram in Figure 9.2, an Orbita Lightwave 1550 nm fibre coupled laser with a linewidth of 300 Hz is used as the main interrogation laser. We modulate on the QPSK code using an acousto-optic modulator (AOM).

For the experiments presented in the following chapters we use two different modulators. For the low DEHoI modulation frequency tests in Chapter 10 and the infrasonic tests in Chapter 11, we use an IntraAction FCM-401E5A acousto-optic modulator (AOM). The drive frequency for this modulator is readily compatible with the digital signal processing capabilities however it has a limited modulation bandwidth. In order to extend to testing higher modulation frequencies in Chapter 10, we use a Gooch and Housgo Fibre Q acousto-optic modulator with a central frequency of 200 MHz[102] for measurements exceeding a 2 MHz chip frequency. The challenges with driving the G&H modulator are discussed in detail in Section 9.3.

Both AOMs functionally serve the same purpose: to encode the optical field with DEHoI modulation. Once encoded, the optical beam is then split between two in-line Michelson interferometers. The in-line interferometer consists of a single compacted, 4 km fibre spool. There are two reflection points per interferometer, the short (reference) arm reflection is caused by a flat-surfaced fibre connector (FC/PC) providing an approximately 8% reflectivity due to Fresnel reflection at the glass/air/glass interfaces. The long (signal)

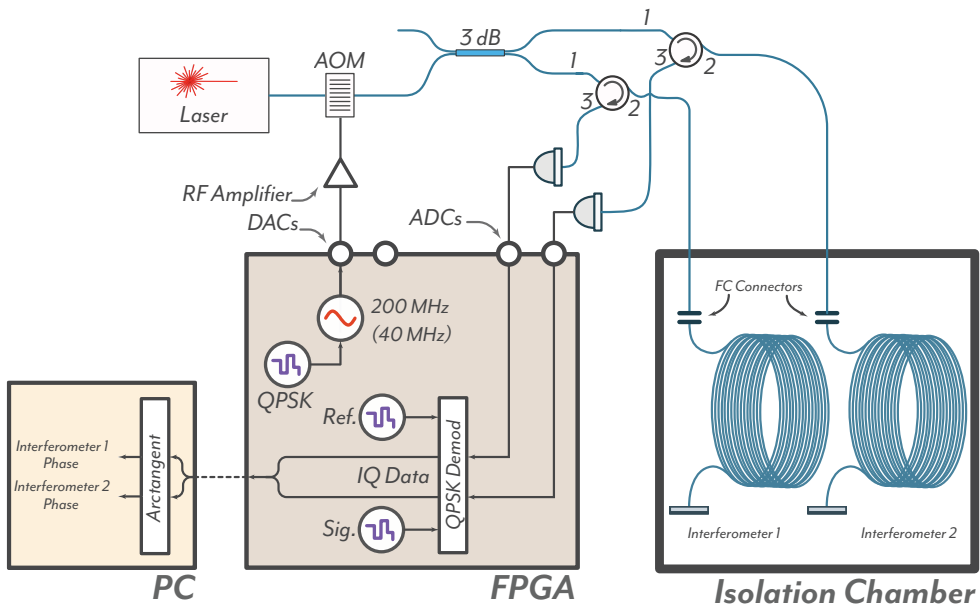


Figure 9.2: Optical Schematic for the Inline Fibre Optic Frequency Reference. We modulate a test laser using an AOM with QPSK modulation generated on an FPGA. In the experiments to follow we use two AOMs, operating an RF frequency of 40 MHz and 200 MHz respectively, also generated on the FPGA. In addition to the QPSK modulation, we generate phase ramp which is used to upshift any re-entrant code noise to the ramp frequency. The modulated optical output is sent to two identical interferometers. The interferometers use 4 km long fibre spools, resulting in a path length difference between the two arms of 8 km. The return signal is picked off using a circulator, detected and digitised. The double demodulation process decodes at two delays, reference and signal, corresponding to the time of flight to the two in-line reflections. This is done in parallel for both interferometers. The output IQ data is serialised and parsed to a networked computer for recording and computation of the arctangent operation.

arm reflection is provided by a single mode fibre retro-reflector (P5-SMF28ER-P01-1) from Thorlabs. The reflected fields from the interferometer are tapped off using circulators and detected using Newfocus 1811 FC detectors.

In order to provide thermal and mechanical isolation to the interferometers, the fibre spools that make up the bulk of the interferometer are placed in an isolation chamber, shown in Figure 9.3. The isolation chamber consists of nested polystyrene and aluminium chambers. Both of the aluminium chambers are constructed of 1 cm plate aluminium and the inside chamber is hermatically sealed. The polystyrene layers are each 5 cm thick. The interferometer is patched out using a 2 fibre feedthrough, which is sealed using adhesives. However, as the two interferometers are housed inside the same isolation chamber, this provides a degree of common mode rejection of thermal effects, which are independently characterised in Chapter 11.

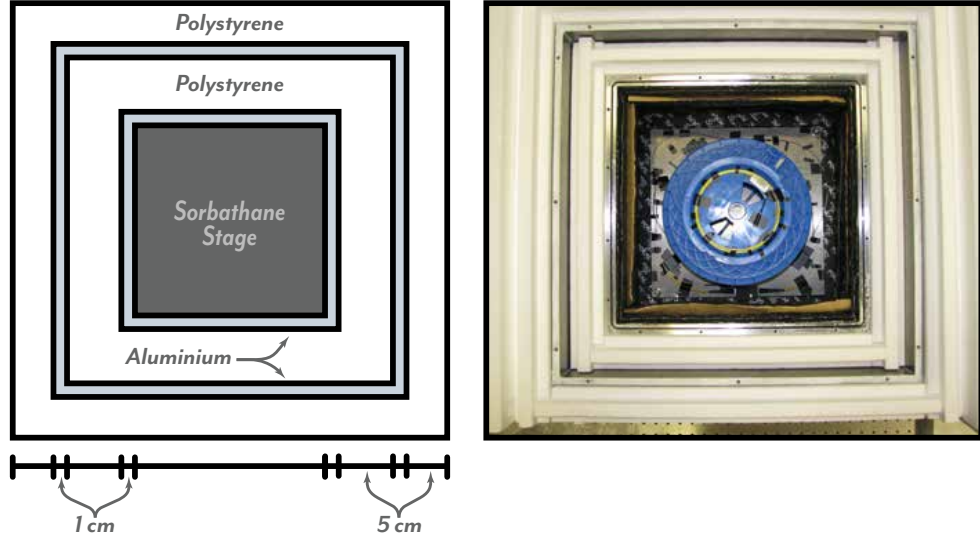


Figure 9.3: The thermal and acoustic isolation for the interferometers is achieved passively through the isolation chambers designed and built by McRae. They consist of cascaded polystyrene and aluminium boxes which act as a two stage low pass filter with a corner frequency of 10.5 hours[103]. A photo of the opened chamber is shown on the right. Note for the in-line configurations, two separate fibre spools were fitted into a single chamber.

The readout for the two interferometers was implemented through the digitally enhanced homodyne readout. The generation of the QPSK code for modulation and the AOM drive frequency was handled on an NI 7966R Virtex 5 FPGA running at a clock frequency of 125 MHz. Analog interface with the digital system was provided by the NI 5782 transceiver card, with 500 MS/s output DACs and 250 MS/s ADCs. Throughout the testing, a number of chip frequencies were tested, ranging from 100 kHz through to 41 MHz.

In addition to the QPSK generation, the AOM drive frequency was further modulated with a seradyne waveform to upshift code noise[47, 96]. Code noise is a phase error which occurs when there is an elation or multi-pass optical delay which causes repeated codes to be partially demodulated. By modulating with a seradyne waveform matched to the FSR of the interferometer, we scan the interferometer through a full 2π modulation. Delays between the two arms are therefore upshifted to a set of harmonics at the seradyne frequency, removing broadband code noise from the measurement.

The AOM drive frequency, with both QPSK and seradyne modulation were all generated on the FPGA. Once output from the DACs, was passed through a Minicircuits ZHL-32A or ZHL-1-2W-S¹ increasing the RF power to 26 dBm, which was sufficient to drive the AOM.

Following photodetection, the output from the individual interferometer photodetectors (NewFocus 1811) was digitised using the two input channels on the NI 5782 transiever. Once digitised, parallel double demodulation was carried out on the two

¹The ZHL-32A was used in conjunction with the low speed 40 MHz AOM. In order to amplify the 200 MHz carrier for the high speed AOM, the higher bandwidth Minicircuits ZHL-1-2W-S was used in its stead

ingested signals, producing an I/Q projection for each interferometer at a decimated rate. The decimated rate is an integer fraction of the code repetition rate.

The FPGA output was serialised and parsed to a network computer for recording and visualisation. The arctangent operation was carried out on the network computer in post processing. While not explored for this work, a CORDIC algorithm can be efficiently implemented on an FPGA for real-time arctangent operations for applications involving phase feedback control. In the following section, we discuss in detail the generation of the QPSK modulation and bandwidth effects of the NI 5782 outputs and Gooch and Housgo AOM.

9.3 QPSK Modulation Generation

A key component of the frequency reference architecture is the generation of the QPSK code and modulation of the code onto the interrogating optical beam. The generation of the code is handled on the NI 7966R FPGA. The algorithm consists of a two stage process. Firstly, two m-sequence PRN codes are generated in parallel through a linear feedback shift register algorithm (LFSR) analogously to the method described in Chapter 3.

The two codes are of the same length but are generated using different initial LFSR states (seeds). This effectively starts the two generators at different points along the code, time-shifting one code relative to the other by an integer number of chips. As m-sequences are only correlated when in phase, the time-shift makes the two generating m-sequences orthogonal. Following the code generation, the boolean output from each of the generators undergoes the logic described in Chapter 8. The boolean logic is then converted to a binary integer representation and scaled to provide the correct, $\pi/4$, phase shift.

As acousto-optic modulators are used in this optical system, the QPSK code requires a RF carrier matched to the AOM resonant frequency. In order to simplify signal generation chain, the RF drive is generated through direct digital synthesis (DDS) in parallel to the code generation. In the case of the IntraAction AOM, the comparatively slow 40 MHz drive frequency and ≤ 2 MHz modulation frequencies are readily achievable. We therefore focus on the signal generation process for the G&H high speed AOM, though the same methodology applies to both modulators.

For the G&H modulator, the required drive frequency of 200 MHz was generated at the full DAC output rate of 500 MS/s. In order to achieve these speeds, we implemented a four times parallelised sine wave generator operating at a clock frequency of 125 MHz. However, the conversion from the digital to analog domains causes imaging around the Nyquist frequency, which for this system is 250 MHz. As a result, the carrier frequency of 200 MHz is imaged around the Nyquist frequency, generating an additional 300 MHz tone within the second Nyquist zone. This in turn generates an additional beat note at the difference frequency of 100 MHz as shown in Figure 9.4. These image tones in subsequent Nyquist zones can be mitigated with in-DAC interpolation [104]. As this was not available, in order to reduce the impact of these tones, analog low pass filters were used to cut the DAC response above 200 MHz.

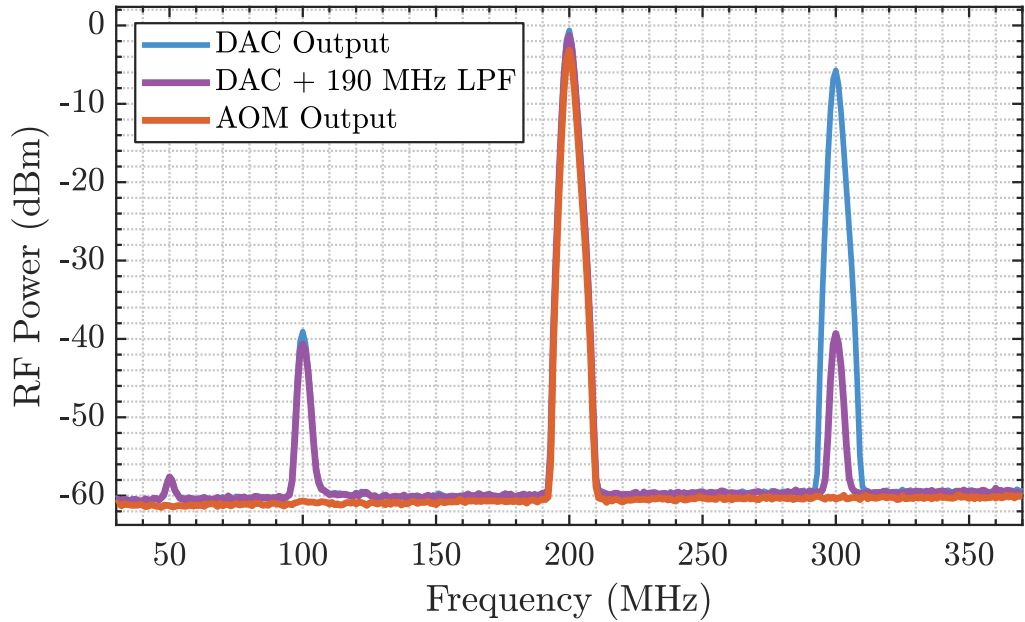


Figure 9.4: The generation and conditioning of the AOM drive frequency generated using the FPGA. As we are digitally generating a 200 MHz tone, which is close to the 250 MHz Nyquist frequency of the DAC (blue). This results in a large response mirrored around Nyquist, and a subsequent difference frequency at 100 MHz. An additional 190 MHz LPF reduces the magnitude of the 300 MHz tone (purple), and when combined with the AOM response, only the 200 MHz tone is preserved as seen by the AOM output (orange).

This however does not remove the 100 MHz beat note as that interference occurs during the digital to analog conversion process. In order to remove the 100 MHz component, we rely on the frequency response of the AOM. To characterise the AOM bandwidth, we construct a heterodyne interferometer, measuring the power of the heterodyne beat note as a function of the AOM drive frequency, shown in Figure 9.5.

For this test, the AOM drive frequency was driven by a 250 MHz signal generator built into the Moku:Lab. We retain the 190 MHz analog LPF and RF amplifier for this measurement to give a complete picture of the combined AOM + RF amplifier + LPF response. As shown in Figure 9.5, at 100 MHz, the AOM response provides 20 dB of suppression. Since the 100 MHz beat is approximately 40 dB smaller than the main 200 MHz carrier field, this provides a total suppression of 60 dB relative to the carrier. Using the 190 MHz LPF on the DAC output ensures that a similar suppression is achieved at 300 MHz, as shown in Figure 9.4.

With the AOM characterisation complete, we introduce the QPSK modulation on top of the 200 MHz carrier. Figure 9.6 shows the output response of the AOM as measured through a heterodyne measurement compared against a bit-accurate FPGA simulation of the QPSK generation architecture. This illustrates the bandwidth effects of both the RF filters, amplifier and the AOM. Due to the asymmetry of this modulation around the 200 MHz carrier frequency, we hypothesize the modulation will introduce residual amplitude noise into the system. This hypothesis is in the process of being investigated at the time of writing.

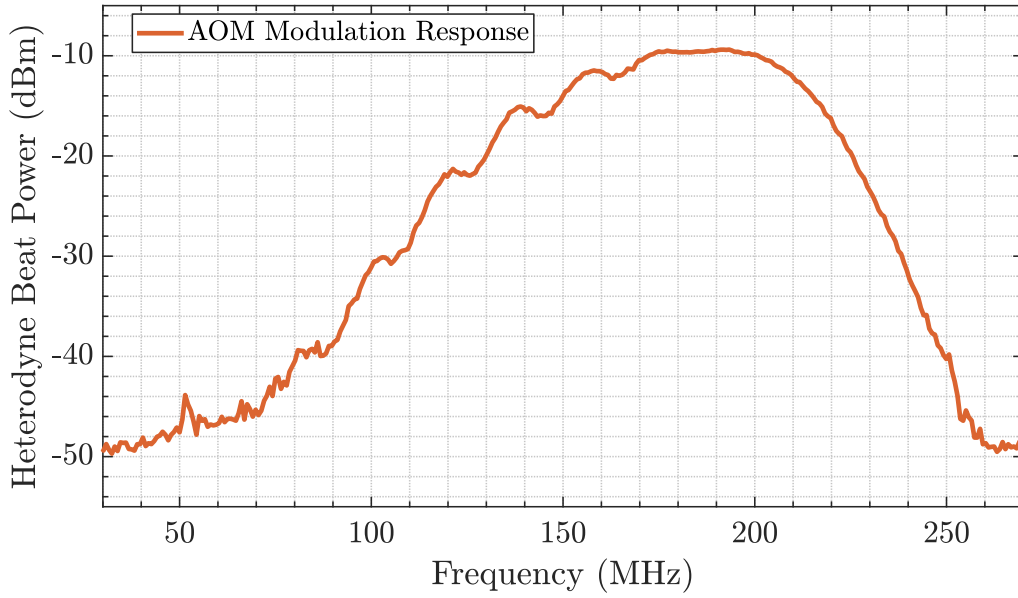


Figure 9.5: Transfer function measurement of the high speed G&H AOM, RF amplifier and signal conditioning filters. The AOM has a centre frequency of 200 MHz and an effective modulation bandwidth of ~ 50 MHz. The smooth roll-off above 200 MHz is due to the 190 MHz LPF.

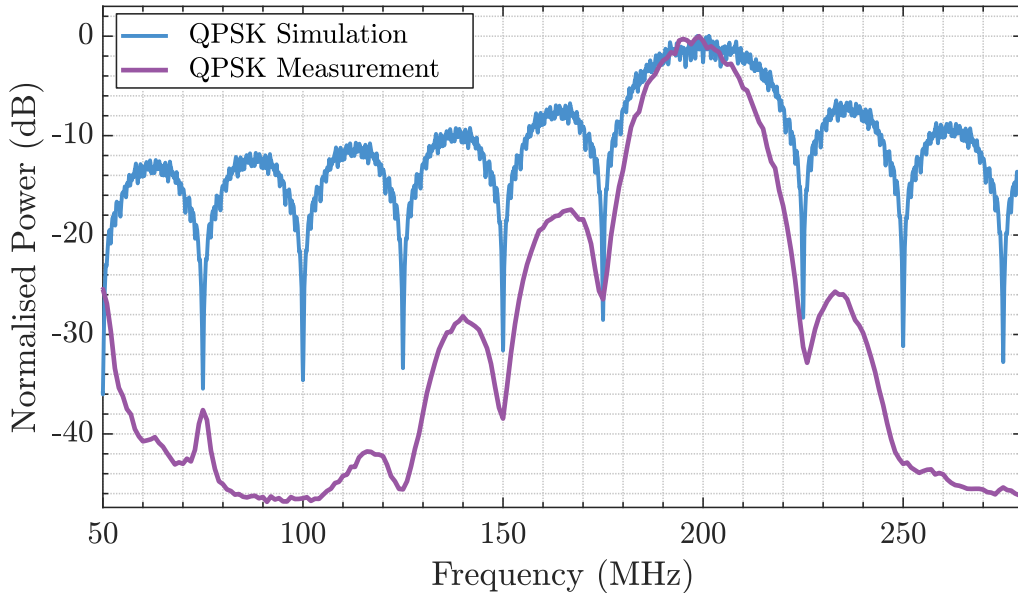


Figure 9.6: The QPSK spectrum (purple) was measured using a self-heterodyne measurement, therefore shaped by the AOM/filter response. It is plotted against an simulated spectrum without the AOM response, generated using MATLAB (blue), showing the effect of the transfer function of the AOM/filter system, shown in Figure 9.5.

9.4 Differential Stability Measurement

The readout from each individual interferometer tracks the phase evolution of the interrogating light source with respect to the fibre frequency reference. As with all frequency references, the main metric that we are concerned with its stability. In order to obtain a quantitative measure, we utilise the second, identical interferometer to provide an independent measurement of the laser phase noise. The phase evolution of the interrogating laser with respect to the two interferometers is shown in Figure 9.7a.

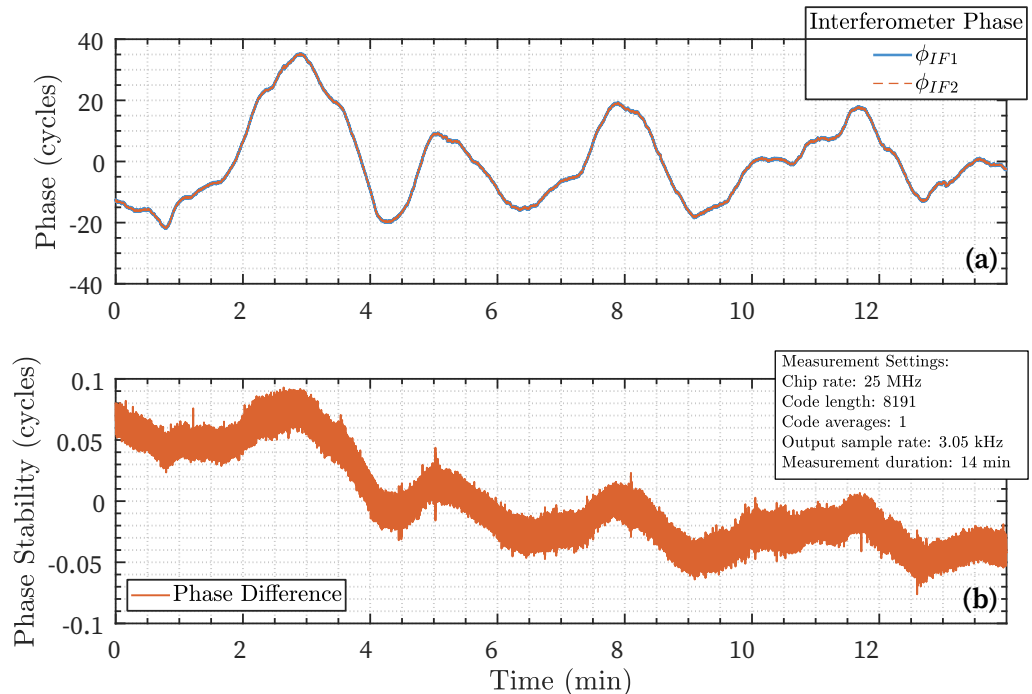


Figure 9.7: A 1000 second measurement of two in-line interferometers showing the interferometer phase evolving with laser frequency (a). The difference between the two interferometers determines the relative phase stability shown in the second plot (b).

By interrogating both interferometers with the same source, laser frequency noise is common to both and cancelled out through a differential measurement. The residual noise floor is therefore due to the uncorrelated noise of the two references, such as thermal expansion, thermo-optic effects on the fibre refractive index, mechanical coupling or scattering induced phase noise. This residual noise floor determines the relative stability of the two interferometers.

The main parameters we can alter with the frequency reference are the modulation frequency, the code length and the averaging time, in integer multiples of the code length. In the example shown below, we use a 13 bit code, with 8191 chips. This code modulated at 25 MHz using the G&H AOM. Through the demodulation process, the code correlation is computed by integrating once over the code length.

Given the chip rate and code length, the averaging time results in an output sample rate of 3.05 kHz. The raw phase output of the two interferometers is shown in the time domain traces of Figure 9.7(top) with the phase stability of the two interferometers shown

in 9.7(bottom). Following the phase extraction we also calibrate to frequency using the approach detailed in Section 9.1. Finally, we compute the amplitude spectral density of the readout using the pwelch method. The resultant spectral density is plotted in Figure 9.8.

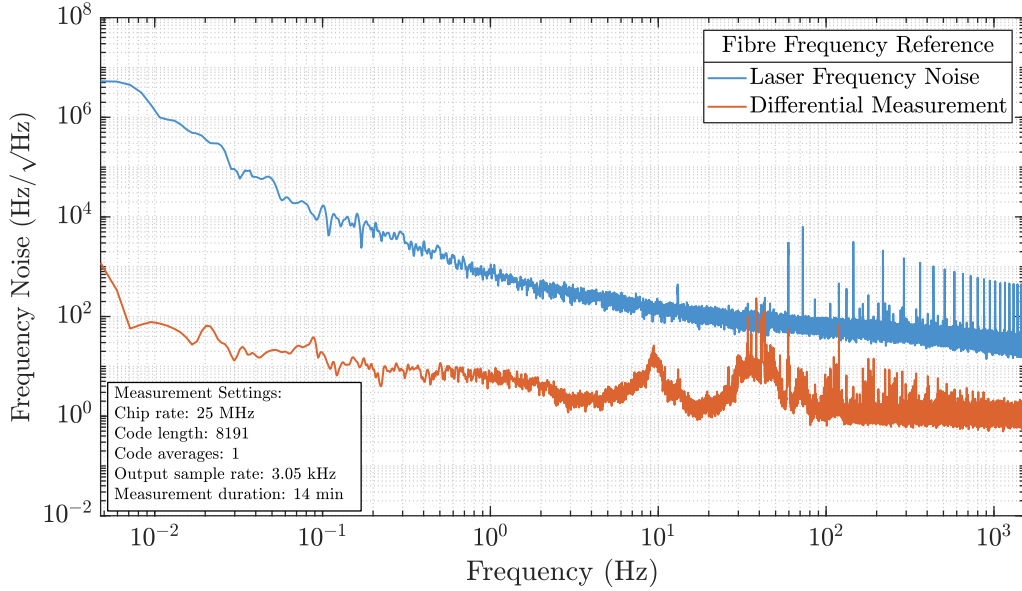


Figure 9.8: Taking the measurement shown in Figure 9.7, we compute the amplitude spectral density using the pwelch method. The laser frequency noise of the test laser is shown in the first trace (blue). The relative stability between the two references is shown in the second trace (orange). The discrete harmonics present at audio frequencies are due to the upshifting of code noise through seradyne modulation. Also identified are the key noise sources, with reference to the frequency regime that occur.

From the relative stability spectral density, Figure 9.8, we can identify several different noise processes. Below 10 mHz, we see the start of a low frequency roll up representing both thermal and polarisation induced phase noise. From there to 100 mHz, the broadband shelf noise feature represents the cyclic phase error induced by Rayleigh scattering in the optical fibre. We go into further detail regarding this in Chapter 10. The high frequency noise floor reaches a broadband level of $1 \text{ Hz}/\sqrt{\text{Hz}}$ from 11 Hz with some acoustic pick up in the sub-100 Hz range.

This is reflected in the computation of the Modified Allan deviation, shown in Figure 9.9, which was carried out using the Stable32 software package[66]. Here, the optimal averaging time, given by the minimum of the Allan deviation, was at 0.67 seconds, corresponding to frequency of 1.49 Hz. The fractional stability remains at 3×10^{-14} until 100 mHz, at which point Rayleigh scattering begins to dominate.

In Chapter 10 we use this interferometer setup to investigate how digitally enhanced homodyne interferometry may be used to modify the coupling of Rayleigh scattering. We then proceed in Chapter 11 to combine the interferometer readout with an optical frequency comb for characterisation of temperature effects in the sub 10 mHz frequency regime.

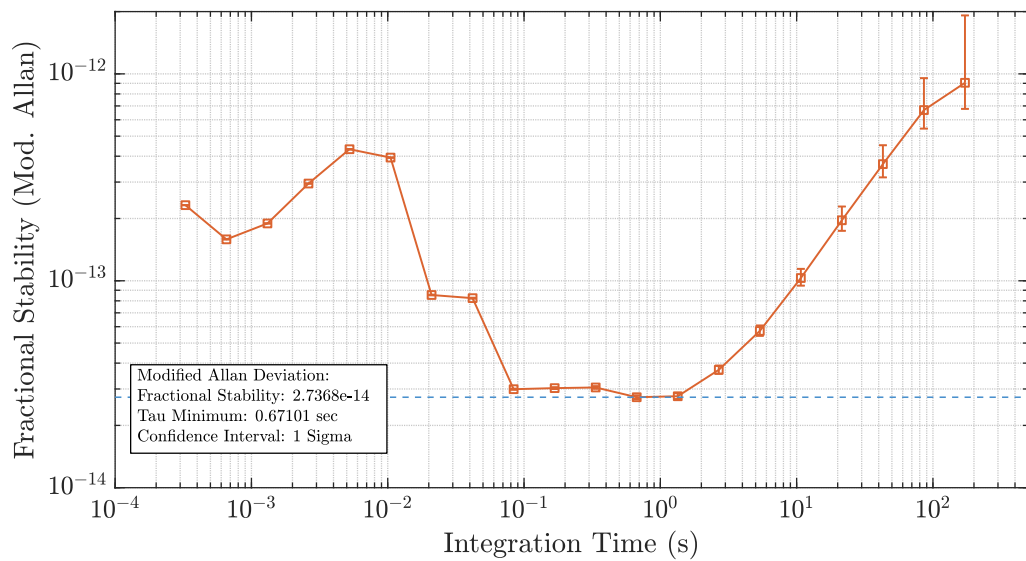


Figure 9.9: The modified Allan deviation computed using Stable32 for the dataset shown in Figure 9.7. We see an minimum fractional frequency stability of 2.7×10^{-14} at 1.49 Hz, indicated by the dashed blue line. This gives an optimal averaging time of 0.67 seconds. A level of 3×10^{-14} is achieved broadly from 1.5 Hz through to 100 mHz.

Gating of Rayleigh Backscatter Induced Phase Noise

Scattering in optical fibre is a double edged sword; both a useful measurand to be harnessed to measure external signals, and a spurious noise source which can degrade the performance of optical systems. For a fibre optic frequency reference, the latter case applies as the presence of Rayleigh scattering corrupts the interferometric readout, limiting the phase sensitivity of the interferometer. In this chapter, we discuss the coupling of Rayleigh scattering into the fibre frequency reference as well as the use of digital interferometry to gate and suppress Rayleigh scattering, thereby improving system noise performance.

10.1 Scattering in Optical Fibres

When light is scattered off material inhomogeneities, the scattering mechanism is determined by the relative size between the optical wavelength and the scattering features. In the regime where the scattering objects are smaller than the optical wavelength, Rayleigh scattering becomes the dominant scattering mechanism.

Here, we primarily consider the scattering off microscopic inhomogeneities and density variations within optical fibre; a function of the fibre manufacturing process, where the heat and stress of the drawing leads to these variations being embedded and ‘frozen’ into the material[105, 106]. The amount of Rayleigh scattering can be quantified through the scattering coefficient, as determined using the Einstein-Smoluchowski equation:

$$\alpha_S = \frac{8\pi^3 n^8 p^2 \beta k_B T_f}{3\lambda^4}$$

Where n is the refractive index of the glass, p the photoelastic coefficient of glass, β the isothermal compressibility and T_f the fictive temperature, which can be defined in terms of the temperature at which the glass was treated during the drawing process.

In modern optical fibre, especially at the telecommunication wavelengths around 1550 nm, modelling work by Saito et al has determined that Rayleigh scattering forms the dominant loss[105]. The theoretical limit of this loss, as postulated by the same work, is approximately 0.15 dB/km, though in practice, this value resides at 0.18 dB/km for

Corning SMF28e single mode fibre, which is the value we carry forward into the following calculations[106, 107]¹.

10.2 Backscatter Induced Phase Noise

The primary effect of Rayleigh scattering in the fibre reference is the introduction of phase errors in the mHz band. This is caused by the interference between the interferometer metrology optical fields and a coherent scattering field. As the phase noise of the scattering field increases, the interference between these fields leads to a flat noise shelf at lower frequencies. This is a known problem in gravitational wave detection, and has been extensively analysed in the case of a single point, or few scatter point sources[108, 109, 110, 111].

In order to adapt this analysis for Rayleigh scattering in a fibre optic interferometer, we replace the point-scattering field with the coherent Rayleigh back-scattered (RBS) field. This is similar to an analysis by Takada, which considers the phase coupling of Rayleigh scattering from a broadband light source within a Sagnac interferometer[112]. Here we extend this to consider a highly coherent source interrogating an unbalanced interferometer, focusing specifically at < 1 Hz Fourier frequencies. To start, we consider a single metrology field, for example a single interferometer arm, and the cumulative coherent RBS field generated from the fibre being interrogated. We can write this as follows:

$$E(t) = \underbrace{\left(|r_i|^2 P_i(t) e^{-2\alpha L_i}\right)^{\frac{1}{2}} e^{i\omega t + i\phi_i(t)}}_{i^{\text{'}}\text{th metrology field}} + \underbrace{\left(\gamma(L_C) P_i(t) e^{-2\alpha L_i}\right)^{\frac{1}{2}} e^{i\omega t + i\phi_i(t) + i\theta(t)}}_{\text{Scatter field}} \quad (10.1)$$

where $P_i(t)$ is the input optical power of which $|r_i|^2$ is the fraction contributing to the $i^{\text{'}}\text{th}$ metrology field. This input power also sees fibre attenuation, dependent on the attenuation coefficient, α and the length of the $i^{\text{'}}\text{th}$ interferometer arm, L_i . The fraction of the optical power that is coherently Rayleigh back-captured by the fibre is given by $\gamma(L_C)$ and is dependent on the optical coherence length L_C . The phase accrued by the metrology field is given by $\phi_i(t)$ with the phase of the integrated RBS field with respect to the metrology field given by $\theta(t)$. The square root factor in Equation 10.1 is due to the conversion between optical power and optical field.

A phasor representation of Equation 10.1 is shown in Figure 10.1. Before proceeding, we should note that given the metrology field is brighter than the scattering field, it is only the coherently amplified scattering which contributes significantly to the measured phase noise. For this reason, we discard effects of incoherent scattering.

Determining the RBS Phasor Amplitude

The next step is to estimate the mean RBS phasor amplitude, $(\gamma(L_C) P_i(t) e^{-2\alpha L_i})^{\frac{1}{2}}$, for which the term of interest is the coupling factor, $\gamma(L_C)$. This component of the analysis draws on work initially done by Gysel and continued by Fleyer[113, 114]. Using this work,

¹Note the conversion from dB scale to linear scale can be approximated by $\alpha = \alpha_{dB} \frac{\log(10)}{10}$ where α is defined in terms of optical power

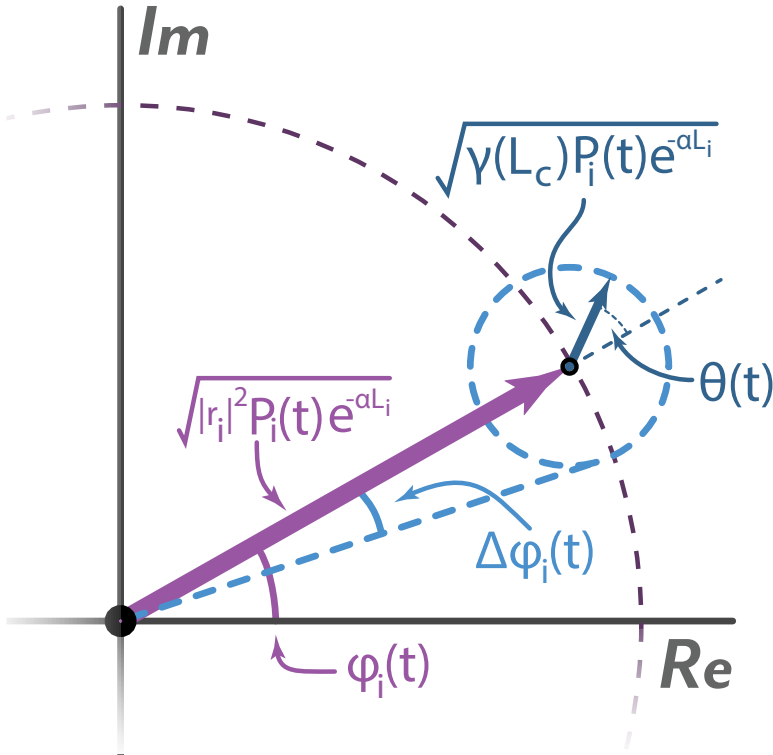


Figure 10.1: Rayleigh backscattering introduces a cyclic phase error, and can be depicted as a rotating phasor on top of the metrology phasor. The mean amplitude of the cyclic phasor is directly proportional to the Rayleigh backscattered field amplitude. The phasor dynamics, relative to the metrology phasor, are driven by laser frequency noise, and leads to a non-linear up-conversion as the rotation exceeds 2π radians within the measurement sampling period. $\phi(t)$ is the angle of the metrology field, $\Delta\phi_i(t)$ is the angular deviation caused by the RBS field, which in this Figure is shown to be maximum. We can determine this deviation using $\theta(t)$, the angle of the RBS field with respect to the metrology field

we determine the expectation value of the coherently backscattered power from a section of the optical fibre:

$$\langle \gamma(L_C) \rangle = \alpha_S \mathcal{S} \int_0^{L_C} e^{-2\alpha z} dz \quad (10.2)$$

Where $\langle \gamma(L_C) \rangle$ is the expectation value of the back-scattered power, normalised to the optical power at the start of the scattering location (L_i)². The other key parameters are the attenuation and scattering coefficients of the optical fibre, α and α_S respectively and the backscattering recapture coefficient, \mathcal{S} . Equation 10.2 then computes the loss over the coherence length, L_C , of which the backcaptured component is given by $\alpha_S \mathcal{S}$. This represents total integrated RBS power that is coherent with the metrology field.

As we operate at 1550 nm using SMF28e optical fiber, optical scattering is the dominant source of attenuation. Therefore the attenuation coefficient α is approximately equal

²In the simpler case where the coherence length is longer than the fibre length, the start point is the beginning of the fibre under test, and the optical power is the input power.

to the scattering coefficient, α_S . Making this substitution and computing integration we arrive at the following expression for the coherently backscattered power:

$$\langle \gamma(L_C) \rangle = \frac{\mathcal{S} (1 - e^{-2\alpha L_C})}{2} \quad (10.3)$$

The attenuation coefficient for SMF28e optical fibre is well known, and we take it to be 0.18 dB/km[107]. The scattering recapture coefficient, \mathcal{S} is given by the following expression[115]:

$$\mathcal{S} = \frac{3}{2(w_0/a)^2 V^2} \left(\frac{n_c^2 - n_{cl}^2}{n_c^2} \right) \approx \frac{1}{4} \frac{(NA)^2}{n_e^2}$$

where n_c is the fibre core refractive index, and n_{cl} is the cladding refractive index. The normalised spot size is given by w_0/a which is dependent on the normalised frequency parameter V for the fibre. For single mode optical fibres, we can approximate this using the known numerical aperture of the optical fibre (NA) and the effective index n_e [107, 115]. With this, we have all the necessary parameters to calculate the RBS phasor amplitude.

Phase Noise Coupling

The final step of this calculation is to determine the phase noise coupling given the amount of coherently Rayleigh scattered power. As highlighted in Figure 10.1, the phase noise coupling from RBS depends on the projection of the RBS phasor onto the phase quadrature of the metrology field phasor. This projection for the i 'th metrology field is given by the following expression:

$$\Delta\phi_i = \tan^{-1} \left(\frac{\|\text{RBS Phasor}\| \sin(\theta(t))}{\|\text{Metrology Phasor}\|} \right) \quad (10.4)$$

Where $\|x\|$ constitutes the amplitude of the phasor, x and $\sin(\theta(t))$ determines the projection of the RBS phasor to the interferometer phase $\Delta\phi$ as a function of time. Substituting in the expressions for both phasor amplitudes we arrive at the following phase noise coupling expression:

$$\Delta\phi_i = \tan^{-1} \left(\frac{(\gamma(L_C) P_i(t) e^{-2\alpha L_i})^{\frac{1}{2}} \sin(\theta(t))}{(|r_i|^2 P_i(t) e^{-2\alpha L_i})^{\frac{1}{2}}} \right) \quad (10.5)$$

We can now substitute the expression for $\gamma(L_C)$ from Equation 10.3. Given the scattering recapture coefficient is small, we can also use the small angle approximation to simplify the previous expression arriving at Equation 10.6.

$$\Delta\phi_i \simeq \sqrt{\frac{\gamma(L_C)}{|r_i|^2}} \sin(\theta(t)) = \sqrt{\frac{\mathcal{S} (1 - e^{-2\alpha L_C})}{2|r_i|^2}} \sin(\theta(t)) \quad (10.6)$$

From this, we note that the phase noise coupling is independent of the input power to the interferometer, as well as the length of each interferometer arm (L_i). We can physically reason this to both the metrology field, and its coherent RBS being attenuated over the same transit distance.

We also see the RBS induced phase noise is bounded due to the limits of the sine function in Equation 10.6. The spectral characteristics of the Rayleigh scattered noise is therefore determined by the Fourier transform of $\sin(\theta(t))$. As the phase noise $\theta(t)$ exceeds one cycle, it wraps around 2π , as illustrated in Figure 10.1. In this situation, instead of an increase to the amount of phase noise, the process up-converts the noise to higher harmonics. As the noise source we consider is a continuous spectrum, this results in the noise shelf commonly associated with non-linear scattering phase noise up-conversion, often referred to as “cyclic error” [111].

From existing work on fibre refractometry, we know the dynamics of $\theta(t)$ are primarily driven by laser frequency noise [113, 114], which for metrology grade lasers scales as $1/f$ at low frequencies[116]. At a threshold frequency, the $1/f$ laser frequency noise dynamics will cause $\theta(t)$ to exceed 2π resulting in up-conversion of this excess low frequency noise. In this limit, we can replace the function $\sin(\theta(t))$ in Equation 10.6 with its RMS value of $1/\sqrt{2}$ and assume the dynamics at these Fourier frequencies to be spectrally white. The phase noise spectral density due to the i 'th metrology field given these conditions can therefore be written as follows:

$$\tilde{S}_{\phi(i)} = \sqrt{\frac{\mathcal{S}(1 - e^{-2\alpha L_C})}{4|r_i|^2}} \quad (10.7)$$

For an unbalanced two beam interferometer such as the fibre frequency reference, the amplitude of the two metrology fields is vastly different, and need to be treated separately. If we consider the in-line optical architecture (for details see Chapter 9, Figure 9.1), the prompt reference reflection was caused by an glass/air/glass interface created by partially connecting two FC fibre connectors. This has a reflectivity of approximately $|r_{\text{ref}}|^2 = 0.08$, meaning only 8% of the total optical power at that point is utilised by the metrology field while the RBS field is dependent on the total power at that point. The signal arm of the interferometer has a HR fibre coupled mirror, therefore we consider $|r_{\text{sig}}|^2 = 1$. To determine the total RBS induced phase noise, we must incoherently add the contributions from these two metrology fields:

$$\begin{aligned} \tilde{S}_\phi &= \sqrt{\tilde{S}_{\phi(\text{ref})}^2 + \tilde{S}_{\phi(\text{sig})}^2} \\ \tilde{S}_\phi &= \sqrt{\frac{\mathcal{S}(1 - e^{-2\alpha L_C})(1 + |r_{\text{ref}}|^2)}{4|r_{\text{ref}}|^2}} \end{aligned}$$

This gives an expression for a single interferometer, however when we consider the differential stability measurement, we gain a factor of $\sqrt{2}$ as the Rayleigh scattering from each interferometer adds incoherently. This gives a total phase noise spectral density for the differential phase measurement as follows:

$$\tilde{S}_\phi = \sqrt{\frac{\mathcal{S}(1 - e^{-2\alpha L_C})(1 + |r_{\text{ref}}|^2)}{2|r_{\text{ref}}|^2}} \quad (10.8)$$

We then convert from phase spectral density to expected frequency noise, using the FSR of the fibre interferometer, yielding the following expression:

$$\tilde{S}_\nu(f) = \frac{c}{4n_e\pi\Delta L} \sqrt{\frac{\mathcal{S}(1 - e^{-2\alpha L_C})(1 + |r_{\text{ref}}|^2)}{2|r_{\text{ref}}|^2}} \quad (10.9)$$

Here ΔL is the physical fibre spool length of each interferometer. Using Equation 10.9, we can estimate the coupling of Rayleigh scattering into the fibre frequency reference differential stability measurement.

Gated Suppression of Backscatter Phase Noise

When we include a digital interferometric readout, such as the one used for the fibre frequency reference, we can digitally control the coherence of the optical source. For a given coherence length, we can then alter the amount of coherent Rayleigh scattering that will couple into the measurement as phase noise, as illustrated in Figure 10.2.

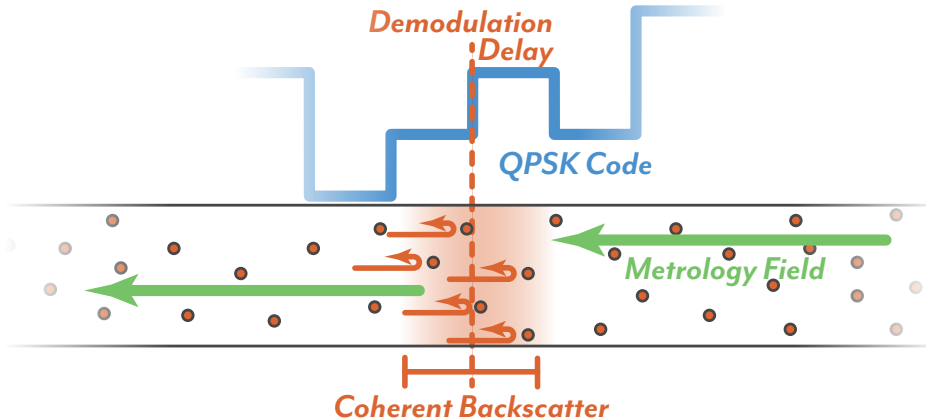


Figure 10.2: The use of digital interferometry allows for the gating of coherent backscatter. Digital interferometric modulation limits the coherence length of the source to an integrated region of 1 chip length around the demodulation point. Rayleigh backscatter within the optical fibre is therefore only coherent with the metrology field when the scattering event occurs within this gated region around the demodulation delay.

As per previous discussions, Digital interferometry enables gating of signals, with a resolution dependent on the modulation frequency of the pseudo random code. This chip length is analogous to the coherence length of the source, as all signals originating within one chip length interfere coherently³. We can therefore write the coherence length, as determined by digital interferometry, through the following expression:

$$L_c = \frac{c}{n_e f_{\text{chip}}}$$

Where n_e is the effective refractive index of the optical fibre, and f_{chip} the modulation frequency of the PRN or QPSK code. Substituting this into the expression for Rayleigh scattering induced phase noise, Equation 10.9, we can plot the expected RBS noise floor

³Assume the use of a coherent optical source with coherence length greatly exceeding the DI chip length

as a function of the code modulation frequency, f_{chip} , as shown in the following section in Figure 10.4.

10.3 Experimental Demonstration

Using the fibre frequency reference, as described in Chapter 9, we can measure the gating of Rayleigh scattering as indicated by a drop in the RBS noise shelf in the frequency domain. The main parameter which we alter is the coherence length of the source, which we can synthesise and modify by altering the modulation (chip) frequency of the DEHoI modulation. This process is not continuous, and therefore the method employed was to select a set of modulation frequencies, and conducting an interferometer differential measurement at each frequency.

The initial measurements, up to a chip frequency of 2 MHz, were conducted using the 40 MHz IntraAction AOM as the modulator. Due to the bandwidth limitations of this modulator, the faster rise time 200 MHz Gooch & Housego AOM was utilised for the measurements faster than a chip frequency of 2 MHz. A table of the modulation frequencies used and the measured and predicted RBS induced phase noise is shown in Table 10.1.

Chip Frequency (MHz)	Coherence Length (m)	RBS Noise Level (Hz/ $\sqrt{\text{Hz}}$)
0.05	4109.6	139.6
0.1	2054.8	107.7
1.04	197.3	61.7
1.98	103.6	44.1 (45.1)
2.5	82.2	49.0
5	41.1	44.5
13.8	14.8	37.9
25	8.2	13.2
41.7	4.9	10.0

Table 10.1: A list of the selected chip frequencies, respective coherence lengths and the measured Rayleigh backscattered phase noise level. The level was determined by fitting to the plateau in the measured frequency spectral density between 10 mHz and 100 mHz, as indicated in Figure 10.3. The results are plotted against the modelled phase noise level in Figure 10.4. The bracketed value for 1.98 MHz chip frequency represents the measurement with the G& H AOM at that frequency.

Following the completion of the series of DEHoI modulation frequencies, we determine the RBS phase noise coupling for each measurement. The magnitude of the RBS noise feature was measured by taking the average of the spectral density between 10 mHz and 100 mHz; the frequency band which corresponds with the RBS induced phase noise shelf. The uncertainty is determined by computing the standard deviation of the frequency data within the same measurement band. The frequency band of interest, and the measurements we obtain from the spectral density are highlighted in Figure 10.3, a representative example at a chip frequency of 1.98 MHz. The resultant RBS phase noise induced frequency noise from all measurements are listed in Table 10.1 and plotted as a function of the DEHoI modulation frequency in Figure 10.4. In addition, Figure 10.4 also plots the theoretically expected frequency noise from Equation 10.9, which we see is dominated by RBS coupling from the reference reflection.

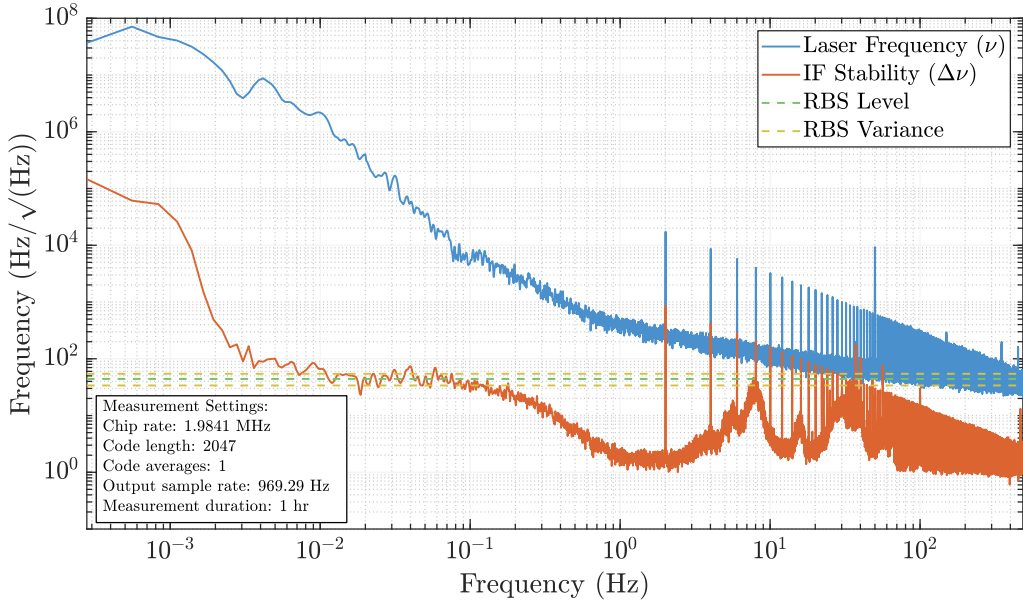


Figure 10.3: A frequency spectral density showing the Orbita Lightwave laser frequency noise spectrum as measured using a fibre frequency reference. The subtraction (IF Stability), shows the relative frequency stability between the two fibre interferometers. The Rayleigh backscattering noise shelf magnitude we see rolls up to a clamping point by ~ 100 mHz and was estimated by fitting to the spectral density plot. The fit, given by the RBS level and uncertainty, given by the RBS variance were computed by considering frequency data between 10 and 100 mHz. The example plotted here is a measurement at $f_{\text{chip}} = 1.98$ MHz using the low speed IntraAction AOM.

The highest modulation frequency accessible with the 200 MHz Gooch & Housego AOM was $f_{\text{chip}} = 41$ MHz. As plotted in Figure 10.4 we see this achieves an RBS noise limited frequency noise of $10 \text{ Hz}/\sqrt{\text{Hz}}$, which shows good agreement with the noise floor estimate at that modulation frequency. We see broad agreement between the experimental data and the theoretical model above 1 MHz chip frequencies, with the main deviation from the trend occurring at a modulation frequency of 13.8 MHz. While within the uncertainty bounds, we hypothesize the deviation is due to residual code noise arising from an unfavourable combination of DEHoI measurement bandwidth and modulation frequency. These details of code noise have been discussed in prior work [96], with current investigations into methods to confirm as well as further minimize its effects carried out by fellow PhD student, Ya Zhang.

For low chip frequencies, we see in Figure 10.4 that the experimental results appear below the noise floor estimate. To explain this, we consider the dominant RBS noise source, the reference arm of the interferometer. Due to its position at the start of the interferometer, the amount of RBS coherent with the reference arm is restricted by the lead fibre length. Therefore, we expect as the amount of RBS from the reference arm to clamp even while the coherence length continues to increase. This in turn leads to the lower than expected RBS coupling at low chip frequencies in Figure 10.4.

From this work, we can use the RBS noise estimate to determine the requirements to suppress the low frequency noise shelf to $1 \text{ Hz}/\sqrt{\text{Hz}}$. Following the trend set by the

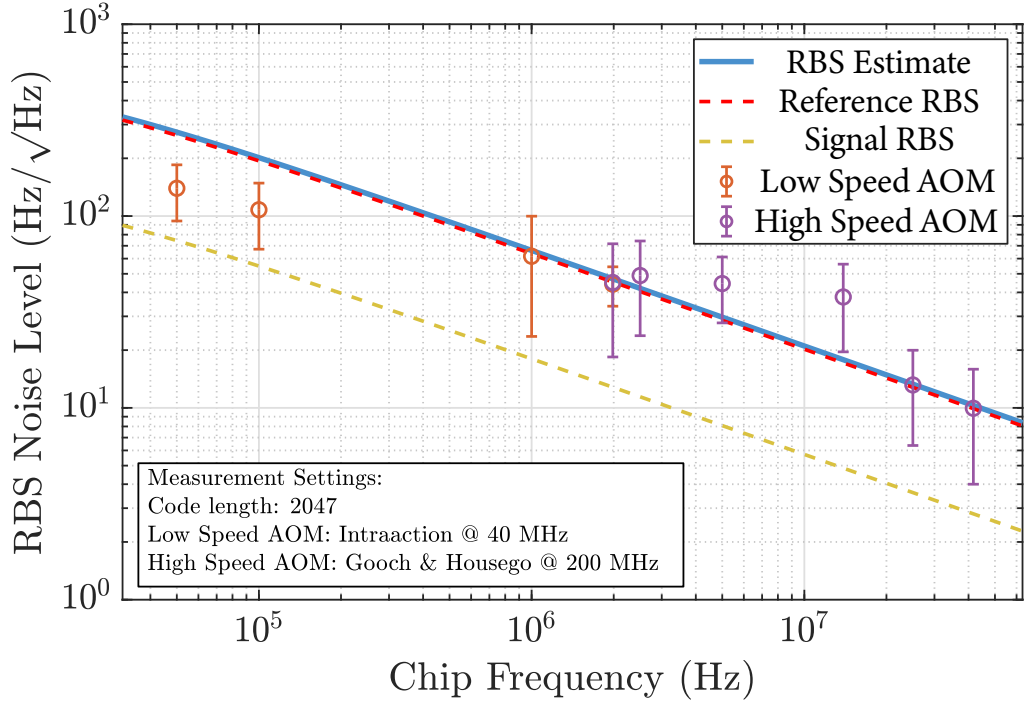


Figure 10.4: A comparison of estimated and measured phase noise from Rayleigh backscattering for the fibre reference. We measure the RBS noise floor using two different modulators over different modulation frequency regimes. The data sets are overlapped at a modulation frequency of 1.98 MHz which shows good agreement between the results obtained with the two modulators. We see broad agreement between the RBS noise estimate and the experimental data as measured over the 10 to 100 mHz Fourier frequency band. This achieves a minimum noise floor of $10 \text{ Hz}/\sqrt{\text{Hz}}$ using the fastest accessible DEHoI modulation frequency of 41 MHz. At low modulation frequencies, we estimate the RBS coupling on the reference field to decrease, explaining the experimental results at 50 kHz and 100 kHz appearing below the RBS estimate.

model, we estimate a 3.7 GHz modulation frequency is required to achieve $1 \text{ Hz}/\sqrt{\text{Hz}}$ across the RBS noise shelf from 10 mHz to 100 mHz. While this is technically feasible for both modulators and digital signal processing hardware, the expected improvement to the noise floor does not match the considerable cost of hardware and engineering effort required to implement this approach.

From Equation 10.9 we see that the RBS frequency noise is inversely proportional to ΔL . Hence, as an alternative to an increase in modulation frequency, an increase of the fibre interferometer length by a factor of 10 using a 40 km fibre spool would result in a predicted RBS limited frequency noise floor of $1 \text{ Hz}/\sqrt{\text{Hz}}$. Once extended to such long lengths of fibre, the effects of attenuation and the optical power necessary to overcome that become increasingly important considerations. Therefore, to avoid these complications, we conclude the most prudent course of action for future designs is to implement a transmissive interferometer, such as a Mach Zehnder, which will be immune to first order Rayleigh scattering. The insight we draw from this work can then be readily applied to second order scattering effects, which will present a technical limit for this new architecture.

Infrasonic Performance of a Fibre Frequency Reference

A major technical challenge with an optical fibre interferometer is the coupling of low frequency thermally induced drift. The drift causes changes to the physical length of the fibre, as well as shifts of its effective refractive index. These changes amount to fluctuations in the optical path length of the interferometer, introducing phase noise in the sub millihertz band.

Meanwhile, optical frequency combs provide a means for optical sources to be referenced to RF frequency standards which are stable over significantly longer time scales. In this chapter, we combine frequency readouts from an optical frequency comb and fibre frequency reference. Through this, we verify the readout calibration of the fibre frequency reference and further characterise thermal effects on the fibre reference.

11.1 Optical Frequency Comb Wavelength Metrology

Optical frequency combs are a powerful tool for connecting the radio frequency and optical domains. Consisting of an array of equally spaced discrete optical frequencies, dubbed comb teeth, they act effectively as a ruler for measuring optical frequency. A self-referenced optical frequency comb is able to stabilise to RF frequency standards such as atomic clocks, inheriting the long timescale stability of these frequency standards. This frequency stability can be broadly disseminated through the optical regime via the comb enabling other optical sources to be referenced to it as a stable, calibrated frequency source. This development warranted the awarding of the Nobel Prize in Physics in 2005[117].

The optical frequency comb was originally developed as a tool for high resolution spectroscopy. The core frequency comb consists of a mode-locked laser, generating an ultra-fast pulse train with a fixed phase relationship between the successive pulses. If we consider the pulse train in the frequency domain, we generate a comb function, consisting of distinct peaks with an equidistant spectral spacing. The spacing of the teeth in the frequency domain is directly proportional to the pulse repetition rate, f_r of the mode-locked laser. We can write each successive comb tooth frequency in terms of the laser repetition rate:

$$\nu_i = n_i f_r + f_o$$

Where ν_i is the frequency of the i th comb tooth, n_i is an integer representing the tooth number, and f_o an offset frequency. As the repetition rate, f_r fluctuates, this causes an expansion or contraction of the frequency difference between all comb teeth, resulting in a stretch or contraction to the spectral output. The offset frequency, f_o on the other hand results in a common shift to all comb teeth. The frequency f_o is referred to as the Carrier Envelope Offset (CEO) frequency.

This name is apt as the CEO frequency is dependent on the carrier envelope phase, ϕ_{ce} . This is the time evolving phase of each successive pulse due to the difference between the phase and group velocities of the resonator field in the mode-locked laser[118], and can be written as follows:

$$\Delta\phi_{ce} = \left(\frac{1}{\nu_g} - \frac{1}{\nu_p} \right) l_c \omega_c$$

In this expression, ν_p and ν_g are the phase and group velocities respectively. The length of the optical resonator is given by l_c and the centre frequency of the pulse by ω_c . The presence of this phase offset leads to a common frequency shift in all the comb teeth as given by the following expression[118]:

$$f_o = \frac{f_r \Delta\phi_{ce}}{2\pi}$$

Given these two parameters, f_r and f_o , we are able to determine the absolute optical frequency of each of the comb teeth. However, both of these parameters are time varying, meaning that for any absolute frequency referencing, both these parameters must be stabilised.

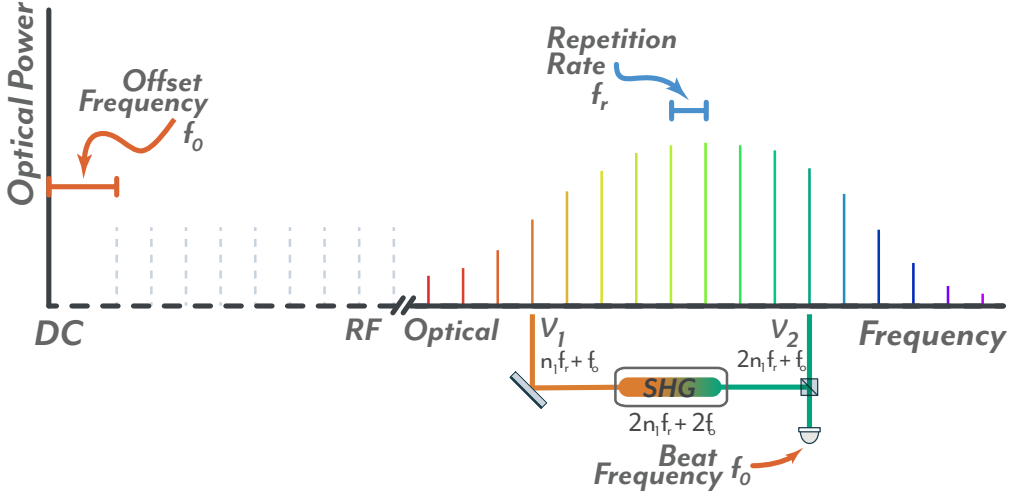


Figure 11.1: Stabilising a frequency comb requires referencing of two parameters, the repetition rate (f_r) and offset frequency (f_o) to a frequency standard. The repetition rate can be directly measured through a heterodyne measurement of two successive comb teeth and locked to an RF frequency standard. To lock the offset frequency, two comb teeth separated by an octave in optical frequency are used instead. By frequency doubling the lower comb tooth using second harmonic generation (SHG) and performing a heterodyne measurement with the upper tooth, the offset frequency can be isolated, and similarly referenced to an RF frequency standard.

In practice, the repetition rate (f_r) of an optical frequency comb is fairly routine to stabilise. As this frequency is typically within the bandwidth of RF electronics, the heterodyne beat note between successive comb teeth can be readily measured, demodulated and referenced back to an RF frequency standard. Feedback to control this frequency is sent to the laser resonator length, typically through piezo actuation. However, the application of optical frequency combs to wavelength metrology was only truly enabled when Hansch et al managed to stabilise the CEO frequency by producing the first self-referenced frequency comb.

In a self-referenced optical frequency comb, the CEO frequency can also be reduced to a RF frequency, which in turn can be referenced back to the same frequency standard as the repetition rate. This is achieved by spectrally broadening the comb, producing an octave spanning spectrum[119]. If we consider a tooth at the lower end of the comb with frequency ν_1 . An octave spanning comb has a tooth at the higher end with frequency ν_2 . We can set up the relationship between the two frequencies in terms of the repetition rate and the CEO frequency, also illustrated in Figure 11.1:

$$\nu_1 = n_1 f_r + f_o \quad \nu_2 = 2n_1 f_r + f_o$$

If we take the lower frequency, ν_1 and frequency double it through a second harmonic generation process, the resultant heterodyne beat frequency with ν_2 can be written as follows:

$$2\nu_1 - \nu_2 = 2(n_1 f_r + f_o) - (2n_1 f_r + f_o)$$

This beat frequency isolates the CEO frequency, which allows it to also be demodulated and referenced back to the same RF standard as the repetition rate. To scan and lock the CEO frequency, the intra-cavity phase is tuned. Options for this include varying the pump power, electro-optic actuation or wedge optics. In this way, the two parameters which determine the position of each comb tooth can be locked to an absolute frequency standard.

Given a fully locked optical frequency comb, a test optical source can now be interfered against its nearest neighbour comb tooth to measure its relative drift. The resulting RF frequency heterodyne beat note can similarly be demodulated and tracked giving a continuous readout of this drift.

11.2 Digital Phasemeter Implementation

A critical component of measuring the frequency difference between the comb tooth and a test laser is the readout of the heterodyne frequency. Ideally, this readout has a high sampling rate, and can be adjusted to synchronise with the fibre frequency reference readout. In order to fulfil these requirements, the tracking implementation we use is the digital phase locked loop (PLL). By implementing this frequency readout digitally, we can readily deploy this readout on the same FPGA platform as the fibre frequency reference, as discussed in the next section.

At its core, a phase locked loop performs an IQ demodulation of an RF tone, mixing it down to DC. The difference between this and the IQ demodulation discussed in Chapter 3 is the continuous feedback to update the mixdown frequency, as shown in Figure 11.2. By closing the loop, the phase difference between the input RF frequency and the mixdown frequency is continuously zeroed, resulting in a maximum projection in the I quadrature, with the residual projection in the Q quadrature due to out of bandwidth noise.

Key to this specific implementation however is the continuous tracking of the input RF frequency by the mixdown frequency. By reading out the mixdown frequency as a function of time, we can then infer the RF frequency, and therefore the heterodyne beat frequency between the test laser and frequency comb.

The FPGA algorithm used for this PLL was modified based on the extensive digital PLL work carried out by Roberts [8], and the comb specific implementation was developed with Sarre [120] for an undergraduate project. In adapting the PLL for the readout of the frequency comb beat note, we had to address two issues. Firstly, the linewidth of the comb teeth are dependent on the stability of the clock to which it is referenced. In the system used in the following experiments, a Rubidium atomic reference¹ is used, and a key limitation of these atomic references is the short term stability. As a result, the linewidth of each individual tooth is on the order of 100 kHz. This far exceeds the linewidth of the test laser, and as such dominates the width of the heterodyne beat note. Therefore, we require the unity gain bandwidth of the PLL control loop to be in excess of 100 kHz to maintain lock on the broad lineshape.

Secondly, the original implementation by Roberts was optimised for a FPGA clock frequency of 40 MHz. As the fibre frequency reference runs at a clock speed of 125 MHz, many of the operations need to be parallelised or pipelined in order to prevent timing errors and ensure all computations are completed within the clock cycle.

Running the PLL at 125 MHz clock frequency enforces a limit on the dynamic range of the frequency readout. Specifically, if the heterodyne beat frequency exceeds the Nyquist frequency of 62.5 MHz, the readout will lose lock. In practice, we aim to keep the beat frequency below 50 MHz, which can be achieved by periodically tuning the repetition rate of the frequency comb, changing the spectral position of the comb teeth. In this way, we can maintain the beat frequency range without having to modulate the test laser.

¹SRS FS725 Rubidium Frequency Standard

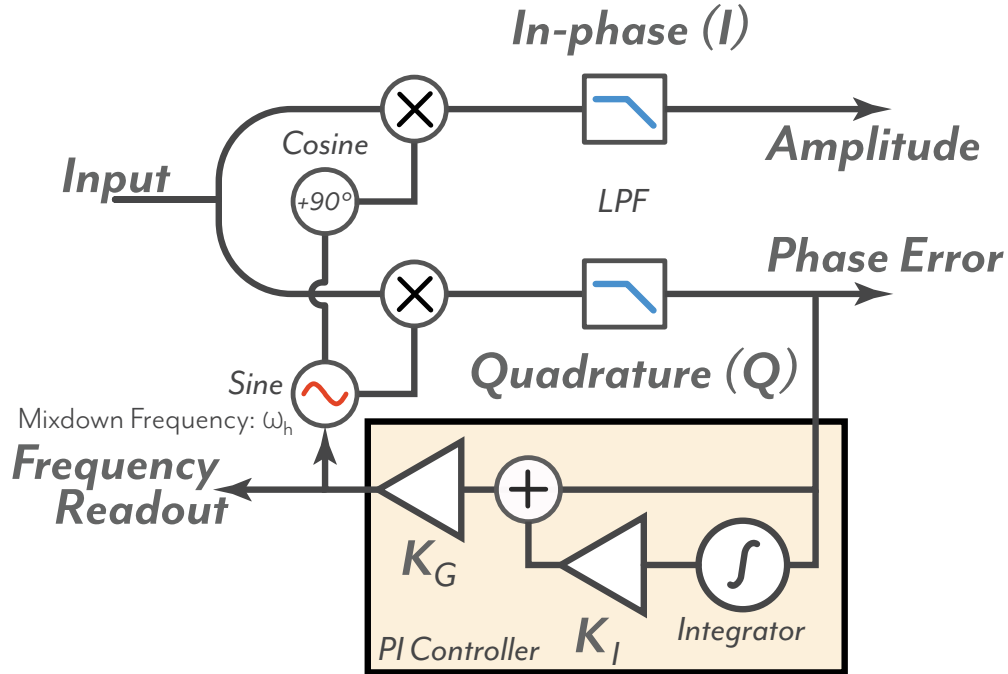


Figure 11.2: A phase lock loop takes an input RF tone and mixes down to DC using phase locked sine and cosine functions and low pass filters (LPF). The phase lock is maintained by locking the quadrature readout to zero using a PI controller, the bandwidth of which can be tuned using the proportional (K_G) and integral (K_I) gain parameters. When locked this projects the output phasor to the in-phase axis. Therefore, the in-phase readout measures the amplitude of the input tone. Furthermore, under this condition, the PLL ensures the mixdown frequency is matched to the input, providing a continual tracked readout of the frequency and the residual quadrature readout provides a measure of the residual phase error.

Following the speed and locking bandwidth optimisation, we obtained a stable PLL with a 300 kHz unity gain frequency. In order to verify the performance of the frequency tracking, we implemented a measurement of the PLL transfer function to frequency excursions. The setup, as shown in Figure 11.3, interrogates the PLL with a single frequency tone generated using a numerically controlled oscillator (NCO) built on the same FPGA.

The frequency of the NCO generated tone is then modulated by an analog signal from the ADC input. The output from the PLL is the frequency error; the detuning from the initial PLL lock point. The frequency error output is sent through the DAC back into the analog domain. The loop between the ADC and DAC is closed using the Bode analyser instrument on the Moku:Lab. This generates a swept tone which drives the ADC and measures the amplitude and phase of the FPGA signal processing via the DAC output synchronously with the sweep frequency. As the ADC and DAC are greater than a factor of 2 faster than any other dynamics in the system, the transfer function is limited by the PLL. The measured transfer function is shown in Figure 11.4.

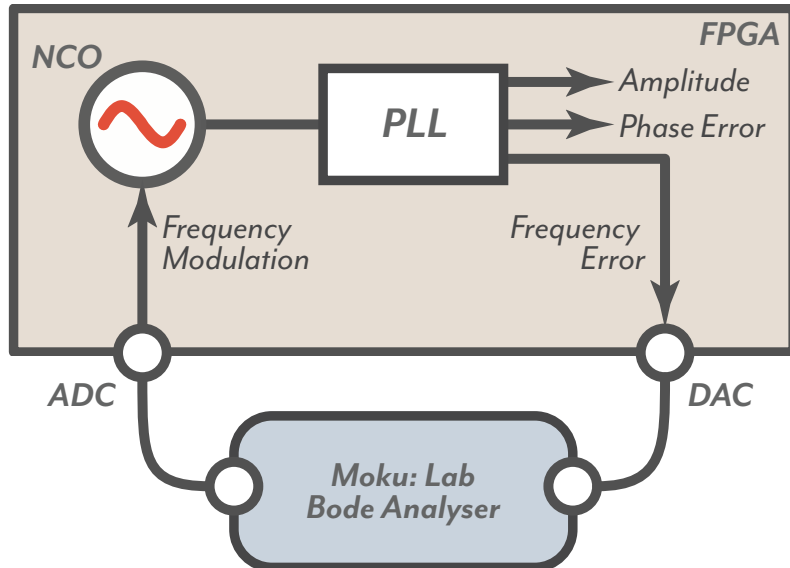


Figure 11.3: The transfer function of the phase locked loop (PLL) was measured by driving it with a frequency modulated input signal. The RF carrier was generated using a numerically controlled oscillator (NCO) on the FPGA, with the modulation signal being a swept sinusoid generated by the Moku:Lab Bode Analyser, and digitised using the FPGA’s ADC. The PLL was then locked to the RF carrier frequency and the tracked frequency modulation (frequency error) was output back to the Moku using the DAC.

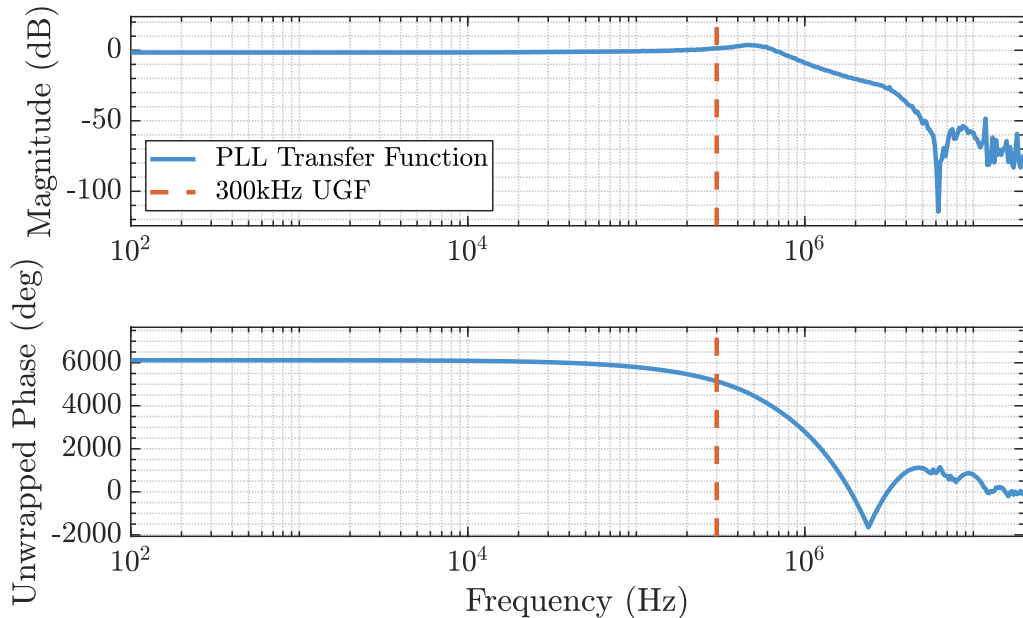


Figure 11.4: The measured amplitude and unwrapped phase response of the PLL to frequency modulation. We see a flat response up to the unity gain frequency of the PLL at 300 kHz. The bandwidth was found to be sufficient to continuously track the optical frequency comb output.

As we see from Figure 11.4, the PLL unity gain frequency reaches the intended 300 kHz bandwidth. This allows us to track the high speed dynamics of the broad comb teeth. The implementation and testing of the optical component of the readout is discussed in the following section.

11.3 Comb Referenced Laser Frequency Readout

In this experiment, an optical frequency comb centred at 1550 nm from Menlo Systems and referenced to a Stanford Research Rubidium clock is used to provide an external optical frequency measurement of the Orbita Lightwave test laser[121, 122]. In order to measure the relative difference between the comb and the test laser, we interfere the two optical sources, producing a heterodyne beat note at the difference frequency between the two. Tracking the frequency dynamics of the heterodyne beat note we are able to determine the wavelength drift of one source relative to the other.

The interferometer was constructed with an all fibre construction, the schematic for which is shown in Figure 11.5. The fibre coupled output of the comb was passed through a circulator with an 80% reflectivity fibre Bragg grating manufactured by Technica at the circulator output[123]. A fibre Bragg grating central wavelength was tuned around the test laser wavelength. As the comb repetition rate was 250 MHz, we required a spectral resolution of greater than 250 MHz to ensure that only 1 comb tooth was reflected by the grating.

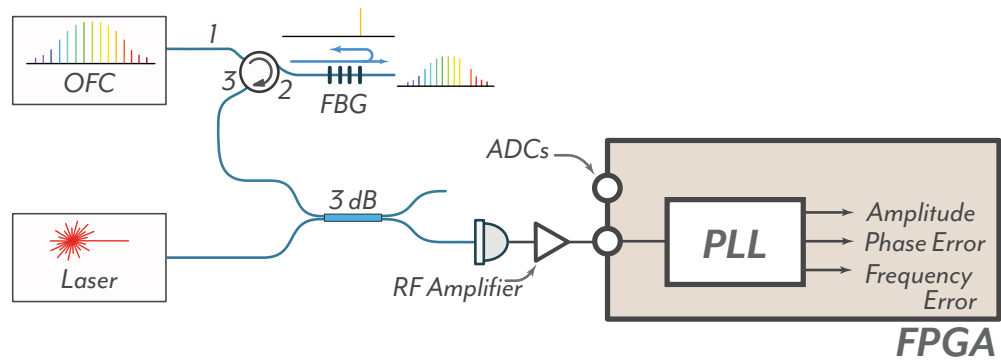


Figure 11.5: The experimental apparatus used to measure the frequency of the test laser using the optical frequency comb. The output of the comb was first conditioned using a fibre bragg grating with reflection wavelength matched to within 125 MHz of the laser frequency. The grating reflection therefore isolated a single comb tooth which was interfered with the test laser. The beat note was detected and passed through an RF amplification stage before digitisation. The frequency of the beat note was tracked using a digitally implemented PLL as discussed in the section prior.

The reflected comb tooth was selected using the reflection port of the circulator and interfered against the Orbita laser. Ensuring that only one comb tooth was interfering with the test laser removes any higher order heterodyne frequencies, improves shot noise performance and fringe visibility due to the absence of spurious comb teeth. As only the nearest comb tooth to the test laser is used, the heterodyne beat frequency is at maximum $f_r/2$, which corresponds to a frequency of 125 MHz. This is matched to the

photodetector bandwidth of 125 MHz for the NewFocus 1811 FC detector.

Following detection, the signal was AC coupled and conditioned by passing it through a Minicircuits RF amplifier to optimally match to the input voltage range of the ADCs on the NI 5782 FPGA interface card. We again use the NI 7966R FPGA to implement a digital phase-locked loop (PLL), as discussed in the previous section to track, and measure the beat frequency. As we are interested in relative stability, this metric is sufficient and the absolute frequency was not computed for this experiment.

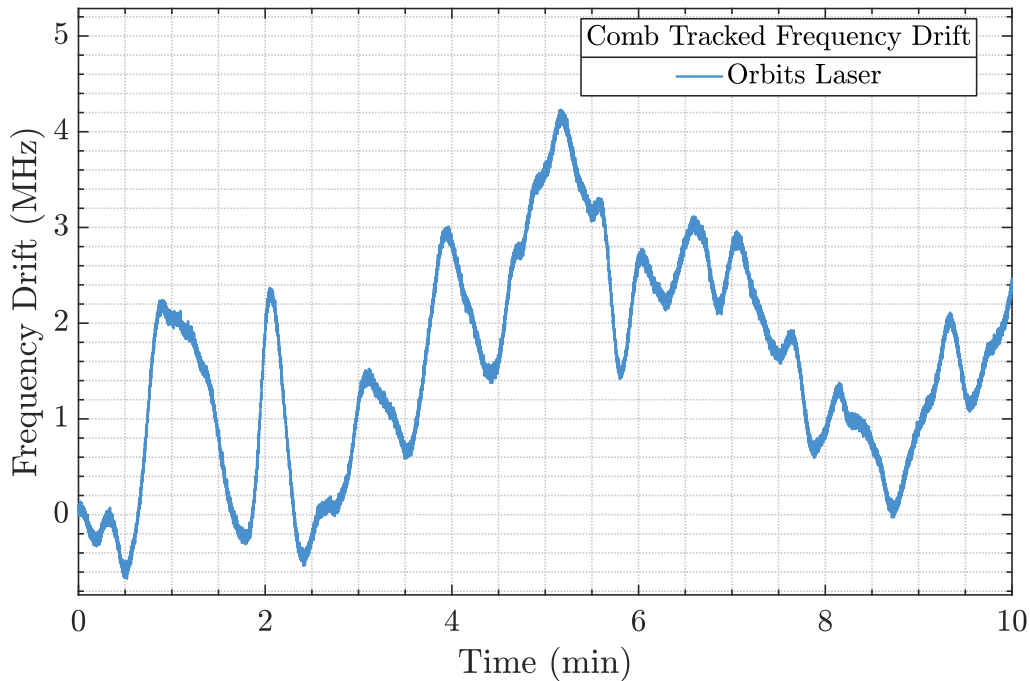


Figure 11.6: A 10 minute measurement demonstrating the drift of the Orbits Lightwave test laser with respect to the optical frequency comb. While the low frequency dynamics are dominated by laser drift, the width of the trace is due to the linewidth of the frequency comb.

As an initial test, we measure the frequency drift of the Orbits Lightwave test laser as shown in Figure 11.6 over the course of several minutes. The frequency drift on the order of MHz is successfully tracked however for sources with higher drift, active feedback would be required to maintain the RF beat between the comb and the source within the ADC bandwidth.

11.4 Hybrid Fibre-Comb Frequency Reference

In order to use the optical frequency comb (OFC) to characterise the fibre reference, we synchronously combine the measurement systems of the fibre frequency reference and the OFC into a ‘hybrid’ readout. Facilitating this is relatively straight-forward given the development up to this point of both measurement architectures on the NI 7966R FPGA platform. The high resource count of this FPGA means that both readout architectures can be readily implemented on the same physical processor. We however only have two ADC channels which means it is possible to only utilise a single fibre interferometer instead of both as was discussed in Chapter 9. This leads to the experimental setup as shown in Figure 11.7.

Figure 11.7 (a) is the conventional setup using two fibre interferometers discussed in Chapter 9 and 10, and is included here for comparison. In this setup we measure the laser frequency noise of the Orbit laser with respect to the two interferometers. In Figure 11.7 (b), we substitute the OFC for one of the fibre interferometers, as before measuring the laser frequency noise of the Orbit Lightwave laser. As the low frequency stability of the fibre interferometer is of particular interest in this experiment, we complete a 48 hour measurements in both configurations, giving us a frequency resolution of $5.7 \mu\text{Hz}$ in each measurement. When tracking the frequency comb, the PLL used for demodulation must remain locked and the RF beat between the Orbit and comb within bandwidth. To ensure this, the beat note was monitored remotely through an RF spectrum analyser.

On the fibre frequency reference side, the measurement bandwidth was reduced in order to ensure that file sizes did not exceed capacity of the available hard drives. The reduction of the output sample rate was done by increasing the number of code averages computed to 32. Using a 2 MHz chip frequency, an 11 bit code with 2047 elements, and 32 full code integrations, the output sample rate was reduced to 30.29 Hz. This was matched to the PLL output decimation filters insuring that both readouts were synchronous. The time domain picture of the measurement over the entire 48 hour time span is shown in Figure 11.8.

In Figure 11.8 (b), we plot the frequency difference between the two measurements, with the difference being zeroed at initialisation. We see that the smaller, hour time-scale features due to laser drift are common between measurements and removed through the two reference subtraction. The frequency difference is therefore limited by primarily the thermal expansion, and subsequent optical path length change of the optical fibre.

The main drawback of the frequency comb however is the short term stability. To illustrate the difference in short term stability, we can zoom in on the data presented in Figure 11.8. Comparing over the course of the first minute of the 48 hour measurement, we can compare the short term stability of the two references, shown in Figure 11.9. If we take the RMS noise of both measurements over a 1 second timespan, we find that the fibre frequency reference has an RMS noise level of 0.72 kHz while the frequency comb measurement over the same timespan amounts to 48.94 kHz of frequency noise, a factor of ~ 68 noisier.

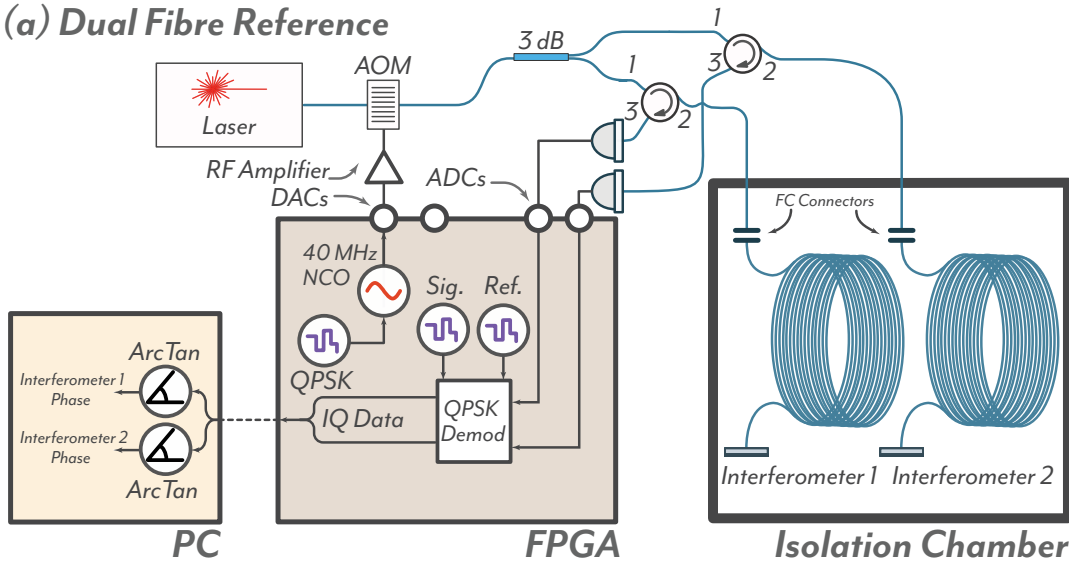
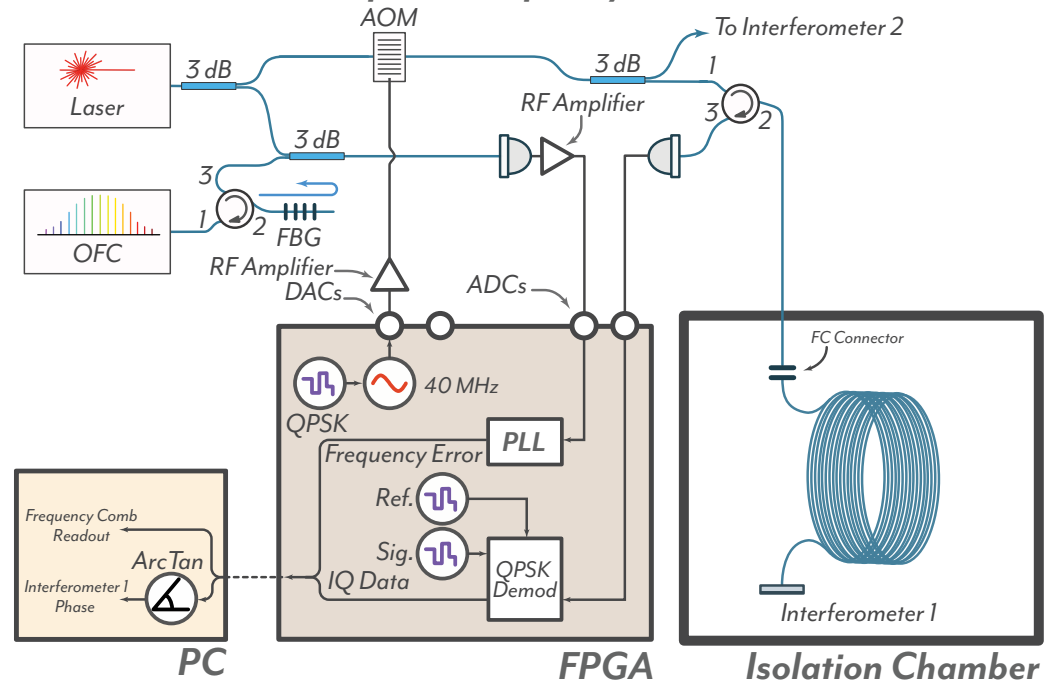
(a) Dual Fibre Reference**(b) Fibre Reference + Optical Frequency Comb**

Figure 11.7: The hybrid fibre-comb reference setup combines the fibre frequency reference and comb readouts with the Orbits Lightwave test laser split between the two references. Due to a limited number of ADCs, the reference must operate in either of two modes. a) Fibre interferometer 1 and fibre interferometer 2 both measure the Orbits laser frequency. The difference of these two measurements yields an estimate of the stability of each fibre interferometer independent of the Orbits Laser frequency noise. b) Fibre interferometer 1 and the optical frequency comb both measure the Orbits laser frequency. We use the difference of these two measurements to characterise the long term length stability of the fibre reference independent of the Orbits laser frequency noise.

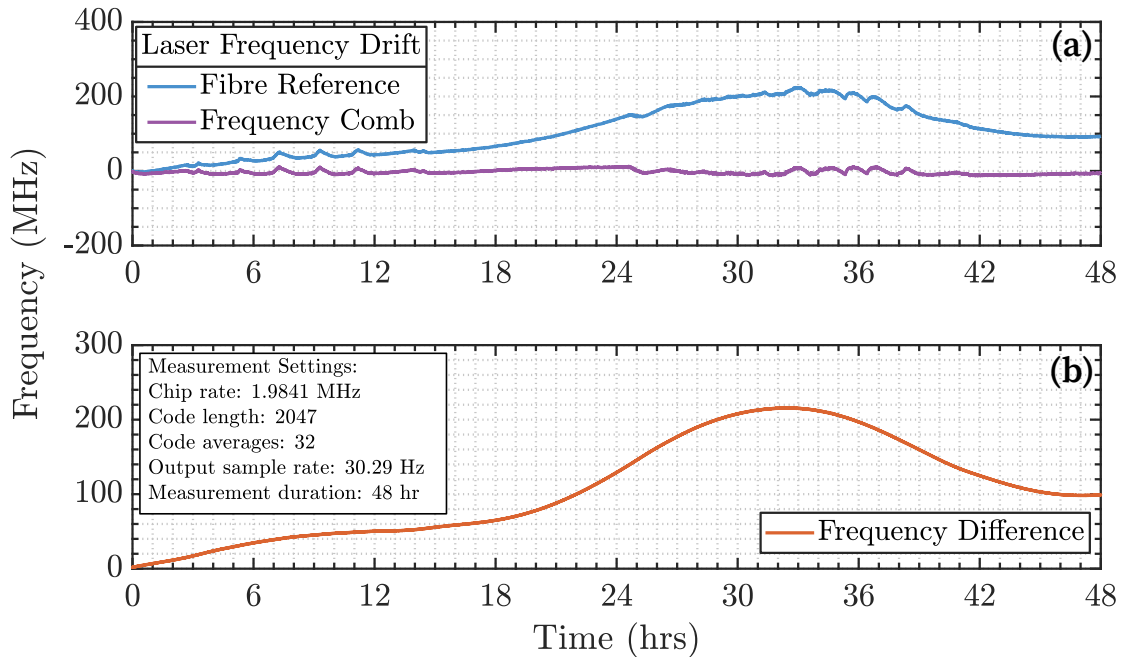


Figure 11.8: Time domain plot of the synchronised fibre frequency reference and the optical frequency comb readouts of the free-running Orbits laser (a). Short term dynamics on the scale of 1-2 hours are common to both readouts, illustrating the short timescale drift of the Orbits. These are subtracted in (b), which shows the frequency difference between the two readouts. The frequency difference is primarily driven by thermal expansion of the fibre reference, and reaches a maximum fluctuation of 200 MHz over the 48 hour measurement

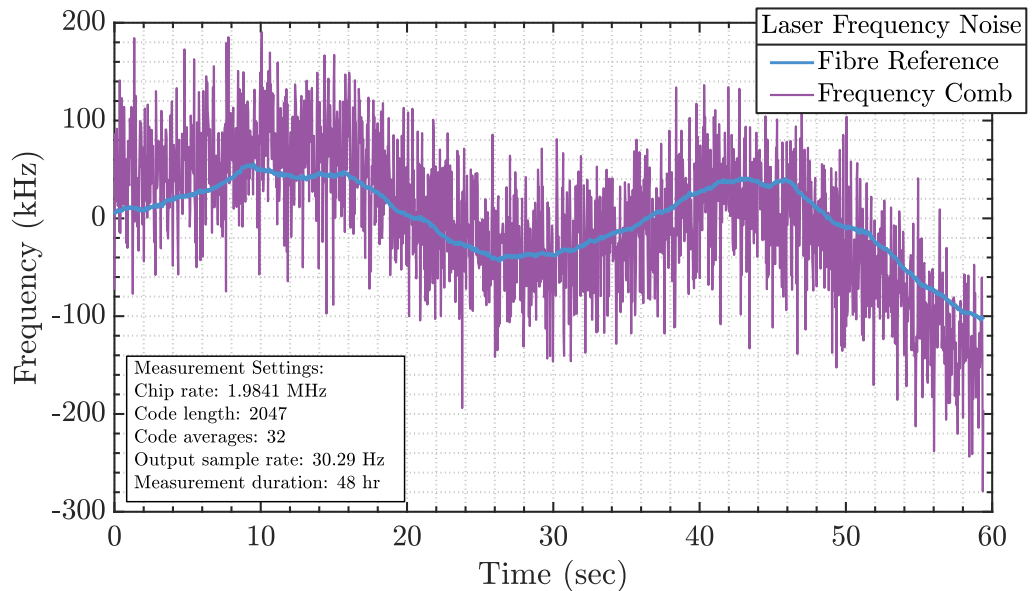


Figure 11.9: A zoomed time domain plot showing the first minute of the 48 hour hybrid-reference measurement (Figure 11.8 a). This illustrates the improved short term stability of the fibre frequency reference.

11.5 Determining the Thermal Corner Frequency

To continue on from a time domain noise comparison, we can further compute the amplitude spectral density of both measurements and compare against a differential measurement between two fibre interferometers. This measurement is again 48 hours in duration, however as it was not possible to operate setup a) and b) from Figure 11.7 simultaneously, the two interferometer measurement was done immediately after the 2 day interferometer-comb measurement.

These are plotted in Figure 11.10, showing the relative stability between the different references in the frequency domain. Here trace (a) is the spectral density of the Orbit Laser with respect to IF1 while trace (b) plots the Orbit laser with respect the OFC. Note that only data from IF1 is plotted as the spectrum from IF2 is identical on this scale. At frequencies below 100 mHz traces (a) and (b) overlap, indicating that in this low frequency regime, both reference measurements are dominated by the frequency dynamics of the Orbit laser.

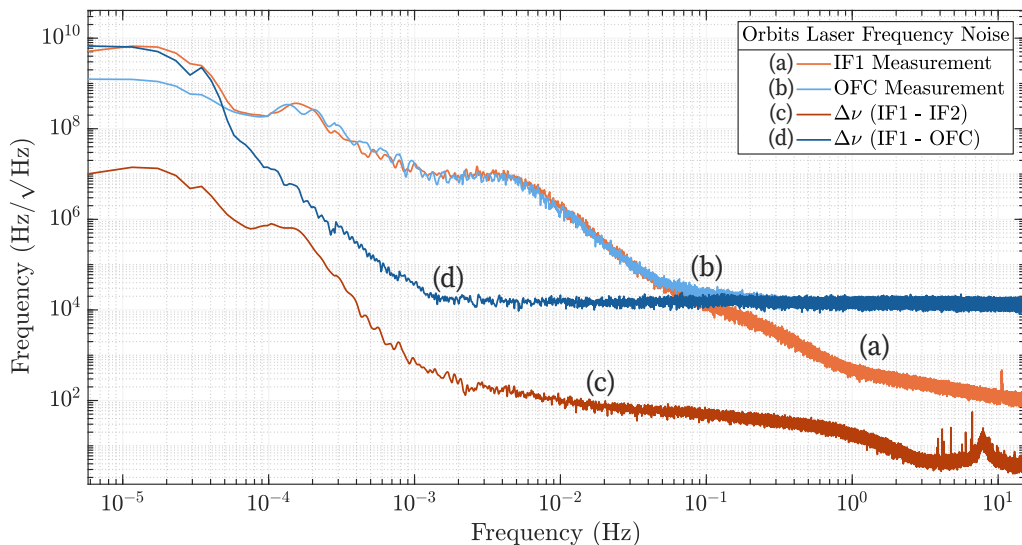


Figure 11.10: A comparison between the measured spectral densities showing the relative frequency stability between the two fiber references and the optical frequency comb. All measurements were conducted over a 48 hour time period. Trace (a) A single fiber frequency reference measuring the Orbit laser, trace (b) optical frequency comb readout measuring the Orbit laser, trace (c) the subtraction of two fiber frequency references and trace (d) the subtraction of fiber reference IF1 and the optical frequency comb. Note the DC frequency bin has been omitted for clarity.

Above 100 mHz, the traces diverge where (b) becomes dominated by the white frequency noise of the OFC at a level of around $20 \text{ kHz}/\sqrt{\text{Hz}}$, while trace (a) still measures the Orbit laser frequency noise. The remaining two traces plot the relative stability between interferometer 1 (IF1) and interferometer 2 (IF2); trace (c), and IF1 and the OFC; trace (d).

When comparing traces (b) and (d) in Figure 11.10, we see the difference between IF1 and the OFC; trace (d) removes common Orbit laser frequency noise dynamics between 100 mHz and 100 μHz . This reveals a thermally induced roll up corresponding with the

long timescale thermal expansion-contraction of the fibre interferometers which is visible for frequencies below 1 mHz. While this low frequency noise feature is also present in the two interferometer measurements; trace (c), it is suppressed by the common thermal environment of the interferometers and therefore underestimates the noise floor over thermal time scales.

This common thermal response of the fibre interferometers causes approximately one order of magnitude suppression below 1 mHz and increases further at very lower frequencies. We therefore rely on the difference between IF1 and the OFC; Figure 11.10 trace (d) to give an accurate estimate of fibre reference performance below 1.5 mHz. Above this frequency, the stability is limited by the high frequency noise of the OFC, and therefore, we determine the optimal cross-over frequency to occur at 1.5 mHz between the two references.

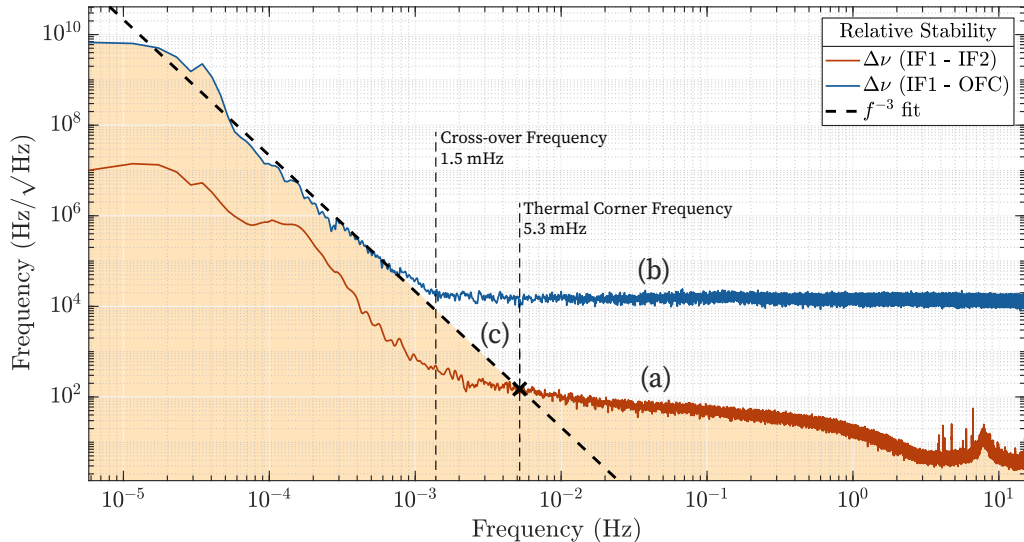


Figure 11.11: The estimated infrasonic noise floor of our 4 km fiber frequency reference. First we show trace (a), the subtraction of the two fiber frequency references and trace (b), the difference between optical frequency comb and fiber frequency reference from Figure 11.10. Trace (c) is the fitted f^{-3} curve with the yellow shaded area representing the inferred stability of the fiber references. We also highlight the cross-over frequency between the OFC and interferometer of 1.5 mHz, and the inferred thermal corner frequency of the fibre interferometers of 5.3 mHz.

To infer the onset of thermal drift in the fibre reference, we can use the IF1 and the OFC difference measurement to project the thermal drift corner frequency. To do this, we fit a f^{-3} curve to data below ~ 1 mHz and extrapolate this curve to higher frequencies, as shown in Figure. 11.11 trace (c). A f^{-3} curve is selected as it fits the low frequency data well and is justified by the f^{-2} frequency response of the isolation chamber while f^{-1} approximates the laboratory air-conditioner dynamics external to the isolation chamber.

From this, we find the intersect between the interferometer stability and extrapolated f^{-3} curve, which from Figure. 11.11 we see occurs at 5.3 mHz. Above this frequency we assume that thermal dynamics are not significant within the isolation chamber. Using the

f^{-3} , we can therefore infer the stability limits of IF1 and IF2 as highlighted by the shaded area in Figure 11.11.

11.6 Thermal Expansion of the Fibre Frequency Reference

As we now have an independent measure of the frequency drift using the OFC, we can calibrate from frequency back to displacement. By reversing the frequency calibration, we switch back to a phase measurement and compute the path length required to produce the measured phase shift. Accounting for the reciprocal of the frequency calibration, the absolute path length change of the fibre can be inferred through the following expression:

$$\delta OL = \frac{n\lambda\Delta L}{c} \Delta\nu(t)$$

Where δOL is the change in the optical path length of the fibre interferometer, ΔL is the length difference between the two arms of the interferometer, λ the interrogating optical wavelength and $\Delta\nu(t)$ the difference between the two frequency measurements. We can then take the frequency difference as shown in Figure 11.8 and calibrate it to thermally induced path length expansion over the 48 hours, shown in Figure 11.12.

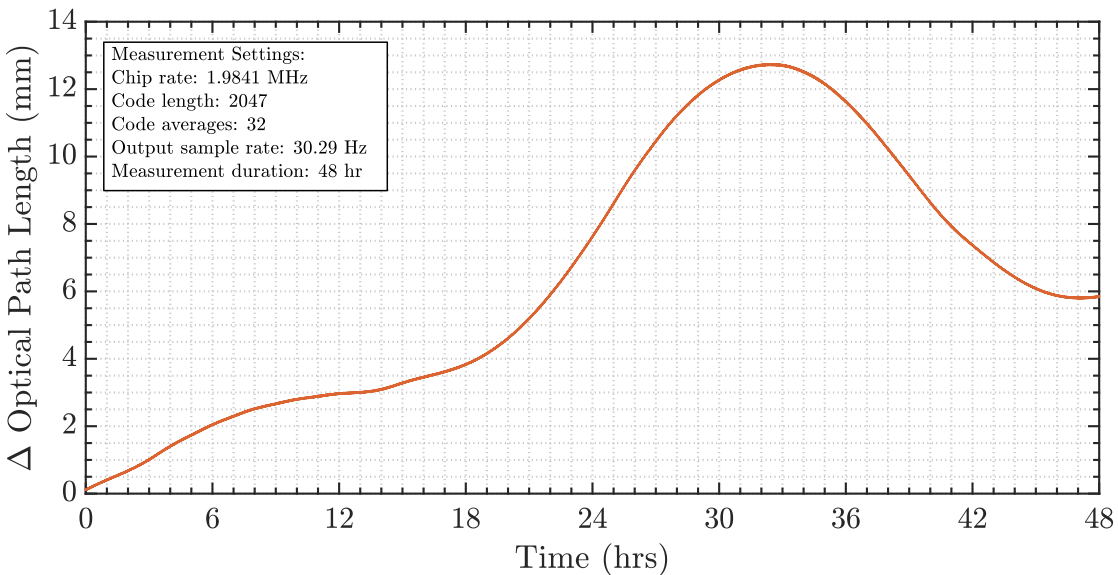


Figure 11.12: Calibrating the frequency difference between the two references as shown in Figure 11.8. Over the 4 km fibre spool length, a maximum expansion of 13 mm in optical path length (δOL) is measured. This expansion includes both the physical expansion of silica and any thermo-optic effects which alter the refractive index of the fibre.

We can compare this with the thermal expansion of silica and the thermo-optic coefficient of optical fibre, inferring the approximate temperature variation within the isolation chamber. Considering thermo-optic effects first, we can write the refractive index as a function of temperature up to first order as follows[124]:

$$n(\Delta T) = n_0(1 + \alpha_T \Delta T) + \mathcal{O}(\Delta T^2) \quad (11.1)$$

Where α_T is the first order thermo-optic coefficient for single mode fibre and equals $5.3 \times 10^{-6} /^\circ\text{C}$ at laboratory temperature[124]. The initial effective refractive index of the fibre is given by n_0 . The change in refractive index with temperature can then be expressed by removing the DC term as follows:

$$\delta n(\Delta T) = n_0 \alpha_T \Delta T \quad (11.2)$$

Repeating a similar process for length, we can determine the thermal expansion using the following expression:

$$\delta L(\Delta T) = \beta_T \Delta L \Delta T \quad (11.3)$$

In the above expression, β_T is the thermal expansion coefficient of silica, which gives the fractional length change per degree change in temperature; quoted to be $5.5 \times 10^{-7} /^\circ\text{C}$ [125]. We can convert this to an absolute length by factoring in the length of the spool, which is equivalent to the interferometer arm length difference, ΔL . Using Equations 11.1, 11.2 and 11.3, we can write the optical path length change as a function of these two effects:

$$\begin{aligned} \delta OL &= 2n(\Delta T)\delta L(\Delta T) + 2\delta n(\Delta T)\Delta L \\ \delta OL &= \underbrace{2n_0\beta_T \Delta L \Delta T}_{\text{Physical Expansion}} + \underbrace{2n_0\alpha_T\beta_T \Delta L (\Delta T)^2}_{\text{Second Order Correction}} + \underbrace{2n_0\alpha_T \Delta L \Delta T}_{\text{Thermo-Optic Shift}} \end{aligned} \quad (11.4)$$

Given the two coefficients, and the measured optical path length change of δOL over the 48 hours, we infer the equivalent temperature change of 0.18 ± 0.02 $^\circ\text{C}$, with the uncertainty dominated by the comb linewidth. Now that the temperature variation has been determined, we can use it to calculate the physical expansion, using Equation 11.3. Doing this, we find a maximum physical length change of 386 ± 1 μm over the 4 km spools. The remaining change in optical path length is therefore solely due to the thermo-optic shift in the fibre refractive index.

The calibration of the fibre frequency reference using the optical frequency comb presents a first step towards independently characterising fibre reference and presents an initial estimate of thermal effects on the fibre coil. Through this work, we can then inform the thermal stability requirements of future reference architectures.

Future Frequency References

Through the work discussed in this part of the thesis we have characterised an in-line fibre frequency reference architecture built on a digitally enhanced homodyne interferometric readout. The work extends on previous iterations of the fibre frequency reference by Ngo and McRae, with a focus on characterising the effects of Rayleigh scattering and temperature effects on the optical fibre.

The first area of investigation considered the coupling of Rayleigh backscattered light into the interferometer phase readout. With the use of the digital interferometric readout, we were able to suppress the coherent interference effects due to this scattering field. The relationship between the DI modulation frequency and the amount of coherent backscatter phase noise was established and verified through experimental work.

Following the Rayleigh scattering investigation, the fibre frequency reference was combined with an optical frequency comb to form a hybrid readout. The optical frequency comb was referenced to a Rubidium frequency standard, and therefore, provided an independent measure of the laser frequency. With this, we measured the optical path length change of the fibre reference and frequency comb and inferred the thermal corner frequency for the system.

Drawing from these conclusions, we finish this body of work by proposing a new frequency reference architecture for future investigation and implementation as a pre-stabilisation stage for a Strontium lattice clock.

12.1 Rayleigh Scattering Suppression Conclusions

In Chapter 10, we estimated the coupling and dynamics of Rayleigh backscattering on the relative stability between two fibre frequency reference interferometers. We further proceeded to investigate and evaluate how the deterministic change of the coherence of the optical source by altering the DEHoI chip frequency could suppress the coupling of Rayleigh backscatter induced phase noise.

We first determined the spectral shape of the noise feature to be a shelf in the frequency domain to be caused by non-linear up-conversion of phase noise due to Rayleigh scattering. As Rayleigh scattering is driven by the phase dynamics of the source, the shelf manifests itself at low frequencies, where the $1/f$ increase in frequency noise towards these frequencies exceeds the threshold for non-linear up-conversion. Physically, this corresponds to

the Fourier frequency at which the phase noise from the optical source drives the phase of the RBS field over a 2π shift. Using this insight, we develop a model to determine the shelf magnitude, assuming that the shelf is spectral white over the frequency band it occupies. This model is developed as a function of the optical coherence length of the source.

Experimentally we verify this by tuning the coherence length by altering the chip frequency of the digital interferometric readout. We see broad agreement between the experimental data and the theoretical model, with the main deviations from the trend occurring at a modulation frequency of 13.8 MHz and for low modulation frequencies. We hypothesize the former deviation is due to residual code noise arising from an unfavorable combination of DEHoI measurement bandwidth and modulation frequency, an insight drawn from subsequent work by Ya Zhang. The latter deviation we attribute to a reduced RBS coupling from the reference arm of the interferometer due to the limited lead fibre length. At the maximum, hardware limited, chip frequency of 41 MHz, we demonstrate suppression of the RBS noise shelf to $10 \text{ Hz}/\sqrt{\text{Hz}}$.

Based on the model, we extrapolate the necessary requirement for a $1 \text{ Hz}/\sqrt{\text{Hz}}$ noise shelf to be a 3.7 GHz chip frequency. This exceeds the current hardware, and will require a large investment both in hardware and software development time. We therefore recommend a transmissive interferometer such as a Mach Zehnder to avoid the effects of first order Rayleigh scattering.

12.2 Hybrid Fibre-Comb Conclusions

The hybrid fibre-comb reference aimed to characterise the infrasonic performance of the fibre frequency reference and had two main goals. Firstly, to provide an independent measure of the optical test source frequency. This was imperative for ensuring the calibration process used by the fibre frequency reference was accurate. Secondly, the long term stability of the comb was used to characterise the thermal performance of the system. Prior to this, both of these milestones had not been addressed within the existing body of fibre frequency reference work.

By measuring the optical test source using both the frequency comb and the fibre frequency reference over a 48 hour measurement, we firstly determine the frequency detuning between the two measurements due to thermal drift in the fibre reference. We see a peak drift over the two days of $\sim 200 \text{ MHz}$ with all the common short (hour) time-scale features due to the laser frequency being cancelled out by performing a differential measurement. This showed good agreement, at least on these timescales, between the fibre reference and the frequency comb.

The frequency detuning, was we converted to an equivalent optical path length change in the interferometer. Using the physical expansion and thermo-optic shift effects on silica, we infer the temperature change within the isolation chamber to be $0.18 \pm 0.02 \text{ }^\circ\text{C}$.

Finally, we use relative stability between the optical frequency comb and the fibre frequency reference to infer the thermal corner frequency of the fibre interferometer of 5.3 mHz. This gives an idea of the time-scales achievable with the frequency reference in its current form using only passive thermal isolation.

12.3 Towards A Future Reference Architecture

From the work presented in the previous few chapters we can draw several inferences which can inform the design of future frequency references. When combined with previous insight from work completed by Ngo, McRae and Gray we arrive at a nominal set of design parameters to inform the next generation of fibre frequency references.

The primary goal of the next generation architecture is to act as a pre-stabilisation stage for a strontium lattice clock. This requires a frequency stability of $1 \text{ Hz}/\sqrt{\text{Hz}}$ across the mHz band, which informs the parameter estimates in Table 12.1. In order to achieve this, Rayleigh scattering in this band must be addressed. Projecting the Rayleigh scattering work forward, we require a 3.7 GHz chip frequency to suppress Rayleigh scattering to this level. Due to the high bandwidth, and challenges with GHz level modulation generation, we opt for a transmissive interferometer, such as a Mach Zehnder topology.

The next challenge is the mitigation of thermally induced drift. As the current system is passively stabilised, transitioning to an active temperature stabilised enclosure will see a tangible improvement. If we want to reduce the thermal frequency drift by two orders of magnitude, from 200 MHz to 2 MHz, we can compute the necessary thermal stability using the methods outlined in Chapter 11. We then arrive at a required thermal stability of 1.8 mK, which can be readily achieved through active thermal isolation[89].

The next step of the process is to determine the digital signal processing requirements. There are several parameters that factor into this, namely the arm length difference of the interferometer, phase resolution of the digital interferometric readout, the chip frequency and the code length. If we aim for a modest phase resolution of $100 \mu\text{rad}/\sqrt{\text{Hz}}$ at 1 Hz, we can then fix the required arm length difference in order to achieve the noise floor requirement. Once the arm length is fixed, we can define a Nyquist frequency and from there a chip frequency and code length. A list of the design parameters is shown in Table 12.1.

Performance Metric	Requirement
Frequency Noise Floor	$1 \text{ Hz}/\sqrt{\text{Hz}}$ to 10 mHz
Thermal Frequency Drift	2 MHz
Required Thermal Stability	1.8 mK
Phase Noise Floor	$100 \mu\text{rad}/\sqrt{\text{Hz}}$ at 1 Hz
Arm Length Difference ΔL	3270 m
Nyquist Bandwidth	12.2 kHz
DI Chip Frequency	25 MHz
DI Code Length	1023 (10 bit)

Table 12.1: Parameter estimates for a future fibre frequency reference architecture

One factor yet to be considered is the differences in both optical and electronic delays between the two interferometers. At the time of writing, it has been demonstrated that the timing offsets that arise from the relative delay between the two interferometers results in only partial cancellation of laser frequency noise in the differential stability

measurement. This is currently the limiting noise source at high Fourier frequencies.

In order to address this, on-FPGA delay matching down to the clock frequency of 125 MHz can readily achieve timing resolution of 4 nanoseconds, corresponding to an optical path length of 80 cm in fibre. Beyond this, it is possible to use fractional delay filters in post-processing to ensure complete frequency noise cancellation and uncover the interferometer high frequency stability [126].

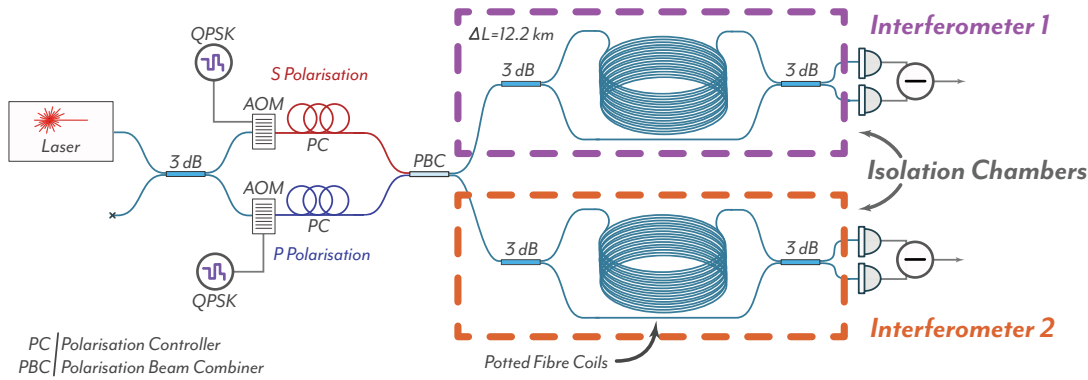


Figure 12.1: A nominal design for a future fibre frequency reference architecture. The most significant change is the switch to a Mach Zehnder topology, which provides immunity to first order Rayleigh scattering. The fibre coil itself will be on the order of 12.2 km to achieve the $1 \text{ Hz}/\sqrt{\text{Hz}}$ frequency stability. Further, by making a potted coil and coupler substructure, the mechanical stability and thermal homogeneity of the interferometer can be improved. Finally, we integrate a polarisation tracking algorithm by encoding orthogonal polarisations with unique QPSK codes. This allows for the tracking of polarisation evolution within the interferometer and enables the correction of polarisation induced phase noise.

In addition to the work presented in this thesis, we can also integrate some of the subsystems developed in previous iterations of the frequency reference. A key system to include is the polarisation management scheme developed by Gray [12]. By preparing the optical polarisation state with two orthogonal polarisations encoded each with orthogonal codes, we are able to recover the polarisation Jones matrix for the interferometer. Using this method, it is then possible to algebraically cancel polarisation noise, removing polarisation noise which occurs in the 1 - 10 mHz band.

The last major optical change is to the construction of the fibre optic delay line used for the long arm of the interferometer. From applications such as fibre optic gyroscopes, potted coils provide a physically compact, monolithic structure which can reduce the impact of thermal and mechanical coupling. They consist of a tightly wound coil, self supported by an adhesive resin which creates a single toroidal structure. By embedding the remaining fibre components within the centre of the potted coil, a discus structure can be created which act as a monolithic structure for mechanical and thermal effects.

Combining these recommendations, we arrive at a nominal design, shown in Figure 12.1. Initial work on this architecture is underway lead by Ya Zhang.